LASER PROCESSING OF METALS AND POLYMERS

by

Senthilraja Singaravelu
B.Sc., May 1998, University of Madras, India
M.Sc., May 2001, Bharathiar University, India
M.S., May 2006, Old Dominion University, USA

A Thesis Submitted to the Faculty of
Old Dominion University in Partial Fulfillment of the
Requirements for the Degree of

DOCTOR OF PHILOSOPHY

PHYSICS

OLD DOMINION UNIVERSITY
May 2012

Approved by:

_____
Geoffrey A. Krafft (Director)

_____
Michael J. Kelley

_____
Gail E. Dodge

_____
Charles I. Sukenik

_____
Patrick G. Hatcher

ABSTRACT

LASER PROCESSING OF METALS AND POLYMERS

Senthilraja Singaravelu
Old Dominion University, 2012
Co-Directors: Dr. Michael J. Kelley
Dr. Geoffrey A. Krafft

A laser offers a unique set of opportunities for precise delivery of high quality coherent energy. This energy can be tailored to alter the properties of material allowing a very flexible adjustment of the interaction that can lead to melting, vaporization, or just surface modification. Nowadays laser systems can be found in nearly all branches of research and industry for numerous applications. Sufficient evidence exists in the literature to suggest that further advancements in the field of laser material processing will rely significantly on the development of new process schemes. As a result they can be applied in various applications starting from fundamental research on systems, materials and processes performed on a scientific and technical basis for the industrial needs. The interaction of intense laser radiation with solid surfaces has extensively been studied for many years, in part, for development of possible applications. In this thesis, I present several applications of laser processing of metals and polymers including polishing niobium surface, producing a superconducting phase niobium nitride and depositing thin films of niobium nitride and organic material (cyclic olefin copolymer).

The treated materials were examined by scanning electron microscopy (SEM), electron probe microanalysis (EPMA), atomic force microscopy (AFM), high resolution

optical microscopy, surface profilometry, Fourier transform infrared spectroscopy (FTIR) and x-ray diffraction (XRD). Power spectral density (PSD) spectra computed from AFM data gives further insight into the effect of laser melting on the topography of the treated niobium.

This thesis is dedicated to my parents, sister and all my teachers.

ACKNOWLEDGMENTS

My Ph. D. degree would not have been possible, without the guidance and the help of several individuals, who in one way or another, contributed and extended their valuable assistance and support, in the preparation and completion of this study. It is my pleasure to thank those who helped me accomplish my desire.

I am whole heartedly grateful to my Ph.D advisors Dr. Michael J. Kelley and Dr. Geoffrey Krafft. Thanks to Dr. Michael J. Kelley for planning my research, training me and guiding me in each step of research. Thanks for the enthusiasm, inspiration, and great efforts to explain things clearly and constant encouragement to complete my assignment. Their guidance and support from the initial to final stage enabled me to develop an understanding of the subject. Thanks to Dr. Geoffrey Krafft for accepting me as his student and guiding me throughout the journey of Ph.D. Thank you for all the support you both have provided me, if not I would have been lost.

I would like to thank my committee members (Dr. Gail Dodge, Dr. Charles Sukenik and Dr. Patrick Hatcher) for their patience, guidance and contributions to my thesis. A special thanks to our department chair Dr. Charles Sukenik and Dr. Gail Dodge who were always ready to help me professionally and personally. I would like to thank Dr. Lepsha Vuskovic for her understanding and support. I also thank the funding support I have received without it this research would not have been possible.

It was a privilege to be trained by a group of scientists, who are the core of FEL family. Working with different teams like FEL, SRF, and CASA has given confidence and inspiration for my future life. Thank you all.

I owe my deepest gratitude to Dr. J. Michael Klopf from FEL team, who was beside me supporting my experiments. Any discussion I had with him has always been informative and helpful. Thanks for his encouragement and patience. He faced the challenge of a demanding student as I was. Eventually my progress will inspire many more research students to seek his fortunate advice and guidance.

I wish to thank Dr. Shukui Zhang from FEL team for training and teaching me the laser system. I can never forget the timely help rendered by Dr. Gwyn Williams, Dr. Steve Benson, Dr. Jim Coleman, Cody Dickover, Chris Gould, Joe Gubeli, Kevin Jordan, Jim Kortze, Dan Sexton, Dr. Michelle Shinn, Dr. Richard Walker, Tom Powers and Guy Wilson, during my stay in FEL building by providing all the help I requested for.

I was greatly benefited working with Dr. Whelan Colm, Dr. Mark Havey and

TABLE OF CONTENTS

LIST OF TABLES

LIST OF FIGURES

CHAPTER 1

INTRODUCTION

I. BACKGROUND AND MOTIVATION

Invented in 1960, the laser offers a unique set of opportunities for precise delivery of high-quality coherent energy. Due to stimulated emission in a resonator, the generated photons are multiplied. As the stimulated photons share the same wavelength, direction, and phase, the resulting electromagnetic wave is characterized by a high degree of coherence, a very narrow spectral distribution, and low divergence. This unique behavior results in very good focusing capabilities, and the resulting power densities in the focus of a high-power laser can reach 10^{16} W/cm^2 easily.[1] Such high intensities enable (for example) rapid thermal processing, where thermal energy is confined to the beam spot without collateral damage to the adjacent material.

Sufficient evidence exists in the literature to suggest that further advancements in the field of laser material processing will rely significantly on the development of new process schemes. The process control system must enable the precise delivery of photons to a specific material with high spatial and temporal resolution; i.e., the laser control system parameters must be appropriately varied for the particular material under irradiation at the optimum time.[2] Prior experiments have demonstrated that a diverse set of material transformations can be realized by a judicious choice of the common laser process parameters, such as the wavelength, pulse amplitude, temporal and spatial characteristics, polarization, and total photon dose.[3-14]

Considering the interaction of laser radiation with materials, there are a few key parameters that come into play when predicting what effects take place. They are the amount of average laser power delivered to the material interaction site when the laser is operating in a continuous wave (CW) mode and the amount of laser energy in joules delivered to the material interaction site when the laser is operating in a pulsed mode. This energy and its spatial and temporal distribution determine what kind of material modification will occur.[15] To understand the effect of the laser beam on the irradiated material, the electronic and lattice dynamics must be taken into account. In order to induce any effect on the substrate, the laser light must be absorbed and the absorption process can be thought of as an energy source inside the material.

The initial interaction during laser processing is the excitation of electrons (especially in conductors), vibrations (in insulators), or both (in semiconductors) from their equilibrium states to some excited state.[16] These typical single photon processes are well-known in a wide field of physics and have been discussed extensively.[17, 18] The excitation energy is rapidly converted into heat. This is followed by various heat transfer processes: conduction into the materials, and convection and radiation from the surface. The most significant heat transfer process is heat conduction into the material. The generation of heat at the surface and its conduction in the material establishes the temperature distribution in the material, and depends on its thermo-physical properties and the laser parameters.

As mentioned above, in laser material processing the wavelength of the lasers and the absorption spectrum of different materials is to be considered. For example, the wavelength of CO_2 lasers is 10.6 μm, which is highly reflective with copper. For that

reason, CO_2 lasers are not typically used when doing material processing with copper. Shorter wavelength lasers perform much better with copper. The wavelengths of other lasers that are typically used for material processing are the Nd:YAG laser at 1.064 μm, the Yb-fiber laser at 1.07 μm, the frequency doubled Nd:YAG at 0.532 μm, the excimer laser that can provide at least four UV wavelengths including 0.244 μm, and recently the tunable free electron lasers (FEL). When compared with conventional lasers, the significant difference in the FEL lies with the laser medium, an energetic (free means unbound) electron beam. Current FELs cover wavelengths from millimeter to the soft x-ray range. The advantages of the FEL over conventional lasers include wavelength tunability and high powers that can be achieved in areas of the infrared spectrum, which have not been achieved using conventional lasers. The FEL's unique tunability enables the FEL to ablate organics with minimal chemical disruption.[19,20]

Nowadays laser systems can be found in nearly all branches of industry for numerous applications. This is a result among other things of close interactions between the industrial needs and fundamental research on systems, materials and processes performed on a scientific and technical basis. Today, basic knowledge of the interactions between laser radiation and materials exists, but not all phenomena are fully understood and some of the process limits are not yet reached. Laser processing covers a wide range of power, interaction time and process materials with length scales from nanometers to meters. Therefore, developing a science base is challenging.[21] Although often research is application driven, basic understanding of the process often requires in depth knowledge obtained through mathematical modeling of the process and online process diagnostics. The understanding of the process limiting phenomena is a must in order to extend the

technical boundaries towards the physical limitations, so that laser materials processing will become more and more economic.[22] In summary, understanding the availability of research equipment, laser resources and deposition technique to be used are the primary steps to perform laser processing on both metals and polymers.

A.   Rapid thermal processing

Materials processing is one of the important and active areas of research in heat transfer today.[23] Rapid thermal processing (RTP) of materials refers to manufacturing and material fabrication techniques that are strongly dependent on the thermal transport mechanisms, involving rapid heating and cooling processes.[24] The laser pulse allows one to restrict the energy deposition within the absorbing volume and minimize collateral thermal damage.[25] In RTP, the laser pulse duration (τ_p), is typically shorter than the time of dissipation of the absorbed laser energy by the thermal conduction (τ_{th}), a condition that is commonly referred to as thermal confinement.[26, 27] The condition for thermal confinement can be expressed as $\tau_p < \tau_{th} \sim L_p^2/D_T$, where D_T is the thermal diffusivity of irradiated material and L_p is the laser penetration depth or the size of the absorbing structure. The pulse duration in this regime is usually shorter than the time needed for gas phase bubble formation and diffusion in the process of heterogeneous boiling.[28, 29] As a result, the absorbing material can be overheated much beyond the boiling temperature, turning a normal surface evaporation at low laser fluences into an explosive vaporization, or phase explosion, at higher fluences.[25-31]

B.   Ablative materials synthesis

The interaction of intense laser radiation with solid surfaces has been studied extensively for many years as a result of possible applications, such as precision

machining, materials synthesis, thin film deposition, and laser induced breakdown spectroscopy for elemental analysis of materials. An onset of massive material removal or ablation is defined by the critical energy density sufficient for the overheating of the surface layer up to the limit of its thermodynamic stability.[25]

The term ablation is generally used for material removal processes by photo-thermal or photo-chemical interactions. In the photo-thermal process, the absorbed laser energy is converted into thermal energy in the material. The subsequent temperature rise at the surface may facilitate the material removal due to generation of thermal stresses. This possibility is more pronounced in the inhomogeneous targets such as coated materials where the thermal stresses cause the explosive ablation of thin films. When the incident laser energy is sufficiently large, the temperature at the surface exceeds the boiling point causing rapid vaporization. These processes of material removal by thermal stresses and surface vaporization are generally referred to as thermal ablation.[32]

In conventional photo-ablation, the energy of the incident laser radiation causes the direct bond breaking of the molecular chains in organic materials resulting in material removal by molecular fragmentation. This suggests that for the ablation process, the photon energy must be greater than the bond energy and that selection of wavelength is more important for different organic materials, making the FEL a unique laser source for photo-ablation of organic materials.

II. EXPERIMENTAL FACILITY

(REQUIRED CAPABILITIES)

To perform RTP, a chamber that can sustain both vacuum ($\sim 10^{-7}$ Torr) and positive pressure (~ 600 Torr) is needed. Experiments conducted during positive pressure can be

used to nitride metals using RTP in a nitrogen atmosphere and the experiment conducted in vacuum can be used to smooth (polish) the surface of the metals. A robust turbo pump attached to the vacuum chamber would be useful to keep the vacuum stable throughout the experiment. RTP does not require the use of external cooling agents. The high thermal conductivity of metals causes rapid self-quenching which means that the laser radiation heats up near surface layers only and the unmelted bulk material acts as the heat sink.[33] Motorized optics mounts and rotating target/substrate holders are needed, which can control the laser beam path to raster on the metal surface according to some specific pattern and velocity of beam rastering during the experiment. This laser rastering procedure and target/substrate rotation velocity can also control the accumulated pulse overlap per area on the surface of the samples.

Among different methods to deposit the thin films, pulsed laser deposition (PLD)[34,35] is a physical vapor deposition (PVD) process that fulfills the needs. In PLD the materials placed in a target are ablated by intense pulsed laser radiation in a vacuum or reactive or inert processing gas atmosphere. There is an emerging body of results that indicate that PLD may revolutionize the synthesis of complex inorganic and organic thin film materials. A unique feature of PLD is that the source material is evaporated (ablated) in a non equilibrium process such that material is evaporated at the stoichiometry of the bulk. Hence, it is possible to prepare thin films of incongruently melting solids that have a stoichiometry characteristic of the solid phase prior to melting. The ablation rates are primarily determined by the laser fluence, the pulse duration, the number of pulses, and the pulse repetition rates.

A PVD Products Inc. PLD 5000 system can sustain the pressure and vacuum needed. This system is also capable of rastering the laser beam on the target to control accumulated pulse overlap. Rastering the laser beam and individual rotation of target pedestals provides an added advantage for laser processing.

For the present studies, a Spectra Physics, "High Intensity Peak Power Oscillator" (HIPPO) nanosecond laser with 1064 nm wavelength is used. This laser can be used as the source for RTP to nitride metals (here niobium), and also to ablate niobium from the surface to produce a thin film. In contrast, tunable IR free electron lasers (FEL's) have faithfully deposited a wide range of organics. Such systems are too costly and too complex to be widely deployed in the laboratories of individual investigators (Appendix A provides details of the facility and more about PLD 5000 and laser systems used). So the IR-FEL at Thomas Jefferson National Accelerator Facility was used to establish an advanced PLD user facility based on the IR FEL in one of the labs of the FEL building, at Jefferson Lab, in collaboration with the Laser Materials Interaction group at Vanderbilt University and the Naval Research Laboratory. Appendix B provides shows several pictures of the installation and commissioning of these systems in user lab of FEL building.

Having the basics of laser-material interaction, the availability of the PLD 5000 system, the HIPPO ns laser, the FEL beam from Jefferson lab and space in FEL building and other facilities like nitrogen gas, chiller water, etc, the installation and commissioning of the equipment is documented as well as the experiments that were finally performed. In this thesis, I present several applications of laser processing of metals and polymers including polishing niobium surface (Chapter 2), producing a

superconducting phase niobium nitride (Chapter 3) and depositing thin films of niobium

nitride (Chapter 4) and cyclic olefin copolymer (Chapter 5).

CHAPTER 2

LASER POLISHING OF NIOBIUM FOR

APPLICATION TO SRF

ACCELERATOR CAVITIES

I. INTRODUCTION

Whenever the electromagnetic radiation hits the surface of any material or metal various phenomena like reflection, refraction, absorption, scattering and transmission occur. The total energy absorbed is an important parameter in laser material interactions. Absorption of radiation in the materials results in various effects such as heating, melting, vaporization, plasma formation, etc., which forms the basis of several laser materials processing techniques.[36] To understand these phenomena various laser parameters like intensity, wavelength, angle of incidence, and polarization; and various material properties including absorption, thermal conductivity, specific heat, density, and latent heat are needed.

Electromagnetic radiation can interact only with the electrons of the material because the much heavier nuclei are not able to follow the high frequencies of laser radiation.[37] When the electromagnetic radiation passes over the electrons it exerts a force and sets the electrons into motion by the electric field of the radiation. The force exerted by the electromagnetic radiation on the electron can be expressed as

$$\vec{F} = e\vec{E} + e\vec{v} \times \vec{H}, \qquad (1)$$

where e is the electron charge, $\vec{v}$ is the velocity of electron, $\vec{E}$ is the electric field, and $\vec{H}$ is the magnetic induction. If it is considered that the electric and magnetic fields carry the same amount of energy in laser photons, then according to Eq. (1), the contribution of magnetic field to the force is smaller than that of the electric field by a factor of the order $\vec{v}/c$. Hence, the most important term in the above equation is $e\vec{E}$. The absorbed radiation, thus results in the excess energy in the charged particles, such as kinetic energy of free electrons, excitation energy of the bound electrons, etc. The absorption of laser radiation in the material is generally expressed in terms of the Beer-Lambert law

$$I(z) = I_o e^{-\alpha z}, \qquad (2)$$

where $I(z)$ is the intensity at depth z, I_o is the incident intensity, and α is the absorption coefficient. Thus the intensity of the laser radiation gets attenuated inside the material. The length over which a significant attenuation of laser radiation takes place is often referred to as the penetration depth ($d = \lambda/4\pi\kappa$, where λ is the wavelength and κ is the extinction coefficient) and is given by the reciprocal of the absorption coefficient ($\alpha = 1/d$).

Another important parameter influencing the effects of laser-material interactions is the absorption of laser radiation by the material. It can be defined as the fraction of incident radiation that is absorbed at normal incidence. For opaque materials, the absorption (A) can be expressed as $A = 1 - R$, where R is the reflectivity of the material.

The reflectivity and the absorption of the material can be calculated from the measurements of the optical constants.

The reflectivity of the metals depends upon the angle of incidence, plane of polarization and wavelength of the laser beam. If the plane of polarization is perpendicular to the plane of incidence, then it is called an "s" ray; if it is parallel to the plane of incidence it is called a "p" ray. The reflectivity[38] at any given angle with different polarizations can be calculated by,

$$R_p = \left| \frac{E'_o}{E_o} \right|^2 ; \text{where} \left| \frac{E'_o}{E_o} \right| = \frac{n\cos\theta - \frac{\mu}{\mu'}\sqrt{n'^2 - n^2\sin^2\theta}}{n\cos\theta + \frac{\mu}{\mu'}\sqrt{n'^2 - n^2\sin^2\theta}} \tag{3}$$

$$R_s = \left| \frac{E'_o}{E_o} \right|^2 ; \text{where} \left| \frac{E'_o}{E_o} \right| = \frac{\frac{\mu}{\mu'}\cos\theta - n\sqrt{n'^2 - n^2\sin^2\theta}}{\frac{\mu}{\mu'}\cos\theta + n\sqrt{n'^2 - n^2\sin^2\theta}} \ , \tag{4}$$

where n are the indices of refraction and μ are the relative permeabilities of the interface materials. The reflectivity of the metal at normal angle of incidence[36,39] is calculated to verify the equation based on the angle of incidence. The metal selected here for my research is niobium. The values of the optical constant for niobium at 1064 nm are $n = 1.566$; $\kappa = 5.09$; $n' = n + i\kappa = 5.326$; $\mu/\mu' = 1.$[40] Fig. 1 gives the reflectivity of niobium ($\lambda= 1064$ nm) at different angles of incidence and polarization.
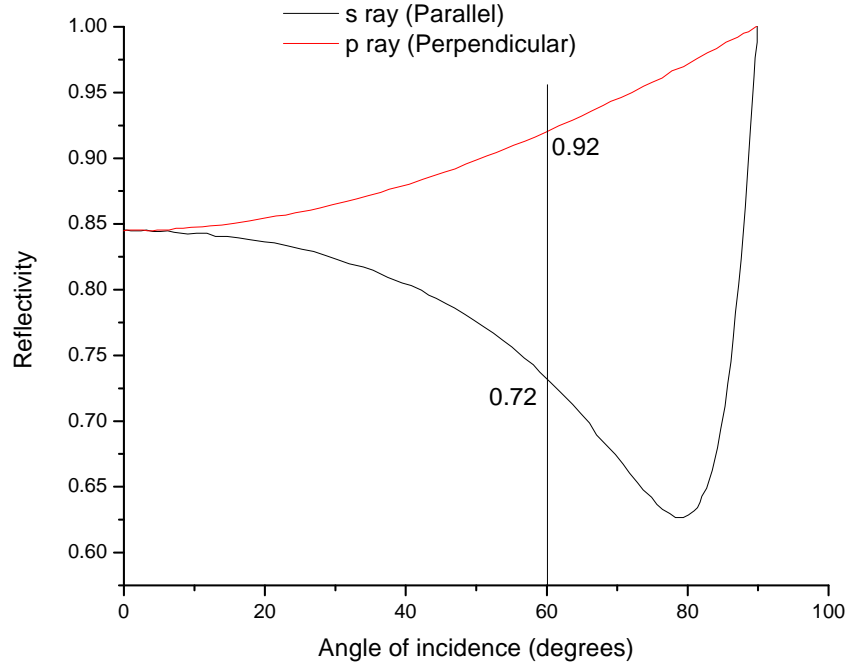
FIG. 1. Reflectivity of niobium at 1064 nm as a function of incidence angle.

The pulse duration of our laser (τ_p = 15 ns) is much longer than the electron collision frequency of the niobium ($\tau_e \cong$ 60 ps),[41] so that a thermal Fermi distribution can be assumed for the electrons. Thus, the absorption of laser light energy by the bulk material can be described by Fourier heat conduction equations.[42] This absorbed energy is distributed by heat conduction. Thus the heat conduction equation has to be solved. In the present work the dimension of the laser spot ($\cong$ 80 µm) is much larger than the thermal diffusion length ($\approx$ nm), and use of a 1D diffusion equation is justified. The heat flow in niobium can be represented by the following equation[42,43, 44]

$$\frac{\partial T(z,t)}{\partial t} - \frac{\partial}{\partial z}\left(k(T)\frac{\partial T(z,t)}{\partial z}\right) = \frac{A(z,t)}{\rho(T)c_p(T)} \tag{5}$$

where $T(z,t)$ is the temperature at depth z at time t, ρ is the mass density, $k = \frac{\lambda}{\rho c_p}$ is the

thermal diffusivity, and $A(z,t)$ is the heat generation (source or which is the combination

of absorbed laser energy and internal heat sink) which can be written as

$$A(z,t) = \alpha I(t)(1-R)e^{-\alpha z} + \Delta U(z,t), \qquad (6)$$

where $\Delta U(z,t)$ is the internal heat sink (phase transformation) and $I(t) = I_o \exp^{-(t-t_o)^2/2\sigma^2}$,

which describes the Gaussian temporal laser pulse profile. The parameters used for our

experiment are σ = 6.37 ns (for 15 ns FWHM), $I_o = \frac{H}{\sigma\sqrt{2\pi}}$ and H is the fluence

(J/cm^2). The reflectivity for niobium for the wavelength 1064 nm at an angle of 60^0 is

0.21 for parallel polarization and 0.68 for perpendicular polarization.

II. MELTING DEPTH PROFILE

At a sufficient fluence produced by the laser beam, the surface of the metal may reach

the melting point and the boiling point. The corresponding laser fluences are known as

the melting and boiling thresholds respectively. Considering a single pulse, when it is

incident upon on the surface of the metal, the surface temperature may exceed the

melting and boiling point, while producing an evolution of depth of melting during laser

irradiation. Fig. 2 shows what happens on the surface during one pulse. Upon the laser

pulse, the temperature of the surface increases and reaches the maximum at pulse time t_p

and then decreases. There are five stages during this process.[37] They are,

1. Temperature reaches T_1 ($T_1 < T_m$) at time t_1 ($t_1 < t_p$),

2. Temperature reaches melting point (T_m) at time t_2 ($t_2 < t_p$),

3. Temperature reaches maximum, T_{max} ($T_{max} > T_m$) at time t_p,

4. Temperature decreases to melting point T_m at time t_3 ($t_3 > t_p$), and

5. Temperature reaches T_1 ($T_1 < T_m$) at time t_1 ($t_1 > t_p$).
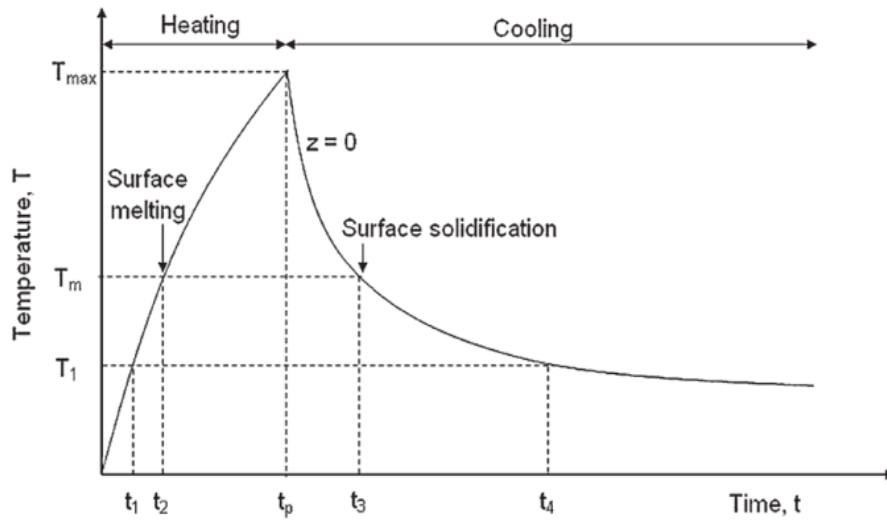
FIG. 2. Surface temperature as a function of time following

a laser pulse incident upon a surface.
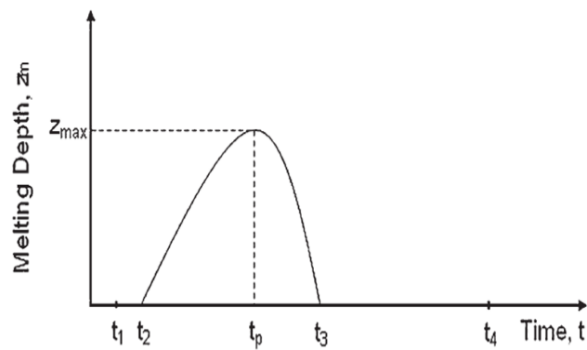
FIG. 3. Melting depth profile of a metal as a function of time.

Fig. 3 shows the melting depth of a metal as a function of time. During irradiation, the melting starts at time t_2 only. Before that time, the material is just heated without any changes. After t_2, the depth of the melting increases, until it reaches the maximum solid-liquid interface depth (z_{max}), which starts to decrease after the surface heating phase, after the time t_p. After time t_p, the surface temperature starts to decrease rapidly, and the solidification process starts. After the surface solidification time t_3, the metal cools down further.

III. SIMULATION FOR SURFACE TEMPERATURE

As there is no analytical solution to Eq. (5), we use the finite differences method (forward difference approximation) to solve the equation. Time (t) and space (z) are divided equally as, $t^i = i\Delta t$ and $z_n = n\Delta z$ (where $n = 0....N$ and z is the direction normal pointing into the surface). Defining the function T whose value T^i is known at the discrete points, the approximation of first and second order partial differential operators at point i can be written as,

$$\frac{\partial T}{\partial t} = \frac{T^{i+1} - T^i}{\Delta t}, \text{ and } \frac{\partial^2 T}{\partial z^2} = \frac{T_{n-1} - 2T_n + T_{n+1}}{(\Delta z)^2}, \quad (7)$$

where T_n^i is the temperature at the time $t^i = i\Delta t$ in the layer $z_n = n\Delta z$. The calculation starts at $i = 0$ with $T_n^0 = 300\ K$ for all n. Evaluation of the first order derivative with respect to time and the second order with respect to direction (here z direction), substituting Eq. (7) into Eq. (5), we can write,

$$T_n^{i+1} = T_n^i + \Delta t. \left[\frac{k_n^i}{(\Delta z)^2} \cdot \left(T_{n-1}^i - 2T_n^i + T_{n+1}^i \right) + \frac{A_n^i}{\rho c_{p,n}^i} \right], \quad (8)$$

which is also called a forward time centered space scheme. To satisfy the Newmann stability criterion ($(\Delta z)^2 / \Delta t \geq 0.5\, k$), we chose $\Delta z = 7.5$ nm and $\Delta t = 0.5$ ps.

The thermo-physical properties of niobium[45, 46, 47] were extrapolated to 5100 K, just above its boiling temperature (5017 K).[48] From this, the thermal conductivity for niobium as a function of temperature is plotted in Fig. 4. The absorption coefficient vs. wavelength is shown in Fig. 5. The simulation for the surface temperature was done using C++ using Eq. (8). The temperature dependent thermal conductivity (Fig. 4), absorption coefficient (Fig. 5), and other thermal parameters shown in Table I was used for the simulation. Fig. 6 shows the computed results of the surface temperature of niobium vs. time, for a single pulse of various fluences. Fig. 7 shows the maximum surface temperature niobium can reach at different fluences. By properly adjusting the fluence one can control many applications using the phenomenon of laser material interactions, as shown in the body of this thesis.

TABLE I. Material parameters used in the simulation to calculate surface temperature rise of niobium.

Parameter	Value
Penetration Depth	16.633 nm
Melting point	2740 K
Boiling point	5017 K
Critical temperature	12500 K
Density	8.57 g/cm^3
Molar Mass	92.9063
Enthalpy of fusion	26.94 kJ/mol
Enthalpy of vaporization	696.6 kJ/mol
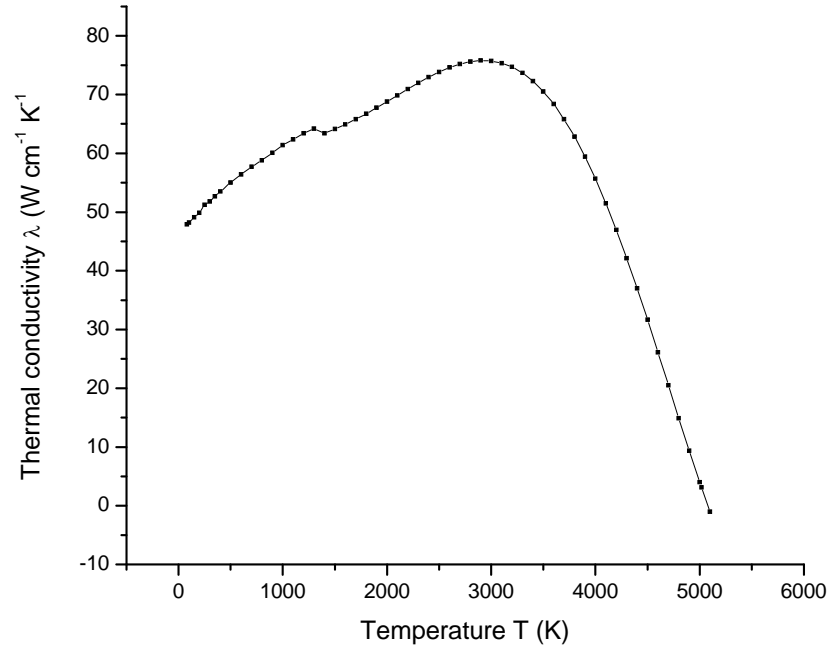
FIG. 4. Thermal conductivity of niobium as a function of temperature.
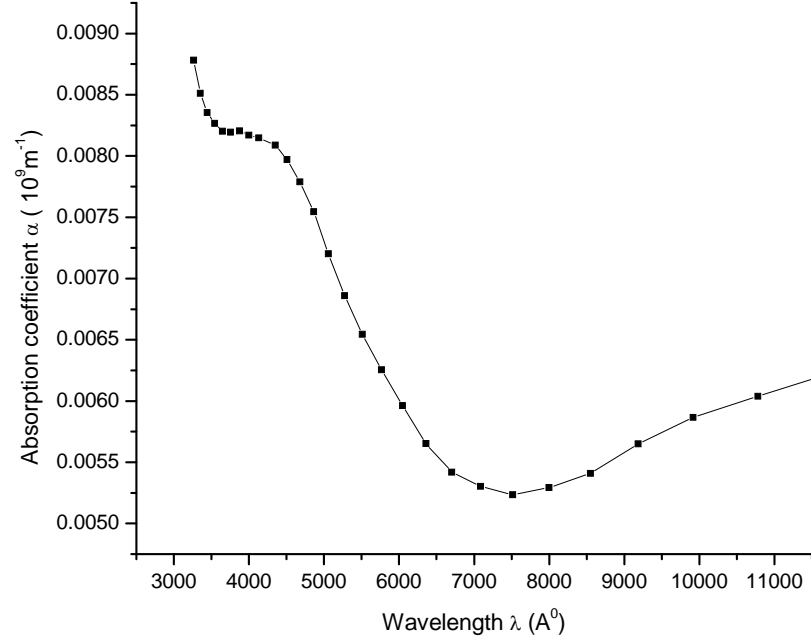
FIG. 5. Absorption coefficient of niobium as a function of wavelength.
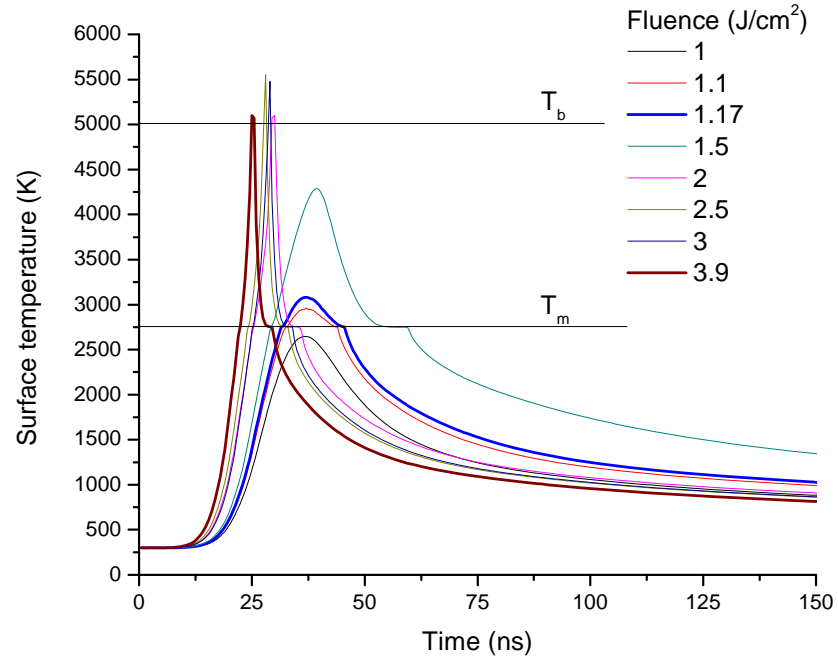
FIG. 6. Calculated time dependence of niobium surface temperature after irradiation by a single 15 ns pulse of the indicated fluence.
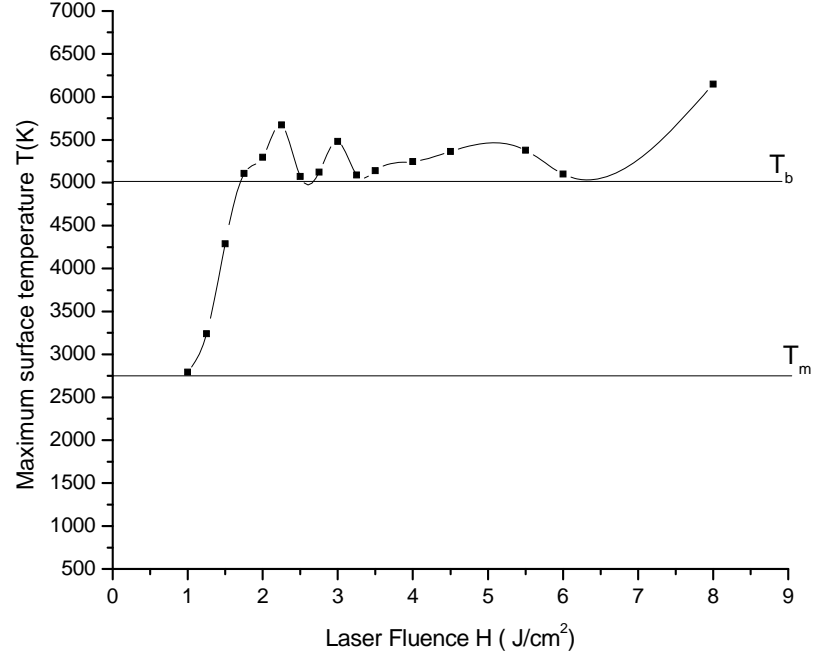
FIG. 7. Maximum surface temperature irradiated
by a single 15 ns pulse of various fluences.

IV. LASER POLISHING OF NIOBIUM FOR SRF ACCELERATOR CAVITIES

Accelerators based on superconducting niobium RF cavities will play a growing role in the future. Their science and technology has been recently reviewed.[49] A key feature is that, in the superconducting state, the RF field penetration is limited to the surface-adjacent 40 nm, lending great importance to the composition and topography of the cavity interior surface. Accordingly, the final steps of present day cavity fabrication methods seek to remove damaged or contaminated material by etching off approximately 100 μm. A disadvantage of this etching process is that it uses aggressive acids (hydrofluoric, nitric, sulfuric) creating cost, safety, and environmental impact issues.

The use of lasers to smooth metal surfaces began to be reported in the 1970's and several processing strategies have evolved since. A recent review presents the history, the fundamentals, and the process applications.[33] The broad theme in laser polishing is that the laser energy melts some of or the entire surface and leveling proceeds by melt flow under the influence of surface tension until solidification intervenes. The events may be viewed in terms of lower and higher energy density regimes, shallow surface melting (SSM) and surface over-melting (SOM), respectively.[50] In SSM, melting occurs at prominences and capillary forces cause the melt to diffuse into depressions. In SSM, a liquid layer covers the surface. While surface tension driven leveling proceeds, other mechanisms can give rise to oscillations manifest as regular ridge structures.

Laser surface melting (LSM) is also used to process surfaces to achieve superior bonding of deposited layers, reduced distortion, and improved physical properties, e.g., increased hardness, wear resistance, and corrosion resistance.[51] For example, laser polishing of micro-milled nickel and titanium alloy parts reduced roughness more than 85%.[52] Others[53-55] used pulsed laser micro-polishing (PLµP) to reduce the surface roughness of micro-fabricated and micro-milled parts. A significant range of pulse durations and spot sizes has been effective.[56,57] Pulse durations in the nanosecond range were found most effective for SMM.[58] The most recent reports include laser induced surface finishing of titanium for bio-implants[59,60] and micro-roughness reduction of tungsten films in the IC industry.[61] At the opposite end of the size scale, mobile laser polishing is being investigated for application to railroad rail.[62]

Characterizing the resulting surface topography is a challenging task, as it is unknown at what scale roughness is important to SRF performance; a recent review is available.[63]

The traditional parameter characterizing surface topography is the RMS roughness (R_q), the root mean square height of a surface around its mean value. However, this statistical description, though simple and reliable, makes no distinction between peaks and valleys and does not account for the lateral distribution of surface features. A more complete description is provided by the PSD (power spectral density), which performs a decomposition of the surface profile into its spatial wavelengths and allows comparison of roughness measurements over different spatial distance ranges.

The present work gives results obtained by laser melting to smooth the surface of niobium. The resulting topography was examined by scanning electron microscopy (SEM) and atomic force microscopy (AFM). PSD's were computed from AFM data.

V. EXPERIMENTAL DETAILS

A. Fluence range to be explored

Laser polishing requires that each pulse heats the surface to a temperature between melting and boiling for the longest possible time, so that surface tension can act. We employed computational modeling to predict the time course of the surface temperature as a function of the laser irradiation parameters. The goal is to identify the most promising range of experimental parameters. So the laser fluences between 0.6 to 2.3 J/cm^2, based on Figs. 6 and 7, were explored. To additionally gain insight into the effect of work piece preheat; calculations were carried out assuming the initial surface temperature to be 300K, 473 K, or 673 K.

Fig. 8 shows the calculated surface temperature of niobium vs. fluence, for a single pulse at the three initial surface temperatures. This predicts that for a single pulse, surface melting starts at about 1.1 J/cm^2 when the initial surface temperature is at 300 K. When

the initial surface temperature is 473 K or 673 K, the surface reaches the melting temperature at 1 J/cm^2. Overall, Fig. 8 indicates that the fluence range from 1 J/cm^2 to 2 J/cm^2 should be explored. Fig. 9 shows the simulated maximum melting depth vs. fluence for a single pulse at the three initial surface temperatures. It indicates that at the low end of the fluence range of interest, the calculated melt depth may not exceed the RF penetration depth.
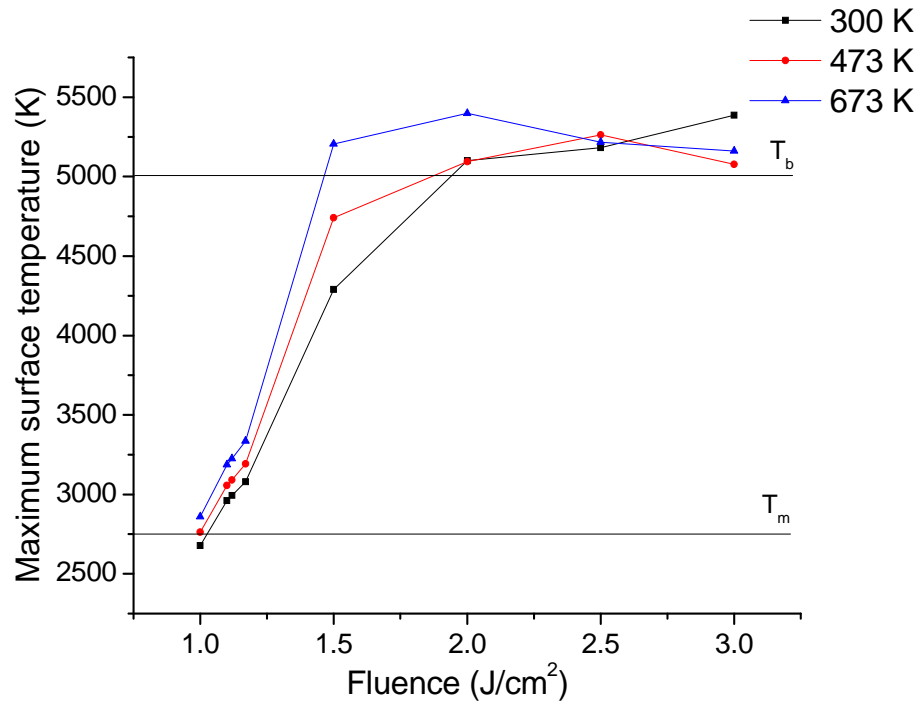
FIG. 8. Calculated peak surface temperature after a single laser pulse of the fluence indicated for three initial temperatures.
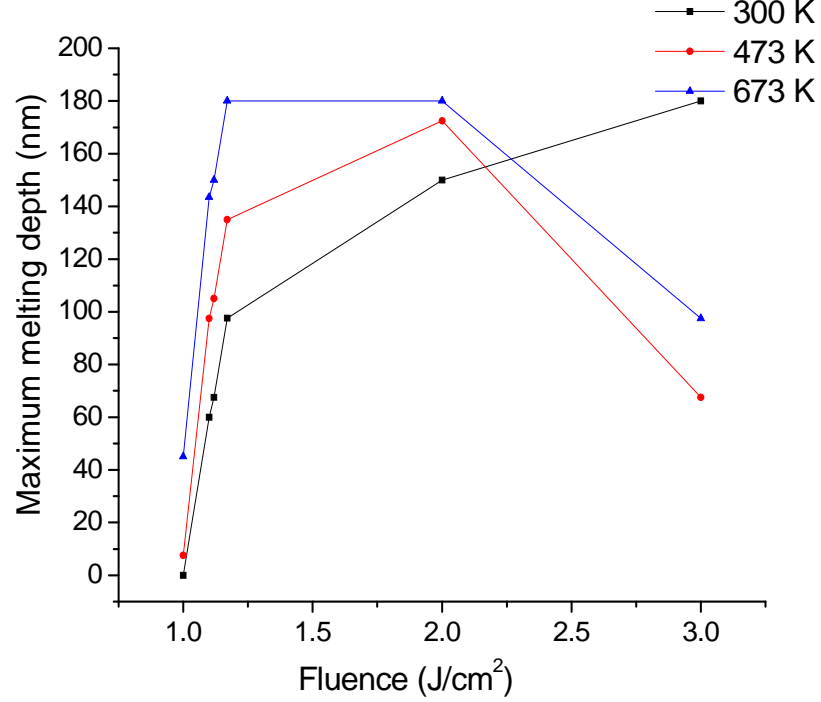
FIG. 9. Calculated maximum melt depth after a single laser pulse
of the fluence indicated for three different initial temperatures.

The time between pulses is ~ 62 µs for the repetition rate of 16 kHz. By the time the
next pulse arrives, the surface temperature is predicted to reach the initial temperature.
Therefore no pulse to pulse heating is expected to occur. Thermal calculations given by
F. Spaepen[64] on metals were used to predict the melt duration at different melt
thicknesses produced by different fluences. The temperature scale is set by the melting
temperature (T_m), which is on the order of 10^3 K. The length scale is set by the melt depth
$(d \cong 10^{-7}$ m). The corresponding temperature gradient is then $\nabla T = T_m/d \sim 10^{10}$ K/m, and
the cooling rate $\check{T} = D_{th} \nabla T/d \sim 10^{12}$ K/s. The life time of the melt can be estimated as
$\tau = T_m/\check{T} = 10^{-9}$ s. Fig. 10 shows the calculated melt lifetime vs. fluence, for a single pulse
at the three initial surface temperatures. Several-fold longer melt lifetimes are predicted
for the elevated initial temperatures. These experiments could not be accomplished with

our current experimental setup, but will be undertaken in the future. The present experiments aim at shallow penetration and short melt lifetime, seeking to maximize the SMM contribution.
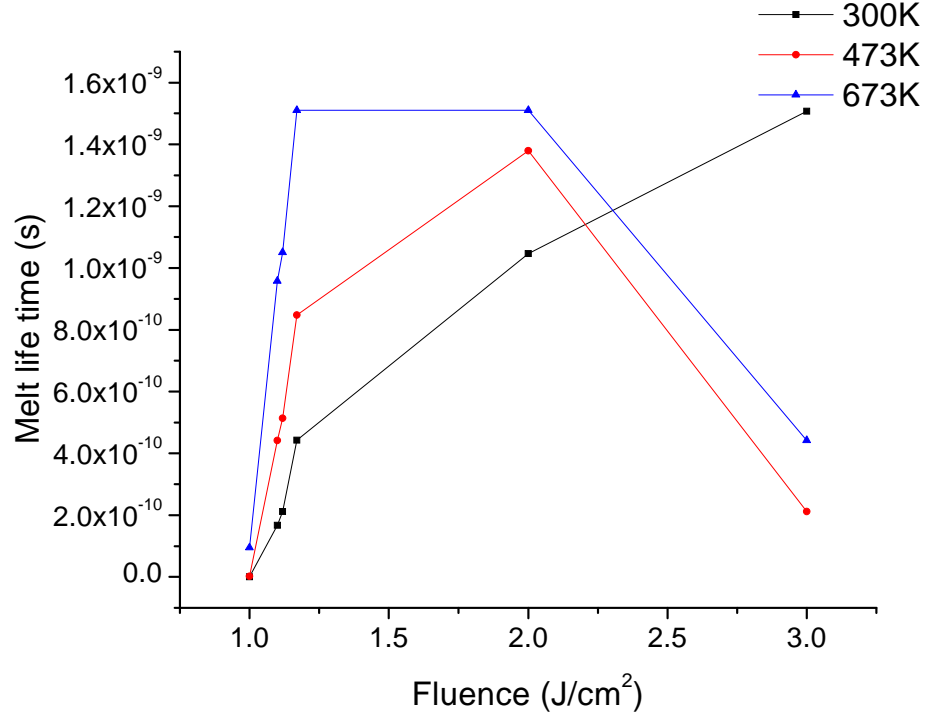
FIG. 10. Calculated melt life time for a single laser pulse of

the fluence indicated for three different initial temperatures.

B.   Experimental setup & procedure

A PVD Products Inc. PLD 5000 system was used for the experiments. Processing was carried out in a vacuum chamber evacuated to 10^{-7} Torr by a rotary backed turbo pump. A reflecting mirror placed in the optical train was used to raster the laser beam over a radial range on the target up to ~1.8 inch. The target pedestals can hold targets of 50 mm in diameter and can rotate individually with a maximum speed of 12 rpm. In each run, three bare niobium discs were mounted and the rotation speed was varied according to the

experiment to obtain the intended pulse accumulation. The laser fluence and pulse accumulation are the experimental parameters explored in this study. The laser beam was incident at an angle of 60° from normal on the rotating niobium target. The laser used was a Spectra Physics "High Intensity Peak Power Oscillator" (HIPPO) Nd:YAG (λ = 1064 nm, E_{max}= 0.430 mJ, τ_p = 15 ns, beam spot $\cong$ 80 μm). The $1/e^2$ beam intensity width (w = 2σ) was determined with a SPIRICON laser beam profiler fitting to a Gaussian transverse intensity distribution $\left(I = I_0 e^{\left(-2r^2/w^2\right)}\right)$. The measured energy per pulse (u) at the target and measured D4σ width ($2w$) are combined to give the measured fluence (H) in J/cm^2 using Eq. (9),

$$H = \frac{u}{\pi w^2} \cos 60^0 \tag{9}$$

where 60^0 is the angle the incident laser beam makes with the surface normal. This angular correction factor gives the energy flux in the normal direction suitable for comparison to the 1-D calculations. Laser fluences of 0.6 to 2.3 J/cm^2 were focused on the niobium target, intending to traverse the temperature from below melting to above boiling, seeking to probe both the SMM and SOM regimes. See Appendix A for more details about the PLD 5000 system and the HIPPO.

Niobium discs, 50 mm in diameter and 2-3 mm thick were cut from polycrystalline sheet stock used for SRF cavities. The samples were degreased in a detergent with ultrasonic agitation, buffered chemically polished in a 1:1:2 solutions of hydrofluoric acid (49%), nitric acid (69.5%), and phosphoric acid (85%), and subsequently rinsed with

ultrapure water followed by a high pressure rinsing for 1 hour. The etching was done for about 2 minutes, removing approximately 10 μm from the surface of each disc.

To make melting evident, the disc surfaces were roughened using 600 grit sandpaper (approximate particle size: 15 μm). The discs were placed in the target holder and the chamber was pumped down to 10^{-7} Torr. The laser fluence was varied from 0.6 to 2.3 J/cm^2, with the number of pulses per unit area constant for the first set of experiments. The target rotation and the repetition rates were adjusted to make sure the number of pulses (same energy per pulse) that overlap on an area remains constant at 75 for this set of tests. To understand the effect of pulse accumulation per area, a second set of experiments were performed by keeping the laser fluence constant at 1.1 J/cm^2 and varying the number of pulses accumulated.

C.   Surface Roughness Measurement

The present work gives results obtained by laser melting to smooth the surface of niobium. The surface topography was investigated with a FE-SEM (Hitachi 4700 SEM/EDX) and with an atomic force microscope (Digital Instruments Nanoscope IV) in tapping mode using silicon tips with 10 nm diameter. A series of 50 μm × 50 μm areas were scanned on each sample.

PSD analysis of AFM data offers a more complete description than the RMS roughness and provides useful quantitative information about the surface topography. Appropriate analytical models aid interpretation and understanding of such morphologies more quantitatively.[65] Here we have adopted the definition used previously for the 2-D PSD of a surface described by its topography z $(x; y)$.[65, 66]

As before,[63] the AFM scan data were detrended by removing a least squares two dimensional first order polynomial from each record before further analysis. In this study, the PSD profiles that were measured at different locations under the same scan condition were averaged separately. A Tukey window transform was applied in order to eliminate spurious high-frequency noise. PSD's were calculated and averaged from at least three scans from different areas. Since the surface after polishing will reveal some level of non uniformity, averaging can effectively and accurately smooth out noise and give more statistically representative PSD.

VI.   RESULTS AND DISCUSSION

Figures 11(a) and 11(b) show SEM and AFM images of the untreated niobium surface. The AFM data indicated a roughness (R_q) of 745 nm. Fig. 12 shows the series of images from the first set of experiments, in which pulse energy was varied for a constant number of pulses. In agreement with the calculations (Fig. 8), fluence less than 1 J/cm^2 produced no visually obvious evidence of surface melting. Still, the roughness was reduced from 745 nm (Fig. 11(b)) to 556 nm (Fig. 12(a)) or 493 nm (Fig. 12(b)). The laser used in these experiments produces a Gaussian beam so that the fluence at the center exceeds the average, perhaps causing a small amount of local melting for fluences less than the value calculated to cause melting by a uniform beam. The fluence per pulse predicted to reach just above the melting point of niobium (Fig. 12(c)) resulted in rounding of sharp edges and smoothening of the surface to a roughness of 202 nm. We interpret these findings as an increasing degree of SSM, with SOM beginning to be evident. Once the fluence per pulse was increased further above the melting point, the surface roughness increased (Fig. 12(d) and 12(e)), as would be expected from

oscillations in the melt under SOM conditions. At sufficiently high fluence, the laser pulse that melts launches mechanical waves that expel melt from the center of the laser beam spot, evident as melt splashing, and promotes increased roughness rather than smoothening.
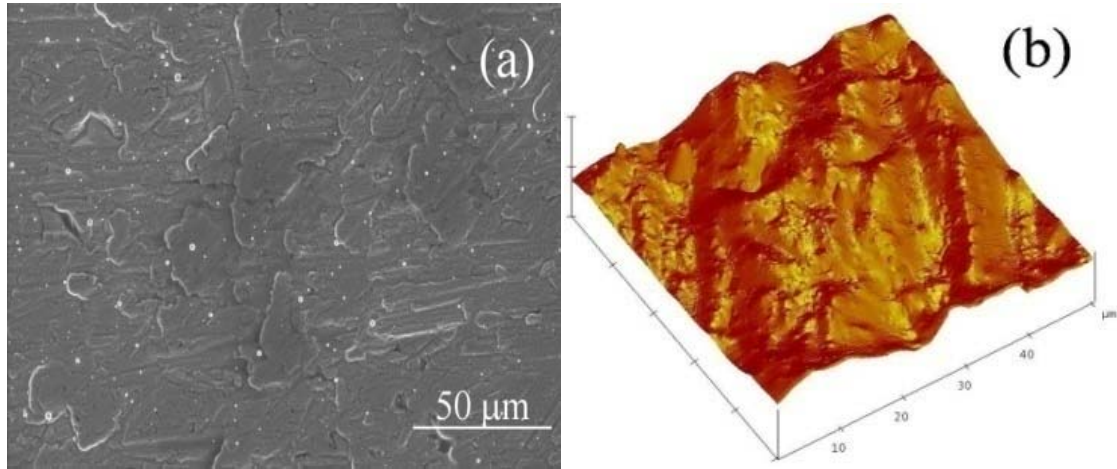
FIG. 11. Untreated niobium surface (before laser processing).

(a) SEM image (b) AFM image (10 μm/div horizontal, 0.5 μm/div vertical).

For fluences >2 J/cm^2 the surface roughness was so high ($\sim$ μm) as to exceed the capabilities of AFM. The SEM image of these materials (e.g., Fig. 14) is consistent with melt splashing. The plot of roughness after treatment (taken from Fig. 12(a-e) and 11(b)) vs the fluence is shown in Fig. 13. In Fig. 13 the error bars are the σ of the results of 5 experimental runs. It can be observed that when the fluence was just above the melting temperature, the roughened surface melted and R_q decreased from 745 nm to 202 nm. The SEM image (Fig. 15) clearly distinguishes between the treated and untreated areas on the surface.

FIG. 12. AFM images of the niobium surface subjected to 75 pulses at the indicated

fluence. (Horizontal scale is indicated on each image; vertical scale is 0.5 μm/div).
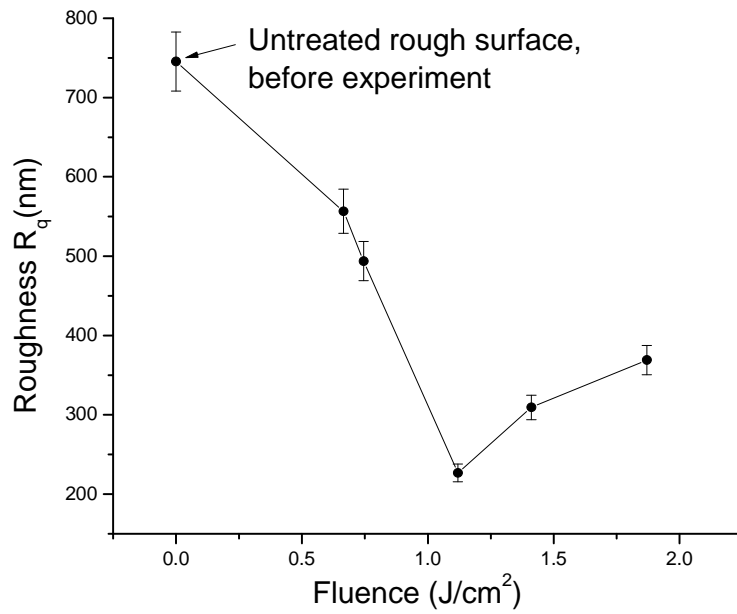
FIG. 13. Surface roughness after 75 laser pulses of the indicated fluence.
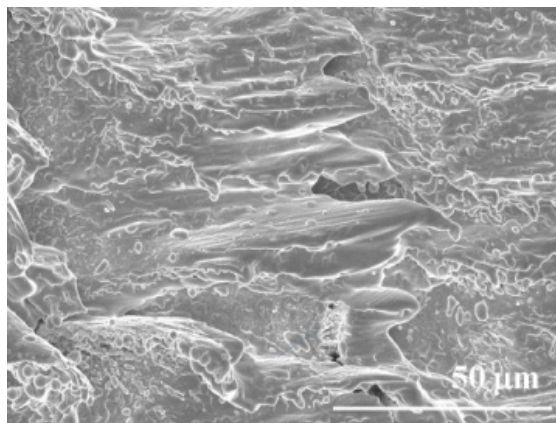
FIG. 14. Increased surface roughness due to higher

laser fluence (> 2.3 J/cm^2) treatment.
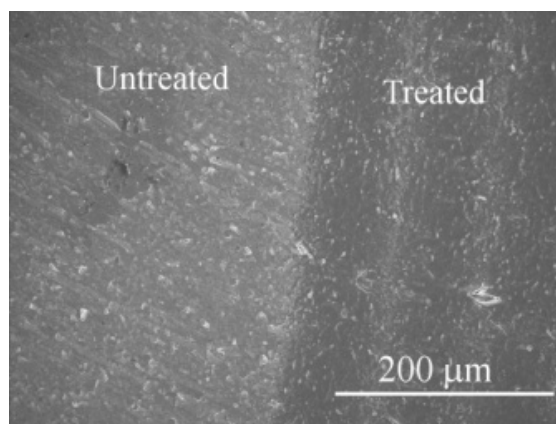
FIG. 15. Interface between the treated (1.1 J/cm^2, 16 kHz and

~75 pulse total per area) and untreated niobium surface.

Fig. 16 shows the series of AFM images from materials irradiated at constant fluence

(1.1 J/cm^2) while varying the total pulses per area. The plot of the roughness vs

cumulative number of pulse per area is shown in Fig. 17. As the cumulative number of

pulses increased, the roughness increased steadily. Though the laser fluence was

nominally just sufficient to reach the melting temperature, the cumulative number of

pulses also is significant for topography. The amplitude of ridge structures forming in the

SOM regime often increases with the total amount of melt time.[33]

FIG. 16. AFM image of niobium surface irradiated by the indicated number of

1.1 J/cm^2 pulses (Horizontal scale: 10 μm/div; vertical scale: 0.5 μm/div).
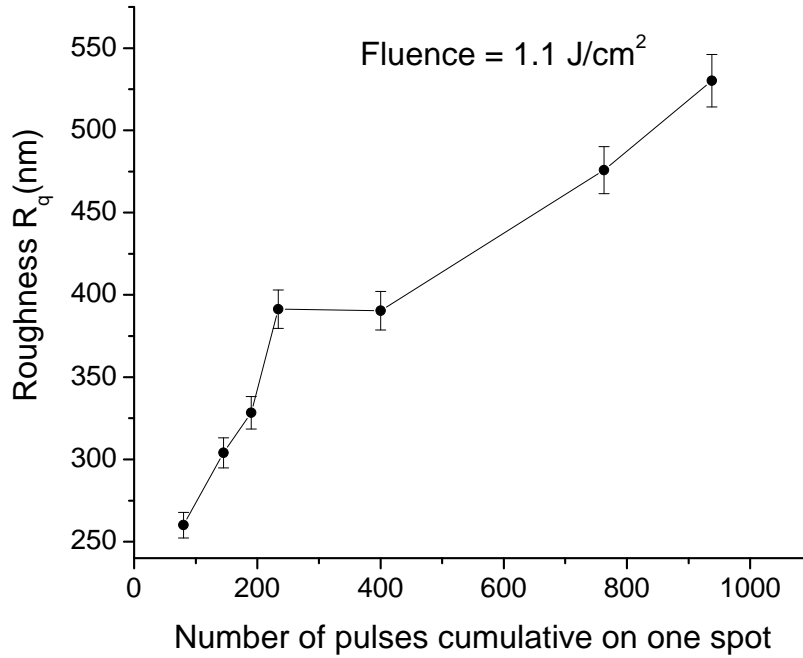
FIG. 17. Surface roughness after irradiation by the

indicated number of pulses at a fluence of 1.1 J/cm^2.

Fig. 18(a) shows the PSD analysis of data from material irradiated with a fixed number of pulses per unit area at a series of fluences. Notice that essentially all the variation occurs at length scales longer than 10 μm, a length scale on the order of the abrasive scratches and the laser-melted spots. The PSD for the fluence predicted to reach just above melting (1.1 J/cm^2) was significantly below all others at longer spatial frequencies (Fig. 18(c)). A similar result was found for fixed pulse fluence with total number of pulses varied (Fig. 18(b)). Expansion of the scale of this figure in the high spatial frequency range (Fig. 18(d)) shows higher PSD values for more pulses.
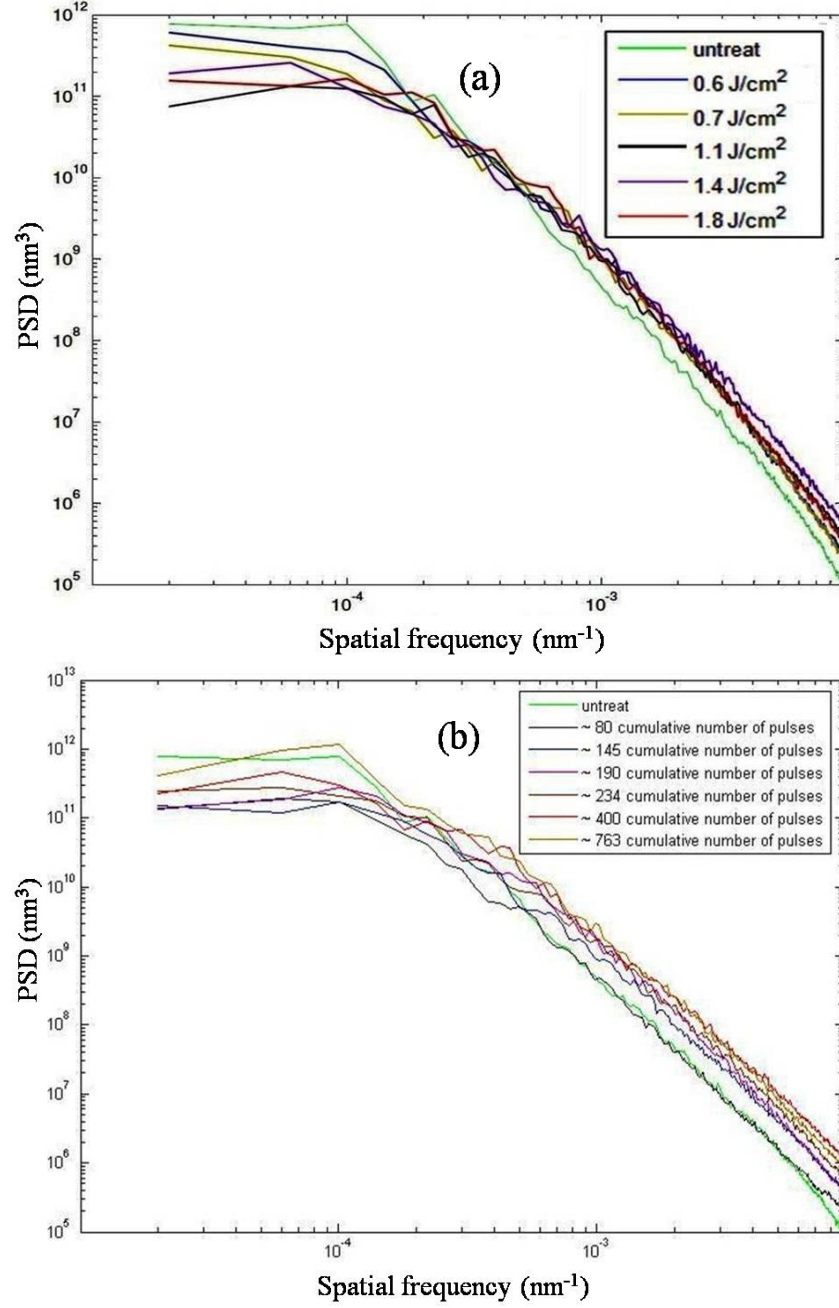
FIG. 18. Power spectral density (PSD) calculated from AFM scans

(a) after irradiation by 75 pulses of the indicated fluence, and

(b) after irradiation by the indicated number of 1.12 J/cm^2 pulses.

Panels (c) and (d) are expansions of (a) and (b), respectively, over the selected

spatial frequency range indicated.

FIG. 18. Continued
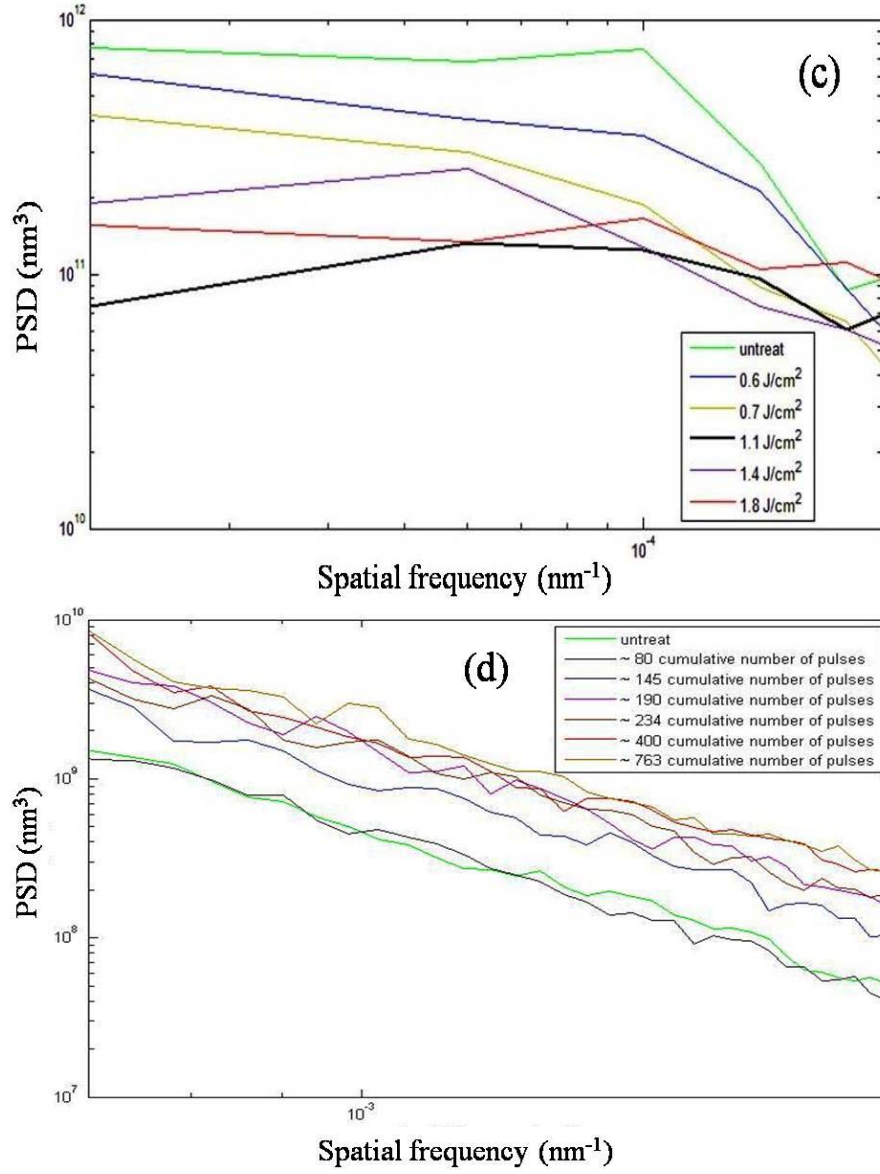
VII. CONCLUSION

Parameters were found for irradiating niobium with a nanosecond laser that produced a significant reduction of surface roughness. PSD analysis of the AFM topography data revealed that a major effect was in the spatial frequency range longer than 10 μm, consistent with the notion of melt oscillations and splashing at high fluence. We conclude

that both SMM and SOM were contributing under the conditions leading to the greatest roughness reduction. A computational model based on the effect of single, spatially-uniform pulses provided useful predictions even though the present experiments used multiple pulses of a Gaussian beam.

CHAPTER 3

LASER NITRIDING OF NIOBIUM FOR

APPLICATION TO

SRF ACCELERATOR CAVITIES

I. INTRODUCTION

The BCS surface resistance of niobium at 1.3 GHz decreases from about 800 nΩ at

4.2 K to 15 nΩ at 2 K.[49] The quality factor Q_0 (2π times the ratio of stored energy to

energy loss per cycle) is inversely proportional to the surface resistance and may exceed

10^{10}. The strong temperature dependence of the resistance is the reason why operation at

1.8 − 2 K is essential for achieving high accelerating gradients in combination with very

high quality factors (and thus energy efficiency). Moreover, superfluid helium is an

excellent coolant owing to its high heat conductivity. The thermal conductivity of

niobium at cryogenic temperatures is strongly temperature dependent and drops by about

an order of magnitude when lowering the temperature from 4.2 K to ~2 K.[67] In principle,

forming the active interior surface from superconducting niobium nitride ($T_c \approx$ 17 K) vs.

the present niobium ($T_c \approx$ 9.2 K) would reduce cryogenic costs and simplify cavity

engineering. The required thickness of the NbN layer needs to take account of the

London penetration depth, reported variously as 85 nm,[68] 176 nm,[69] 270 nm[70] and 375

nm[71] for different NbN preparation schemes.

The Nb-N phase diagram was reported.[72] The desired δNbN extends from ~42 to 50 atomic percent nitrogen. The fcc δ phase converts to the hcp ε phase upon cooling below 1300 °C; ε is not superconducting. Furnace nitriding studies have not been able to obtain δNbN.[73] Quenching from above 1300 °C has yielded some of the desired phase.[74] Rapid thermal processing with a pulsed heat lamp of Nb films on Si in nitrogen yielded some δNbN.[75] Accordingly, we investigated the very rapid cooling attainable by self-quenching in gas/laser nitriding.

P. Schaaf reported laser gas nitriding of iron,[43] aluminum, and titanium,[76] but there appears to have been no work on solid niobium. Compared to furnace nitriding, laser nitriding offers the advantages of a rapid quench, a high nitrogen concentration, fast treatment, and precise position control. Furthermore, materials sensitive to heat and of complex shape can be successfully laser treated. Such considerations motivate our experiment to nitride niobium, obtaining δNbN by laser nitriding.

II. EXPERIMENTAL DETAILS

A.   Fluence range to be explored

In the most desirable process, the niobium surface will be heated to just above the boiling temperature and then cooled rapidly to avoid the δ→ε conversion. We employ computational modeling to predict the time course of the surface temperature as a function of the laser irradiation parameters. The goal is to identify the most promising range of parameters to guide selection of experimental conditions.

Fig. 6, shows the surface temperature profile of niobium vs time, for a single 15 ns pulse of various fluences. The surface temperature profile predicts that surface melting

starts at about 1.1 J/cm^2, and the boiling temperature is reached at 2 J/cm^2. To produce the superconducting δNbN, it is desirable that the fluence brings the surface temperature to just above the boiling point to facilitate reaction with the nitrogen atmosphere, but not to ablate the material. The thickness of the nitride layer is expected to increase with dwell time above melting,[47] so fluences above 2 J/cm^2 were explored.

The photon energy of the laser at the wavelength 1064 nm is only 1.1eV,[77] which is too low to interact directly with the nitrogen atmosphere inside the chamber, which has an ionization energy of 15.6 eV and a dissociation energy of 9.8 eV.[78] The laser intensity is low enough that gas breakdown cannot occur, which needs a threshold intensity of 3x 10^{10} W/cm^2.[32, 79] The threshold can be reduced by two orders of magnitude when a metal surface is place in the nitrogen atmosphere.[80] So we conclude the laser will react only on the niobium surface and not with the nitrogen present in the chamber.

B.   Experimental setup & procedure

A PVD Products Inc. PLD 5000 system was used to carry out the experiments. The niobium discs (2" in diameter, 2-3 mm thickness) were cut from sheet stock used for SRF cavities. The chemical etching was carried out by buffered chemical polishing (BCP) to clean the surface. About 10 microns was removed from the surface of each disc. Fig. 19 shows the picture of the niobium disc before treating with the laser.

Laser processing is carried out in a vacuum chamber evacuated by a rotary backed turbo pump to 10^{-7} Torr. Following evacuation, the chamber can be backfilled with pure nitrogen gas (99.999%) at a pressure ranging from 450 Torr to 620 Torr. The laser irradiation was carried out in this atmosphere. To produce thermal energy for nitriding, a Spectra Physics, "High Intensity Peak Power Oscillator" (HIPPO) nanosecond laser (λ =

1064 nm, E_{max}= 0.430 mJ, τ_p =15ns, beam spot $\cong$ 80 μm) was used. Laser fluences in the range from 2.5 J/cm^2 to 6 J/cm^{2}per pulse were delivered (Fig. 20), intending that the niobium surface reaches above its boiling temperature. In the nitrogen atmosphere, the laser beam is incident at an angle of 60° from normal of the rotating niobium target. The target rotation was kept constant at 9 rpm. The rastering mirror was programmed to scan in such a way that the laser irradiated concentric circles on the niobium target, where reaction with nitrogen gas was intended to form NbN. The combination of the experimental parameters produces concentric circles (graded treatment) on the niobium surface. Fig. 21 shows the laser irradiated niobium disc after the experiment. Thus the number of pulses (same energy per pulse) overlapping is inversely proportional to the radius of the rings, yielding a varying thickness of NbN layer across the nitrided area. Each irradiated ring was subjected to a total laser pulse number per unit area in the range
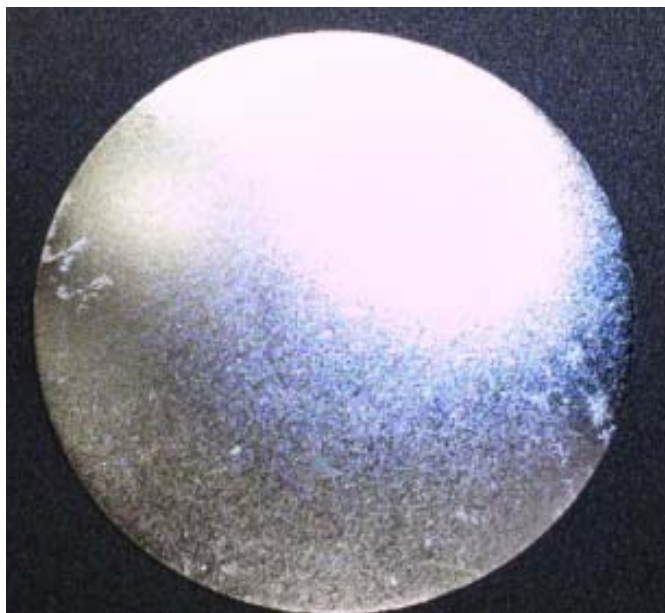
FIG. 19. Nb disc before treatment.
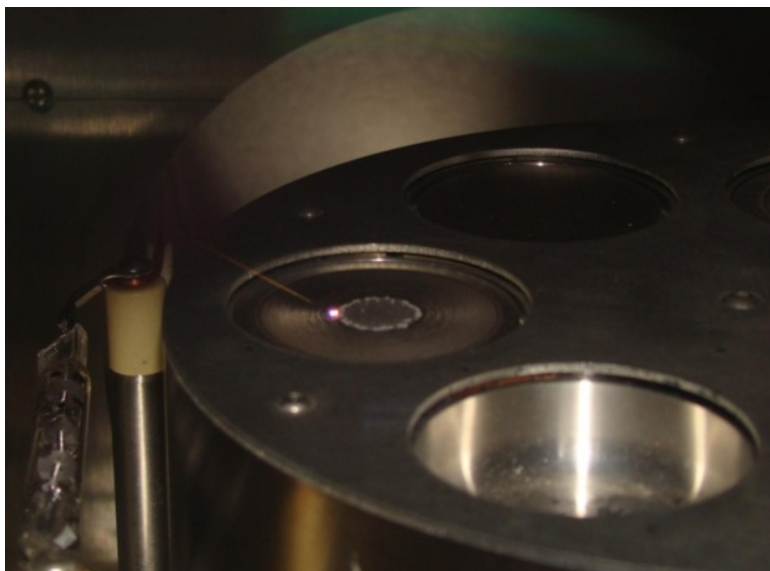
FIG. 20. Nb disc during the treatment.

FIG. 21. Nb disc after the treatment.

of 40 (outer diameter) to 200 (inner diameter). All the conditions used in our experiment are given in Table II.

TABLE II. Preparation conditions for the niobium nitride samples.

Sample number	Repetition rate (KHz)	N_2 press(Torr)	Power (W)	Energy/pulse (mJ)	Fluence (J/cm^2)	Total no. of pulses
1	15	600	5.23	0.349	3.47	60-130
2	15	600	6.47	0.431	4.29	60-130
3	15	550	5.23	0.349	3.47	60-130
4	20	620	8.94	0.447	4.44	70-170
5	20	620	9.7	0.485	4.83	70-170
6	20	620	7.87	0.394	3.92	70-170
7	20	620	5.27	0.264	2.62	70-170
8	20	600	8.94	0.447	4.44	70-170
9	20	550	8.94	0.447	4.44	70-170
10	20	500	8.94	0.447	4.44	70-170
11	20	450	8.94	0.447	4.44	70-170
12	25	620	8.65	0.346	5.96	60-210
13	25	600	9.8	0.392	3.90	60-210
14	25	550	9.8	0.392	3.90	60-210
15	25	500	9.8	0.392	3.90	60-210
16	25	450	9.8	0.392	3.90	60-210
17	30	600	9.1	0.303	3.02	120-260
18	30	600	10.8	0.360	3.58	120-260
19	30	550	10.8	0.360	3.58	120-260
20	30	500	10.8	0.360	3.58	120-260
21	30	450	10.8	0.360	3.58	120-260

III. CHARACTERIZATION OF THE NbN SURFACE

The crystal structure of the surface was determined by x-ray diffraction (XRD) using a Panalytical X'Pert instrument with Co Kα radiation. Phases on the surface were identified by matching the diffraction peaks with the JCPDS (Joint Committee on Powder Diffraction Standards) card. The surface topography was investigated by FE-SEM (Hitachi 4700 SEM/EDX). This was also used to examine in cross-section the thickness of the NbN layer on the Nb. The concentration of nitrogen in the niobium was investigated by energy dispersive x-ray spectroscopy (EDS) on the SEM and wavelength dispersive x-ray spectroscopy on the electron probe microanalysis (EPMA).

IV. RESULTS AND DISCUSSION

The SEM images in Fig. 22(a) show a part of the laser pattern in the form of concentric circles on the niobium surface. Fig. 22(b) shows the treated surface of niobium with 60 total pulses per unit area (sample number 14). From the image, it can be observed that the niobium has reached just above the boiling temperature of niobium. At this temperature, it reacts with nitrogen and undergoes rapid resolidification to form niobium nitride. The surface did not ablate niobium from the bulk material and also had a nanometer-scale surface roughness. Fig. 22(c) shows the treated surface, as the total number of pulses per unit area increases to beyond 150, one observes that the surface of niobium ablates resulting in micron-scale roughness.
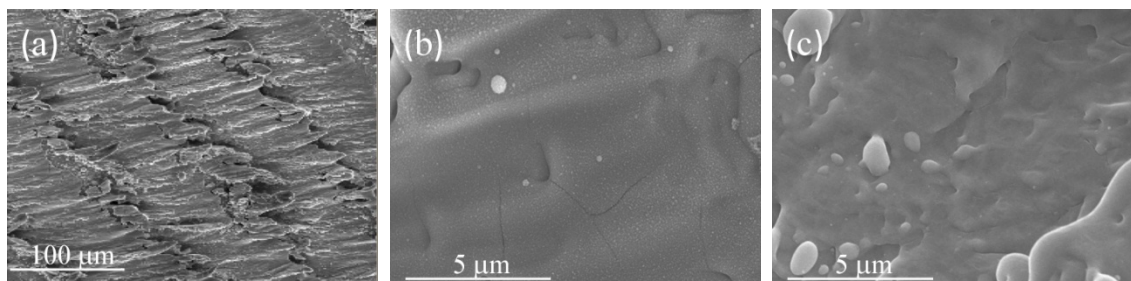
FIG. 22. SEM image showing (a) Part of laser pattern produced on the niobium. (b) Surface irradiated with 60 total pulses per unit area (sample no.14). (c) Surface irradiated with 150 total pulses per unit area (sample no. 14).

Fig. 23 shows the XRD patterns of samples 13, 14 and 15, treated at 600, 550 and 500 Torr nitrogen pressure respectively. They show the presence of different NbN phases, including the superconducting δNbN, phase. There is a shift observed in the position of the niobium peak of sample number 14, where δNbN alone was detected. The reason for this shift of niobium peak compared to other samples is the strain induced by the high concentration of nitrogen to form δNbN (Fig. 23). All other samples, which were prepared by varying pressure, fluence, power and energy per pulse, either had a combination of different phases of NbN or lacked the signature of NbN itself.

The total accumulated pulses varied as a function of radius for all samples. To explore for any effect on composition, the N and Nb content for sample 14 were determined by EPMA along a radius (Fig. 24). The values are constant. They are plotted as atomic percentage, uncorrected for all instrument effects. To calibrate these values, we determined the ratio apparent atomic percentage of N and Nb in NbN reference material (Alfa Aesar 12146) to be 0.69, the same as in the plots.
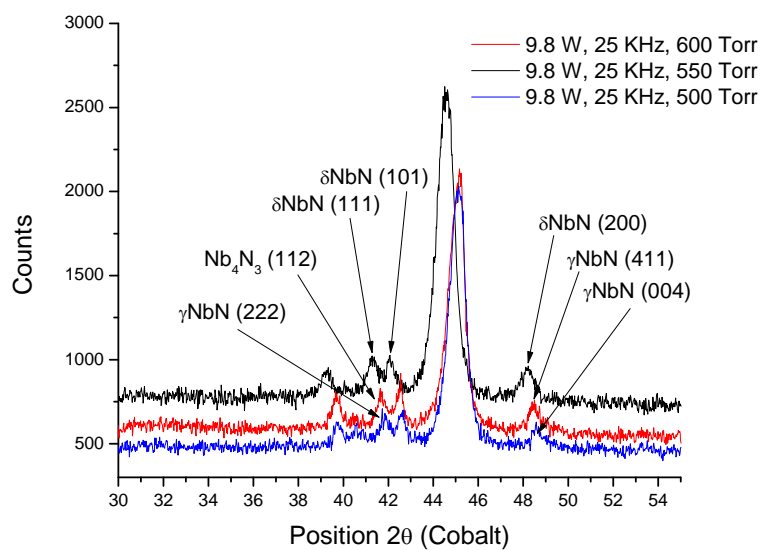
FIG. 23. XRD spectra showing the presence of different phases of NbN

(Sample no. 13 and15) and presence of δNbN (sample no.14).
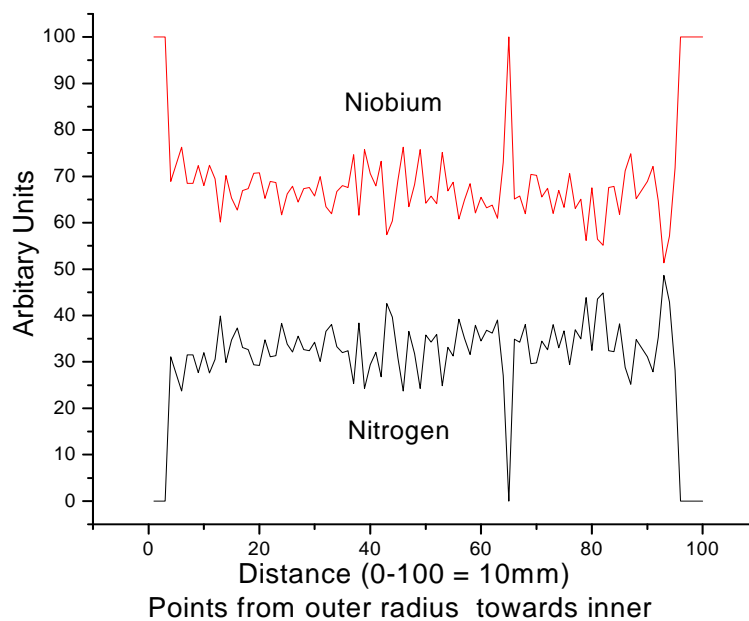
FIG. 24. Radial dependence of atomic concentration of Nb

(upper trace) and N (lower trace) from sample no. 14.

Experiments repeated to check the reproducibility of producing phase-pure δNbN, with the same experimental parameters (Repetition rate = 25 KHz, N_2 pressure = 550 Torr, power = 9.8 W, fluence = 3.9 J/cm^2), were successful.

Fig. 25 shows the SEM of the cross section of sample number 14, to view the nitrided layer and the bulk niobium. Elemental analysis to differentiate the nitrided part and the niobium part was performed by energy dispersive x-ray spectroscopy (EDS) in the SEM (not shown). The nitrided part had the signature of nitrogen and niobium, whereas the niobium region had just the signature of niobium alone. By the scale on the image, the thickness of the nitrided area can be measured as about 10 microns. The simulation (Fig. 6) predicts that delivering a single pulse of fluence greater than 2 J/cm^2 to Nb surface, raises the surface temperature of the niobium to the boiling temperature. It is expected that niobium reacts with nitrogen atmosphere forming NbN only when the fluence is more than 2 J/cm^2 (ie when the niobium surface reaches its boiling point). The XRD analysis shows NbN peaks only when the fluence is above 2 J/cm^2. δNbN was found at a fluence of 3.9 J/cm^2 and nitrogen pressure of 550 Torr.
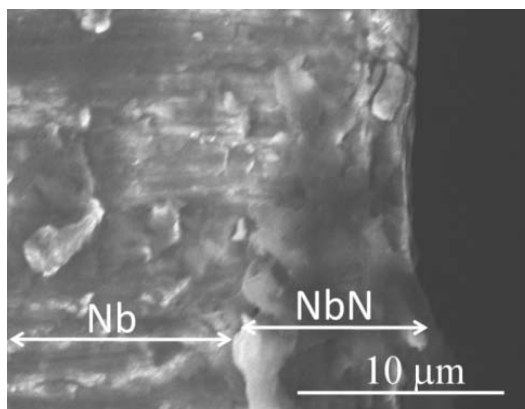
FIG. 25. Cross sectional image of sample no. 14,

indicating the position of the nitrided layer.

V. CONCLUSION

These results provide evidence of the successful nitriding of niobium to produce a superconducting niobium nitride (δNbN) surface layer by rapid thermal treatment using a nanosecond laser. The atomic concentration of N and Nb, did not change drastically with the change of number of pulse overlap per area. But comparing the surface morphology, it was clear that a lesser number of pulses overlapping per area produced less roughness (surface looks smoother), than with a higher number of pulses. The surface temperature simulation results were consistent with the measured threshold for laser nitriding as indicated by the NbN peaks detected through the XRD data. The most likely reason for success in producing phase-pure δNbN compared to previous work is the high cooling rate that avoided conversion of δNbN to the non-superconducting hexagonal ε phase.

CHAPTER 4

PULSED LASER DEPOSITION OF

NbN THIN FILMS

I. INTRODUCTION

At present, the material used in superconducting RF cavities is niobium, with a critical temperature $T_c = 9.2$ K. To reach very high accelerating fields (50-100 MV/m), other materials, having T_c and critical magnetic field higher than niobium, may be needed. The interest in the materials with a critical temperature higher than niobium is connected to the relation between T_c and the RF surface electrical resistance (an exponential function of T_c/T) and to the fact that the accelerating field can be increased, other factors being equal, as the surface resistance decreases. Therefore, high values of T_c could allow one to reach higher accelerating fields, or to have reduced the thermal losses at the same accelerating gradient. Delta phase niobium nitrides are potentially useful materials for superconducting applications due to their high critical temperature ($T_c \cong 17$ K) and to the potentially easy preparation process.[81]

The niobium nitrides have been well developed as thin films by several methods such as vacuum arc deposition,[82-85] reactive magnetron sputtering,[86-92] ion beam assisted processes,[93-95] with an unbalanced magnetron,[96] and by pulsed laser deposition.[97] Using different techniques, NbN thin film was deposited on different substrates such as MgO,[97-100] copper,[101] niobium,[71,102,103] sapphire,[81,104] silicon,[99] and fused quartz

plates.[100,105] The properties of the thin films were studied, with the result that mixed phases of NbN were produced in the thin films.

Using pulsed laser deposition, R.E. Teece, et.al, reported the growth of NbN superconducting films on a MgO substrate by using a KrF excimer laser (λ = 248nm) in a 10% H_2 and 90% N_2 background gas.[98,106] V. Boffa, et.al.,[107] reported producing a NbN superconducting films on a MgO substrate by using a Nd:YAG laser (λ = 532nm) deposited in a pure N_2 atmosphere. Throughout a literature search no work on depositing superconducting NbN thin film either on Nb or Cu using pulsed laser deposition with a pure N_2 atmosphere was found. Here I present the initial work performed on depositing δNbN thin film on a Cu and a Nb substrate in pure N_2 atmosphere using a HIPPO (λ = 1064 nm) and COMPEX Pro 205 excimer laser (λ =248 nm) respectively.

The decision to use a copper substrate was based on the low cost, and simple surface preparation, as well as a higher thermal conductivity (485W/mK at 4.2 K) compared to (28W/mK at 4.2 K/RRR = 40) for Nb, which improves heat transfer to the He-bath.[108] The risk of quenching is thus greatly reduced and operational safety increased.[109]

II. EXPERIMENTAL DETAILS

The PVD Products Inc. PLD 5000 (Fig. 26) at Jefferson Lab, and PLD MBE 2000 (Fig. 27) at PVD Products Inc., Boston, were used to carry out the following experiments.

Niobium discs of two different dimensions (50 mm in diameter, 2-3 mm in thickness and 50 mm in diameter, 6-7 mm in thickness) cut from a reactor grade multigrain niobium sheet used for SRF cavities were used in two different PLD systems. The samples were degreased in a detergent with ultrasonic agitation, and buffered chemically

polished in a 1:1:2 solutions of hydrofluoric acid (49%), nitric acid (69.5%), and phosphoric acid (85%), subsequently rinsed with ultrapure water followed by a high pressure rinsing for 1 hour. The etching was done for 2 minutes, removing approximately 10 μm from the surface of each disc. These discs were used both as target and substrate. An oxide free copper sheet of 2-3 mm thickness was cut into a disc of 50 mm in diameter. These discs were then polished using Buehler Ecomet 4 Grinder Polisher. These samples were polished using 320, 600 grit papers followed with 0.02 μm silicon liquid to achieve final surface roughness of ~12 nm, which was measured through AFM. These discs were used as substrate.

FIG. 26. PVD Products Inc. PLD 5000.

The chamber was pumped down to 10^{-7} Torr as a base pressure. Before starting the deposition the oxide layer on the substrates were removed by heating the substrates (niobium and copper discs) at different temperatures and time, and cooling to room

temperature where the deposition was performed accordingly. The presence of oxygen on the substrate before the deposition was not studied. The experiments were performed by

FIG. 27. PVD Products Inc. PLD MBE 2000.

varying the substrate bake temperature, deposition time, and nitrogen pressure. Substrate-target throw distance, fluence and rastering pattern were kept constant throughout the experiment. The nitrogen pressure was varied from 10^{-4} to 10^{-1} Torr. To deposit a thin film on niobium, the substrate temperature was varied from room temperature to 900 $^\mathrm{o}$C and to deposit a thin film on copper, the substrate temperature was varied from room temperature to 500 $^\mathrm{o}$C. The substrate heater in the PLD 5000 was restricted to 500 $^\mathrm{o}$C, so the PLD MBE 2000 was used to deposit niobium nitride thin film on niobium, by increasing the substrate bake temperature to 900 $^\mathrm{o}$C. Deposition time was varied from 30 mins to 120 mins. Table III and IV shows the different experimental parameters used for the experiment.

The beam spot from the COMPEX Pro 205 laser was measured using a burn paper. The burn paper was kept on the target to exactly measure the beam spot on the target. Fig. 28 shows the burn mark of the laser beam spot. The beam spot (area = 4.290 mm^2) was measured using the KH-3000VD high resolution digital-video microscopy system (HIROX)

FIG. 28. Burn mark image produced by COMPEX Pro 205

on the burn paper to measure the beam spot.

To ablate niobium from the target, a Spectra Physics, "High Intensity Peak Power Oscillator" (HIPPO) nanosecond laser (λ = 1064nm, E_{max}= 0.430mJ, τ_p =15ns, beam spot $\cong$ 80μm) at Jefferson Lab and Coherent "COMPEX Pro 205" excimer laser (λ = 248 nm, E_{max}= 550 mJ, τ_p = 20 ns, beam spot $\cong$ 4.29 mm^2) at PVD Products Inc., were used. The maximum energy per pulse produced by COMPEX Pro 205 was 550 mJ. So 550 mJ per pulse was selected to perform the experiments. The laser beam was incident at an angle of 60° from normal of the rotating niobium target. The target rotation was kept constant at 9 rpm (PLD 5000) and 30 rpm (PLD MBE 2000) throughout the experiment. The

substrate was rotated at 6 rpm and 15 rpm respectively. The maximum target rotational speed (rpm) for PLD 5000 and PLD MBE 2000 is 12 and 50 respectively and maximum substrate rotational speed for both systems is 50 rpm. The laser beam was uniformly rastered on the target.

TABLE III. Deposition parameters on the copper disc.

Deposition Parameters:		Laser Parameters:
Substrate = 2" Copper disc		Laser : HIPPO
Substrate bake time = 30 min		Wavelength : 1064 nm
Deposition time = 30 min		Power : 12.09 W
Base pressure = 10^{-7} Torr		Repetition rate : 25 kHz
Sample number	N_2 pressure (mTorr)	Substrate bake temperature(^{o}C)
1		Room temp.
2		300
3	1	400
4		500
5		Room temp.
6		300
7	3	400
8		500
9		Room temp.
10		300
11	8	400
12		500

TABLE IV. Deposition parameters on the niobium disc.

Deposition Parameters:	Laser Parameters:
Substrate = 1" Niobium disc	Laser : HIPPO
Substrate bake time = 30 min	Wavelength : 1064 nm
Deposition time = 30 min	Power : 12.09 W
Base pressure = 10^{-7} Torr	Repetition rate : 25 kHz

Sample number	N_2 pressure (mTorr)	Substrate bake temperature(^{o}C)
1		Room temp.
2		300
3	1	400
4		500
5		Room temp.
6		300
7	3	400
8		500
9		Room temp.
10		300
11	8	400
12		500

Table IV. Continued

Deposition Parameters:	Laser Parameters:
Substrate = 1" Niobium disc	Laser : HIPPO
Substrate bake time = 30 min	Wavelength : 1064 nm
Deposition time = 30 min	Power : 12.09 W
Base pressure = 10^{-7}Torr	Repetition rate : 25 kHz

Sample number	N_2 pressure (Torr)	Deposition time (min)
13	3×10^{-3}	90
14		120
15	3×10^{-2}	90
16	6×10^{-2}	120
17	3×10^{-1}	120

III. CHARACTERIZATION OF THE NbN THIN FILM

The crystal structure of the surface was determined by x-ray diffraction (XRD) using a Panalytical X'Pert instrument with Co Kα radiation. Phases on the surface were identified by matching the diffraction peaks with the JCPDS (Joint Committee on Powder Diffraction Standards) card. The concentration of nitrogen in the niobium and copper was investigated by energy dispersive x-ray spectroscopy (EDS) on the SEM. The surface topography was obtained with a Digital Instruments Nanoscope IV atomic force microscope in tapping mode using silicon tips with a diameter of 10 nm. A series of 50 μm × 50 μm areas was scanned on each sample. The beam spot of the excimer laser was measured using optical microscopy (HIROX). The thickness of the film was measured using both Tensor K15 Surface Profilometer and AFM.

IV. RESULTS AND DISCUSSION

Fig. 29 shows the atomic percentage of nitrogen, oxygen and copper compared to niobium, which was deposited on a copper substrate using a HIPPO ns laser. The presence of high oxygen percentage tells that the material may have oxidized when it was exposed to air after the experiment. As the oxygen content on the substrate was not determined, it is also possible that the measured oxygen resided on the substrate before processing. The content of nitrogen and niobium was examined on the substrate, but the niobium did not react with nitrogen gas to form niobium nitride. This was observed on all the samples (Fig. 31) prepared, showing deposition of NbN on copper was not successful. Further experiments are needed: increasing the deposition time, substrate bake temperature from 100 $^{\circ}$C till 200 $^{\circ}$C, substrate-target throw distance, letting the substrate to cool down to room temperature completely and varying the rastering pattern.
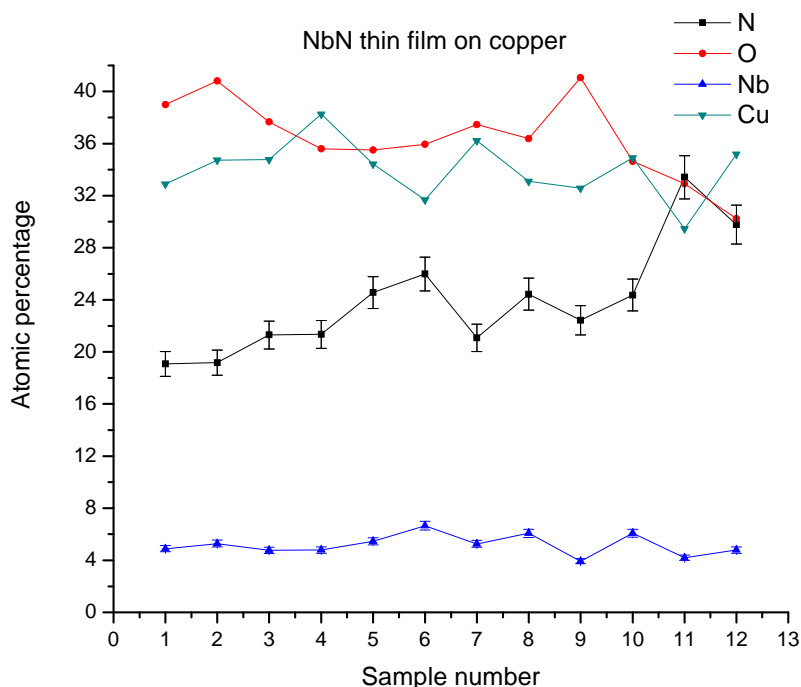
FIG. 29. Atomic percentage of various element in the thin film on copper substrate.

Fig. 30 shows the atomic percentage of nitrogen and oxygen compared to niobium which was deposited on a niobium substrate using both HIPPO and COMPEX Pro 205. Nitrogen was not observed on the thin films deposited (sample 1- 13) using the ns HIPPO, providing evidence that niobium nitride could not have been developed in these samples. Due to the fact that the substrate bake temperature was limited to 500 °C or the substrate bake time was limited to 30 minutes, the deposition time was not enough to form NbN thin film on niobium. It is important to further explore these parameters to observe δNbN on niobium. When the samples (sample number 14-18) were prepared using COMPEX Pro 205, the ratio of nitrogen to niobium was sufficient to indicate niobium nitride. This shows evidence that the substrate bake temperature, bake time and deposition time may be important parameters for forming the niobium nitride thin film.

Further, the films were deposited only after the substrate (niobium) was cooled down to room temperature.
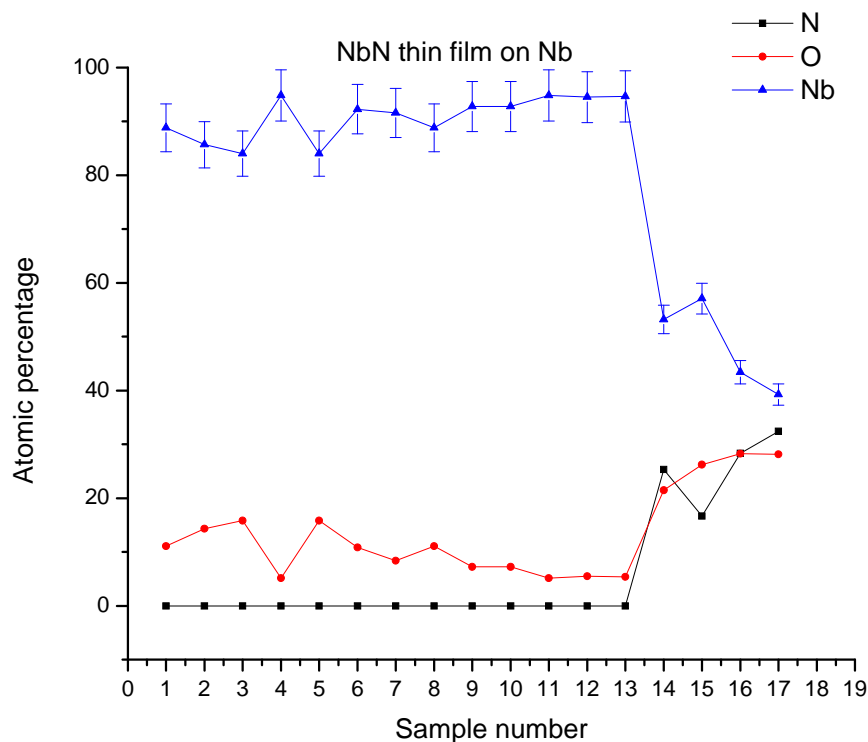
FIG. 30. Atomic percentage of thin film on niobium substrate.

The XRD spectra of thin film deposited on copper at different nitrogen atmosphere pressure are shown in Fig. 31. The XRD spectra do not show evidence of any phase of NbN. The XRD spectra of NbN thin film on niobium using COMPEX Pro 205 at two different deposition times and keeping the magnitude of nitrogen atmosphere pressure constant are shown in Fig. 32. δNbN phase was observed, but inside the same peak location, it shows δNbN at 45.070^{o}, αNbN at 45.105^{o} and niobium at 45.155^{o}. As the deposition time increased, the thickness of the δNbN film and the intensity of the peak also increased. This experiment shows a successful method to produce δNbN on niobium.

We hope that further exploration keeping the magnitude of nitrogen pressure constant and by varying substrate-target throw distance and substrate bake temperature, would produce δNbN phase alone on the niobium, which is the ultimate goal of this experiment. Since the presence of nitrogen was not observed in EDS, the XRD analysis was not performed on niobium, which was prepared using a ns HIPPO laser.
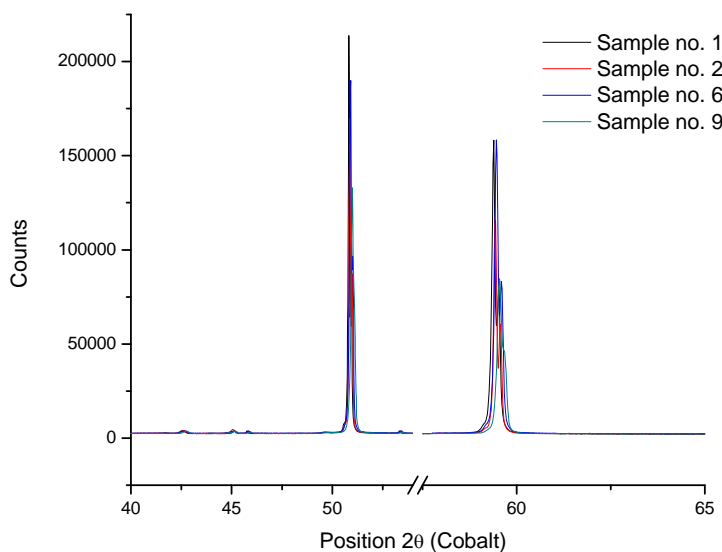
FIG. 31. XRD spectra showing no evidence of NbN on copper substrate deposited at room temperature and 300°C bake temperature.

Fig. 33 and Fig. 34 shows the AFM and SEM image respectively of the thin film samples deposited on a copper substrate (Fig. 33(a)) using the HIPPO ns laser, on a niobium substrate (Fig. 33(b)) using the HIPPO ns laser, and on niobium substrate (Fig. 33(c)) using the COMPEX Pro 205. The AFM data indicated a roughness (R_q) of 83.81 nm (Fig. 33(a)), 34.32 nm (Fig. 33(b)), and 322.83 nm (Fig. 33(c)) respectively.
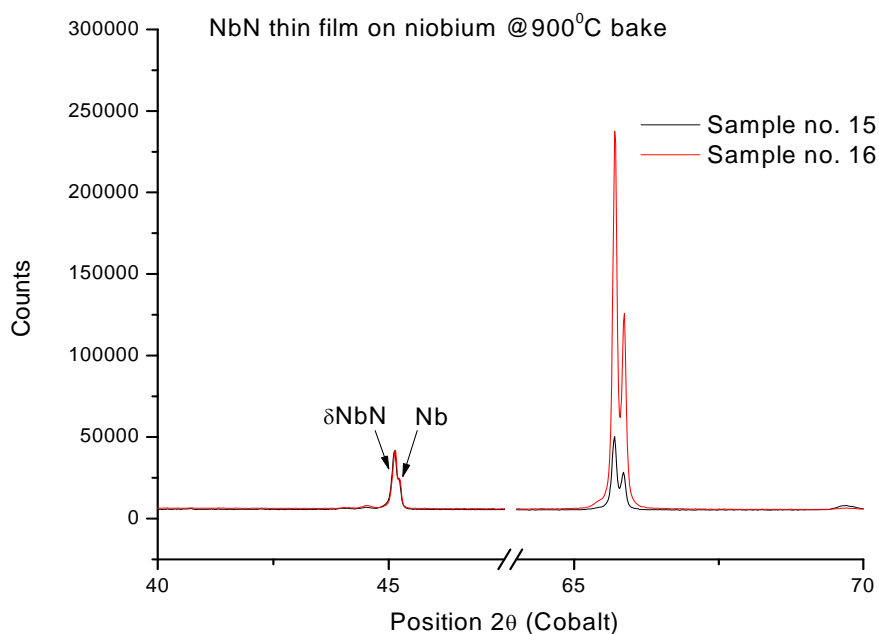
FIG. 32. XRD spectra showing the presence of presence of

δNbN, Nb and αNbN on niobium substrate.
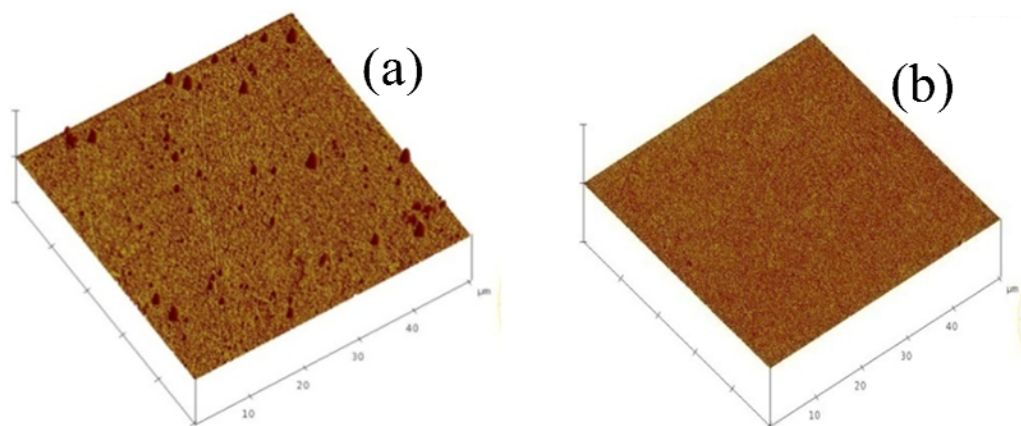
FIG. 33. AFM images of (a) Thin film on copper using the HIPPO (sample number 2). (b)Thin film on niobium using the HIPPO (sample number 6). (c) NbN thin film on niobium using the excimer laser. (sample number 15).

FIG. 33. Continued
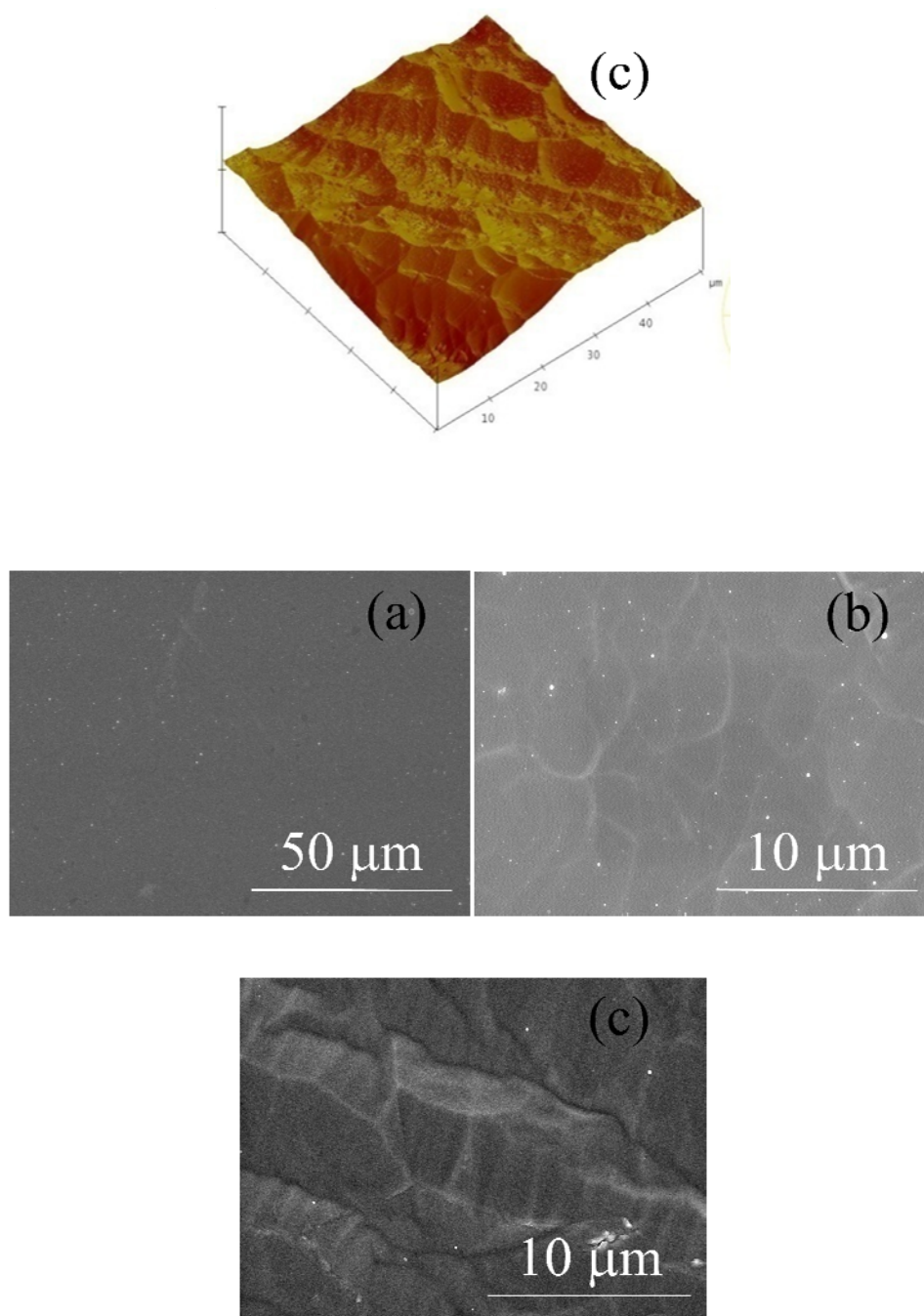
FIG. 34. SEM images of (a) Thin film on copper using the HIPPO (sample number 2). (b) Thin film on niobium using the HIPPO (sample number 6). (c) NbN thin film on niobium using the excimer laser (sample number 15).

Fig. 35 shows the thickness measurement obtained using the surface profilometer on three different thin film samples deposited on: copper substrate (Fig. 35(a)) using the HIPPO laser, on niobium substrate (Fig. 35(b)) using the HIPPO laser, and a niobium substrate (Fig. 35(c)) using the COMPEX Pro 205. As the substrate was baked at high temperature, preparing a step on the surface of the substrate using some mask was not possible. So the thickness of the thin film was measured near to the edge of the sample, where it was placed on the substrate holder. Thus a clear step was not observed. Fig. 35(a) shows the line scan on the edge of the thin film prepared using the HIPPO and a copper substrate, which gives the average thickness of the thin film of 5-15 nm. A thickness of 70-95 nm (Fig. 35(b)) was measured on the thin film deposited on niobium for 90 min using excimer laser and a thickness of 190-260 nm (Fig. 35(c)) on the thin film deposited on niobium for 120 min using excimer laser. Fig. 36 shows the AFM image which differentiates the border of the thin film and the substrate, which also shows that it was not a proper step.

Fig. 37 shows the images of scotch tape measurements for adhesion properties of thin film on two samples deposited using the COMPEX Pro 205 on a niobium substrate. A small area on the surface of the sample was scratched in an island formation using a razor and a scotch tape was adhered and pealed out to see if the thin film from the scratched area was removed. Fig. 37(a) and 37(c) are the image on the sample 14 and 15 before the tape was adhered. Fig. 37(b) and 37(d) are the image on the sample after the tape was removed. As the thin film was not removed from the surface, it shows that the thin film had good bonding with the substrate
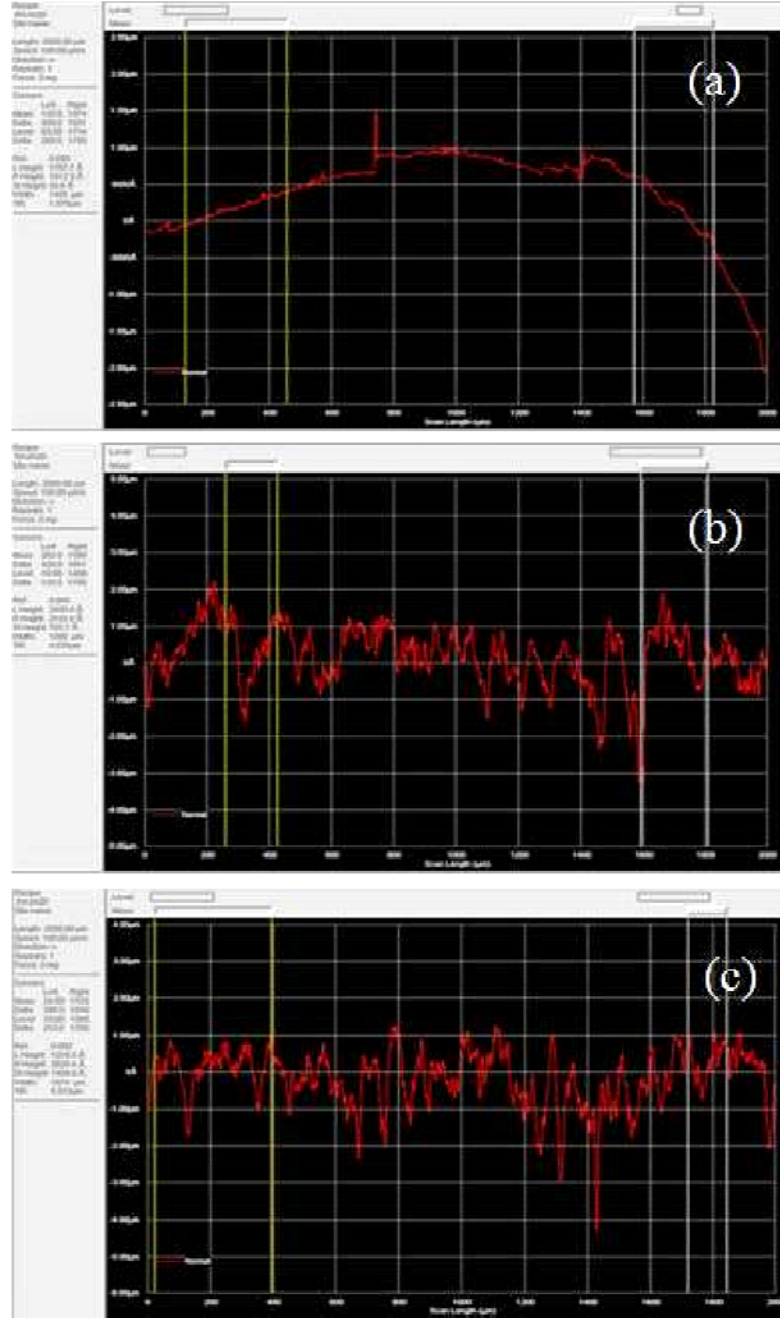
FIG. 35. Thickness measurements using surface profilometer on (a) Thin film on copper

for 30 min (sample number 2) (b) Thin film on niobium for 90 min (sample number 15)

(c) NbN thin film on niobium for 120 min (sample number 16)
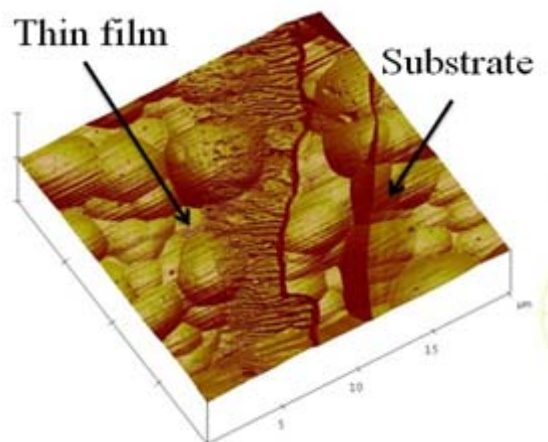
FIG. 36. AFM image showing the border of thin film and

the niobium substrate (sample number 15)
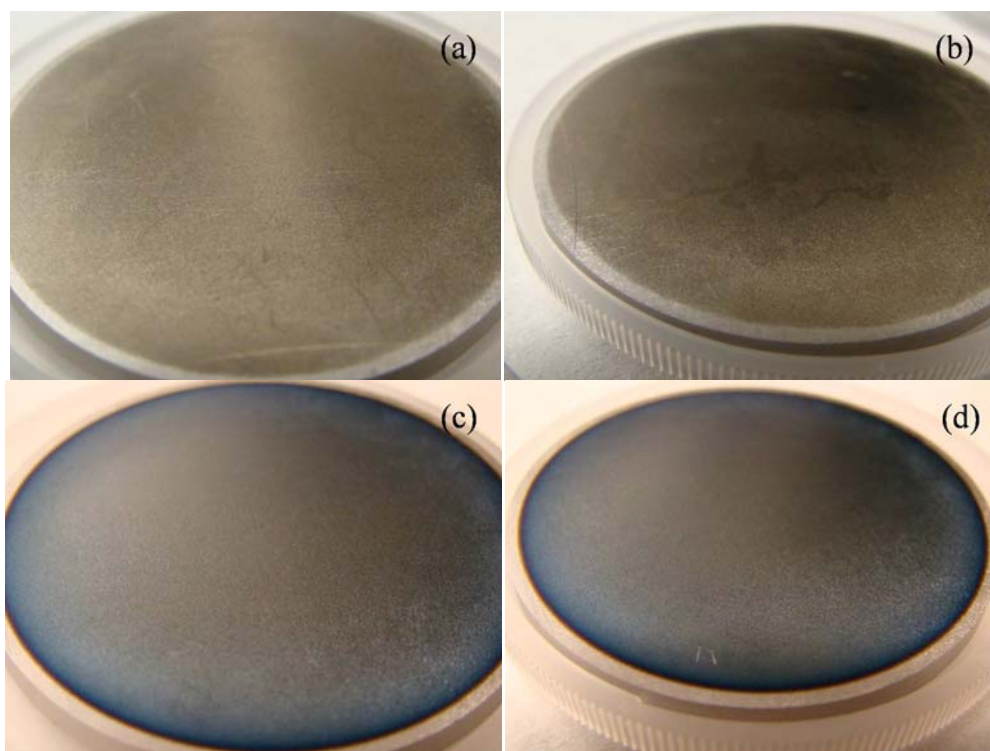
FIG. 37. Adhesion measurements with scotch tape on thin film on niobium substrate.

(a) & (c) before tape was adhered, (b) & (d) after tape was adhered

V. CONCLUSION

NbN thin films were deposited on both copper and niobium discs using pulsed laser deposition method. Deposition of delta phase NbN thin film on niobium was successful. The experiment reveals the basic parameters for obtaining δNbN on niobium and the time frame when to start ablating niobium. Further studies may lead to δNbN alone and avoid other phases of NbN on the niobium substrate. Further exploration is needed to understand the technique to deposit NbN thin films on a copper substrate.

CHAPTER 5

RESONANT INFRARED PULSED LASER DEPOSITION OF CYCLIC OLEFIN COPOLYMER FILMS

I. INTRODUCTION

Organic polymers are emerging as a class of materials having many possible applications in electronics and opto-electronics.[110] The developments in these devices such as thin film transistors, polymer light emitting diodes (PLEDs), and organic light emitting diodes (OLEDs) have highlighted the need for protective and barrier thin films. The importance of barrier and protective coatings in extending the lifetime and reliability of OLEDs is well documented.[111] The properties of the barrier layers should include being impervious to water vapor and air through millions of operational cycles over the lifetime of the devices, and also being optically transparent. A polymer that has recently attracted considerable interest as a barrier material is cyclic olefin copolymer (COC). The COC chain consists of ethylene and norbornene, and the glass transition temperature can be varied from about $75^{o}C$ to $170^{o}C$ by changing the ratio between the two monomers.[112] Because the bulky cyclic olefin units randomly or alternately attach to the polymer backbone, the copolymer becomes amorphous and shows the properties of high glass-transition temperature (T_g) optical clarity, low shrinkage, low moisture absorption, and low birefringence.[113-115] With these properties, the application of cyclic olefin copolymer

has now been extended to production of plastic lenses, optical storage media, and also acts as a barrier material.

Cyclic olefin copolymer is insoluble and thus cannot be deposited by spin coating. A few attempts have been made to deposit organics and polymers using infrared pulsed laser deposition.[116] Picosecond tunable infrared wavelength lasers were not broadly used for these applications until 2001.[117] Since then, a variety of thermoplastic, thermoset, conducting and semiconducting polymers has been carried out. Significantly, tunable infrared laser has been useful to grow thin films of insoluble polymers that are almost impossible otherwise *e.g.*, polytetrafluoroethylene (Teflon®), [118] polyimide[119] and metal or dielectric nanoparticles.[120] Because the mid-infrared photons have energies well below those required to break the bonds that connect monomer units, resonance infrared laser irradiation ablates polymers without photo fragmentation, unlike ultraviolet pulsed laser deposition (UV-PLD).

Here we report on vapor-phase deposition of a barrier and protective polymer, cyclic olefin copolymer (COC), potentially useful in fabrication of OLEDs by resonant infrared pulsed laser deposition (RIR-PLD) using the free electron laser (FEL) and compared the results with those obtained from off-resonant infrared pulsed laser deposition using a nanosecond high power Q-switched laser, both at Jefferson Laboratory. The deposited films were characterized by FE-SEM (Hitachi 4700 SEM/EDX), Digital Instruments Nanoscope IV atomic force microscope, Fourier-transform infrared spectrometry, and HIROX. Also the ablation fluence threshold of FEL photons on COC was measured. These experiments give a preliminary indication of the laser parameters needed to make RIR-PLD deposition of barrier layers of COC a viable commercial process.

II. LASERS

Two different laser sources were used in these experiments. The first was the upgraded Jefferson Lab free-electron laser (FEL), a wavelength-tunable, sub picosecond, infrared light source offering a combination of high repetition rate and high power per pulse and capable of delivering average powers in excess of 10 kW.[121] The FEL, shown schematically in Fig. 38(a), is driven by a superconducting energy-recovery linear accelerator (ERL), a small higher-current relative of the continuous electron beam accelerator facility (CEBAF) used for nuclear physics. In the ERL, each electron circulates once rather than being stored for many cycles, as it would in a typical synchrotron light source. The electron energy is recovered and almost immediately recycled to a fresh electron in the ERL. The source of the accelerated electron bunches that produce the laser beam as they pass through the wiggler is a DC electron gun with a cesiated GaAs photocathode. Because of the nature of the accelerator source, the FEL produces a continuous stream or bursts of individual pulses, ranging in duration from 0.5 to 5 ps, at pulse repetition rates ranging from 4.5 to 75 MHz. Since operating continuously at these repetition rates would eventually lead to unacceptable thermal loading and damage to the ablation targets, a macropulse structure was used to deliver bursts of pulses from the FEL. Typical bursts (macropulses) ranged from 50 to 250 μs. Fig. 38(b) shows the pulse structure of the FEL beam used in our experiments.

The second laser used was a Spectra Physics, High Intensity Peak Power Oscillator (HIPPO), nanosecond high power Q-switched laser system at Jefferson Lab. Table V shows the specification of the laser system used for our experiment.

TABLE V. Laser parameters used.

	Jefferson lab-FEL	HIPPO
Wavelength used	3.43 μm	1.064 μm
Energy / pulse	~ 14 – 15 μJ (Macropulse)	0.13 mJ
Repetition rate	60 Hz (Macropulse) 4 MHz (Micropulse)	15 kHz
Pulse duration	50 μs (Macropulse width)	15 ns
Fluence	$\cong 14.6$ J/cm2	$\cong 2.5$ J/cm^2
Beam spot(diameter)	$\cong 400$ μm	$\cong 80$ μm

Fig. 38. (a) Schematic layout of the free-electron laser at the Thomas Jefferson National Accelerator Laboratory, showing the photocathode electron source and injector, the superconducting RF linac, the recirculation and energy-recovery arc, and the optical cavity and wiggler that generates the tunable infrared laser radiation. (b) Pulse structure of the FEL beam.

III. EXPERIMENTAL DETAILS

Cyclic olefin copolymer - Topas 8007 was previously identified as a potential commercial barrier material for OLEDs; its chemical structure is shown in Fig. 39. Samples of COC discs were typically prepared by placing approximately 10 g of extruded pellets into a 50.8 mm inside diameter polished stainless steel mold and heating on a laboratory hot plate under atmospheric conditions. As the sample softened, the pellets were pressed into the mold using a second stainless steel plate in order to expel trapped air between the pellets and form a smooth surface for ablation. The steel mold was removed from the hot plate and placed on a cold metallic surface to induce rapid solidification and permit the removal of the targets without deforming and scratching them. The cooled target was then removed from the mold, inverted, and mounted in the PLD chamber. These were used as target for thin film deposition and also craters of single pulse shot were created to measure the cratering threshold energy.
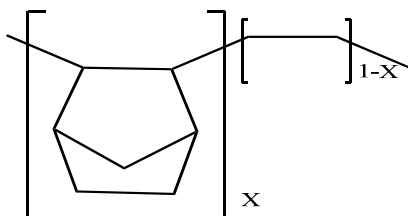
FIG. 39. Chemical structure of the cyclic olefin copolymer.

A PVD Products Inc. PLD 5000 system was used to carry out the experiments. Pulsed laser deposition is carried out in a vacuum chamber evacuated by a rotary backed turbo pump to 10^{-6} Torr. The laser beam is incident at an angle of 60° from normal of the rotating target. A reflecting mirror placed in the optical train is used to raster the laser

beam over a radial range on the target up to ~ 4.5 cm. The target pedestals can hold the targets of 50 mm in diameter and 2-3 mm in thickness and can rotate individually with the maximum rotation speed of 12 rpm. The distance between the substrate (glass slide or 13 mm NaCl disc mounted on the glass slide) and the target was fixed to 10 cm.

The FEL and HIPPO lasers were focused onto the surface of the drop-cast ablation targets by long focal-length BaF_2 lenses. The FEL pulsed beam was focused on one area on the surface of the target and the target was rotated such that the beam creates a 3 cm diameter circular track at a rate of either 1 rpm or 5 rpm, exposing the FEL for one minute. Thus each spot irradiated by the laser in fact absorbs the laser light from thousands of ps micropulses. The off resonant HIPPO laser was programmed to raster on the whole target surface, while the target was rotating at a rate of 9 rpm for 10 minutes.

Knife edge measurements were used to determine the beam spot (diameter) for both FEL and HIPPO lasers (for details see Appendix A). The beam was measured both vertically and horizontally on the target. To find the ablation threshold of energy (fluence) per pulse on COC, the FEL beam was delivered to the target in a circular pattern with a low repetition rate of 1 Hz so that individual spots (craters) on the COC target could be measured.

IV. RESULTS AND DISCUSSION

Structural and surface topography analysis techniques were used to elucidate the characteristics of the COC barrier thin film deposited on the NaCl disc using both resonant and off resonant infrared pulsed laser beams. The COC thin films of thickness 400 nm to 800 nm were successfully deposited using the Jefferson Lab FEL beam at 3.43 μm laser wavelength.

A.   Surface topography of COC thin film

The surface topography of the deposited COC thin films were observed by scanning electron microscopy (SEM) and atomic force microscopy (AFM). The field emission scanning electron microscope (Hitachi S-4700 SEM/EDS) was operated at an acceleration voltage of 1.5 kV, with a scale of 100 μm indicated by the scale bars in Fig. 40.
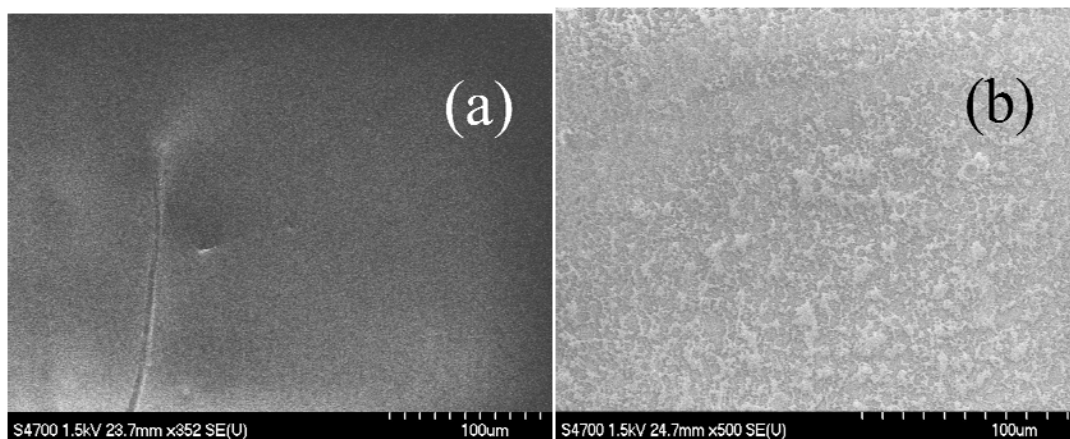
FIG. 40. Scanning electron micrographs of the samples deposited on NaCl plates using (a) Jefferson lab free-electron laser, (b) Nanosecond HIPPO laser.

Fig. 40(a), shows that the COC thin film deposited by the FEL was clear and uniform, compared to the films deposited through HIPPO laser (Fig. 40(b)), which had island formation due to thermal degradation. Thermal degradation of polymer chains is molecular deterioration as a result of overheating. At high temperatures the components of the long chain backbone of the polymer can begin to separate and react with one another to change the properties of the polymer. The initiation of thermal degradation

involves the loss of a hydrogen atom from the polymer chain as a result of heat energy input from off resonant laser irradiation.[122] This creates a highly reactive and unstable polymer free radical and a hydrogen atom with an unpaired electron. So the COC thin film deposited using off resonant laser with fluence $\cong 2.5$ J/cm^2 had broken bonds pieces of burnt COC materials in the form of islands.

AFM images were made using a Digital Instruments Nanoscope IV (Veeco Dimension 3100) in tapping mode using 10 nm diameter silicon tips. The samples were scanned with the scan size of 50 µm × 50 µm. The AFM data indicated a roughness (R_q) of ~10 nm (Fig. 41(a)) on the COC thin film produced with Jefferson lab-FEL and 68 nm (Fig. 41(b)) roughnesses were observed on the thin film produced with the off resonant laser (HIPPO).
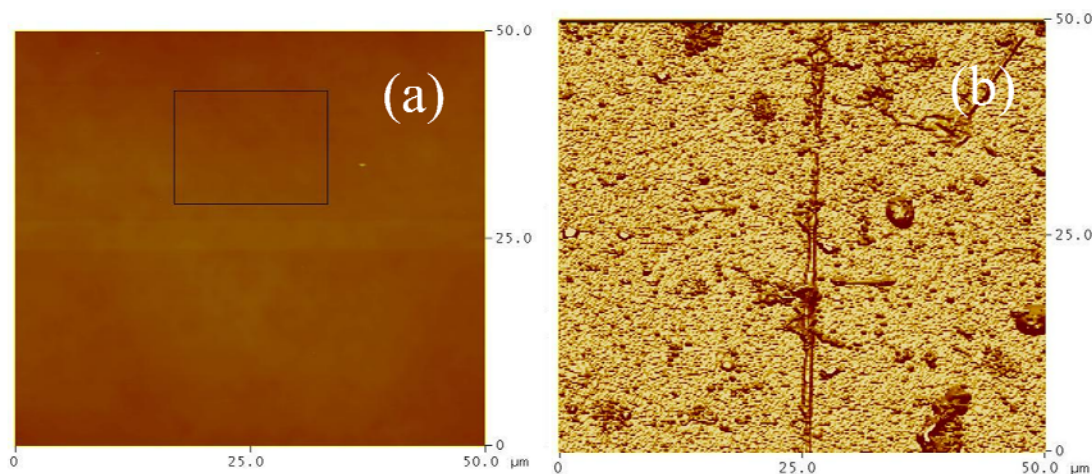
FIG. 41. Atomic Force Microscopy of the samples deposited on the NaCl plates using, (a) Jefferson lab free-electron laser, (b) HIPPO laser.

Fig. 42 shows the visible difference in damage to the COC target when using resonant vs. off resonant laser ablation. The COC target (Fig. 42(a)) was exposed with resonant

FEL laser at 3.43 microns, where the whole polymer chain was ablated without breaking the bonds and burning the target.[123] Fig. 42(b), shows the thermal degradation on the surface of the COC target after exposing it to an off resonant wavelength (1.064 microns), indicating the breaking of bonds due to thermal energy produced at this wavelength. These characterizations also show that RIR-PLD reduces polymer damage by tuning an infrared laser wavelength to a specific bond stretch or bond bend vibrational absorption peaks of the starting material, proving that wavelength is an important parameter for polymer thin film deposition.

Also another parameter to be noted is fluence. Though the fluence of the off resonant laser was very low compared to the resonant laser source, it has caused thermal damage on the surface. This shows that a laser source with resonant wavelength and minimum fluence is capable to ablate polymer chain to deposit polymer thin film. So finding the ablation threshold fluence becomes another important parameter.
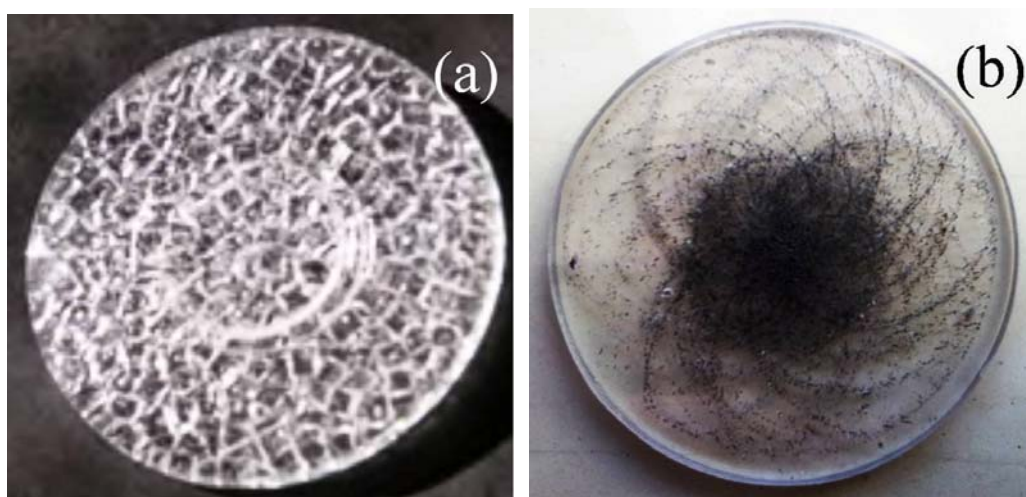
FIG. 42. Optical image of the target exposed with (a) FEL and (b) HIPPO lasers

B.   Stylus Profilometry of deposited COC films

To look at the long-range surface properties of the COC thin films, we used a stylus Profilometer (Dektak) to scan over the films deposited on the glass substrate. The deposited COC thin film using the FEL was very clear and transparent. The surface of the thin film was carefully scratched with a razor blade such that it does not it does not damage the substrate. This scratch on the thin film was used to measure the thickness of the thin film.

Fig. 43(a) shows the result of the film scanned over the scratch in the surface of the COC film, indicating the thickness of the deposited film, as well as surface scans over comparable stretches of the COC films deposited (fluence of ~14.6 J/cm^2). Fig. 45(b) shows the results of an edge scan for the COC thin film deposited using off resonant HIPPO laser. The average step height measured on the film to the substrate was ~750 nm and ~100 μm deposited with the Jefferson lab FEL and the HIPPO laser respectively. The scanning data obtained in between 500 microns to 2000 microns position from Fig. 43(a) also indicates that the thin film deposited using FEL beams at 3.43 microns had a uniform deposition of COC thin films compared with off resonant laser at 1.064 microns (position 0 microns to 350 microns).
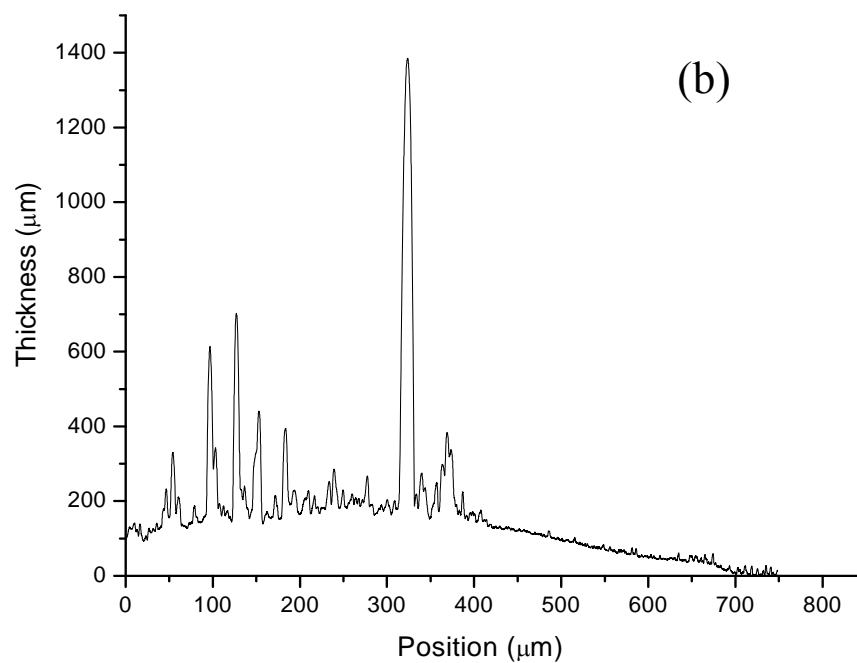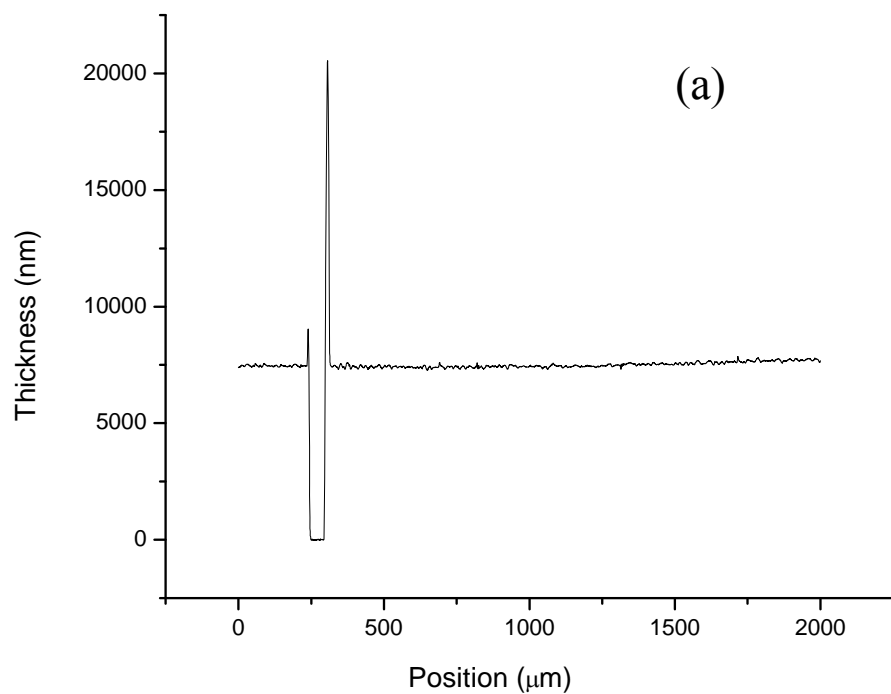
FIG. 43. Stylus Profilometer of COC thin films deposited using

(a) RIR ablation and (b) far IR ablation laser.

C.   FT-IR spectra of COC

Fourier-transform infrared (FTIR) spectrometry is a useful indicator of the extent to which the anharmonic monomer mode structure of the polymers is intact following laser ablation. Thus a comparison of the FTIR spectra of bulk sample materials with FTIR spectra of the deposited films is one indication of whether or not the polymers have survived more or less undamaged the processes of laser ablation and deposition in the form of thin films.

To facilitate FTIR measurements, films were deposited onto IR transparent NaCl plates of 13 mm in diameter and 2 mm in thickness for subsequent analysis. Fig. 44(a), shows a comparison of the FTIR spectra of FEL and HIPPO laser deposited COC thin films and a bulk COC disc. The bulk COC measurements of absorption were performed in reflection configuration and the thin film was analyzed in transmission configuration, accounting for the different normalization in the curves. The measured spectrum of FEL deposited COC thin film shows the gross features of bulk COC.
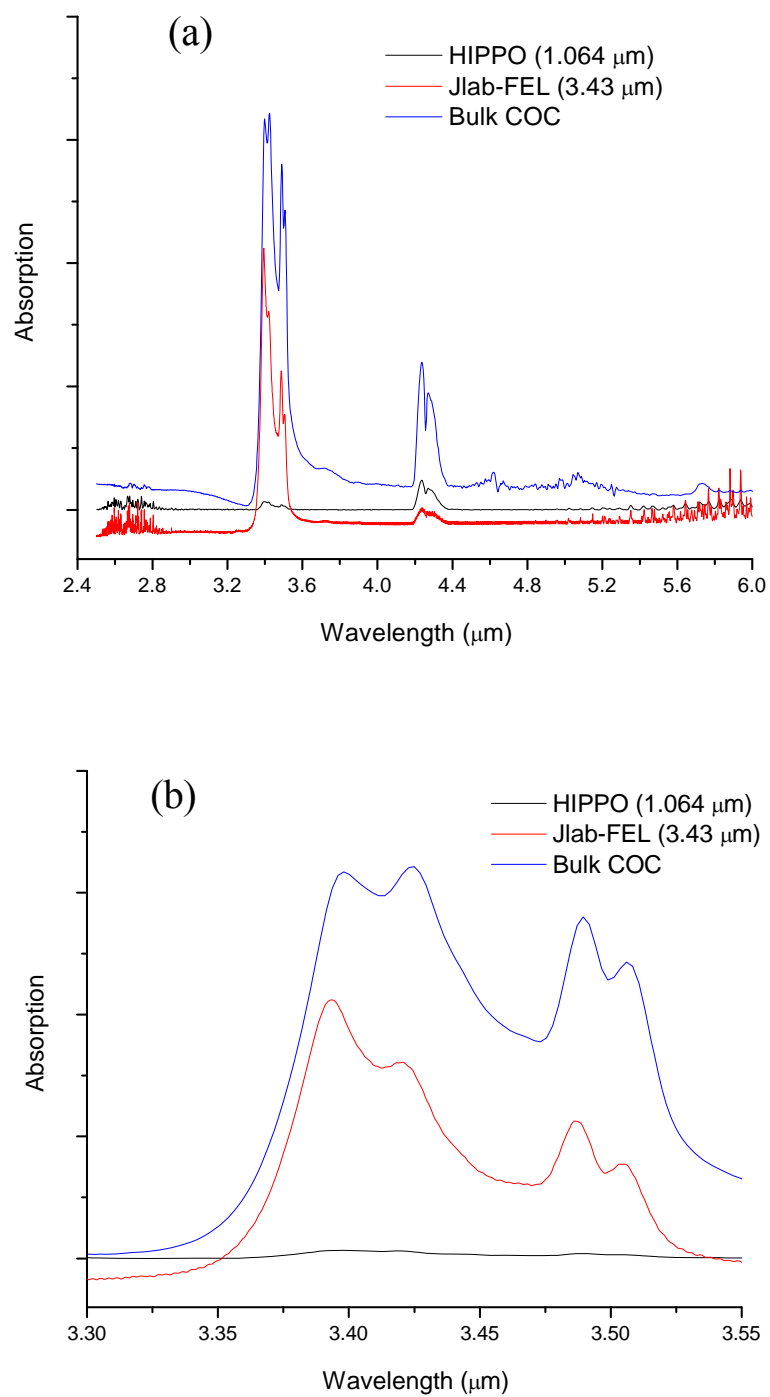
FIG. 44. Measured FTIR spectra (a) Comparing laser deposited thin films and bulk COC target, and (b) Expansion of FTIR spectra. (c) Measured FEL spectrum during experiment showing tuned peak at 3.41 μm and FWHM width of 75 nm.

FIG. 44. Continued
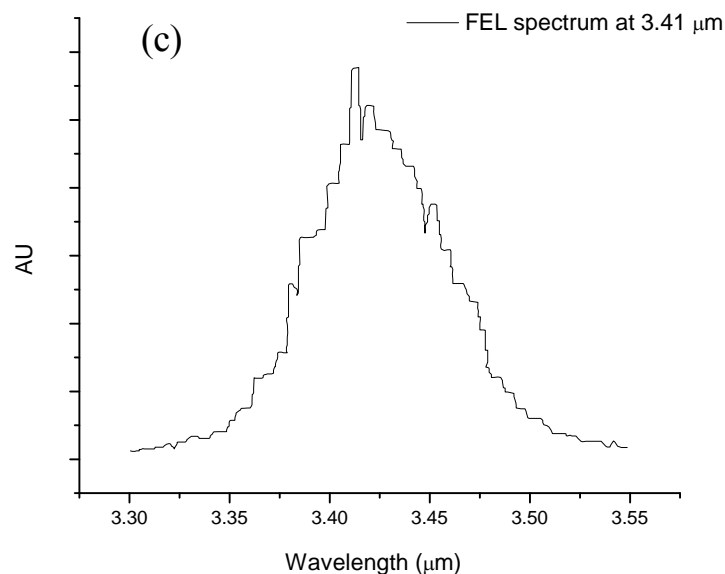
The principal feature of the absorption spectrum of COC is the aliphatic C-H stretch around 3.43 μm. This feature is prominent in the measured absorption spectra of the bulk COC and the COC thin film deposited using RIR-FEL shown in Fig. 44(a) and in more detail in Fig. 44(b). Because this feature is retained in the thin film, it is concluded that the film consists of COC; the FEL photons did not degrade the polymer material. On the other hand, due to the absence of the C-H stretch resonance in the absorption spectrum of the thin film produced using the HIPPO laser, shows that the material deposited using the off resonant HIPPO laser has been modified and the stretch bond broken. As seen in Fig. 44(c), the FEL was tuned to directly excite the C-H stretch bond and the incident radiation is entirely within the bandwidth of the measured resonance, producing effective absorption and heating of the bulk COC in the target.

The FEL photon pulse width was not measured during the experiment, but Happek scans were performed to analyze the electron bunch length which was around 200 fs. Direct autocorrelation measurements of the FEL photon pulse width could be useful to understand more clearly what happens on the polymer, when FEL beam at a specific wavelength and pulse width is irradiated.

D.   Erosion of the COC surface due to RIR irradiation followed by crater depth analysis.

From Fig. 40 to Fig. 44, it was clear that deposition of COC thin films using 3.43 microns IR-FEL at a fluence of ~14.6 J/cm^2 was successful. The next important parameter to be determined was the ablation fluence threshold at the same wavelength. These individual craters were generated on the clear 50 mm COC target with RIR-FEL pulse beam with repetition rate of 1 Hz and rotating the COC target, such that the craters are produced in the circular formation and two exposed areas do not overlap each other.

The depth of the exposed area/crater was measured using 3D optical microscopy ("HIROX" KH-3000VD high resolution digital-video microscopy system). The difference between the bottom of the crater and the top surface was scanned layer by layer (z stack). Fig. 45 shows the evolution of the surface of the COC due to the thermal energy produced at different fluences. At fluences below ~ 5.5 J/cm^2 (Fig. 45(a) – 45(b)), only surface melting is observed. Above ~5.5 J/cm^2 (Fig. 45(c) – 45(f)), the fluences were sufficient for crater formation. A fluence of ~5.5 J/cm^2 is the ablation threshold fluence of the pulsed FEL beam at 3.43 microns. Though the craters were formed with depth of ~ 7 microns, the energy was not quite enough to push the material upwards to reach the substrate which was kept ~10 cm above the target. Further above ~10 J/cm^2

material was ablated from the surface of the COC. Around 14 J/cm^2 the ablated COC material was energetic enough to reach the surface of the substrate creating the COC thin films (Fig. 40(a) and 41(a)).
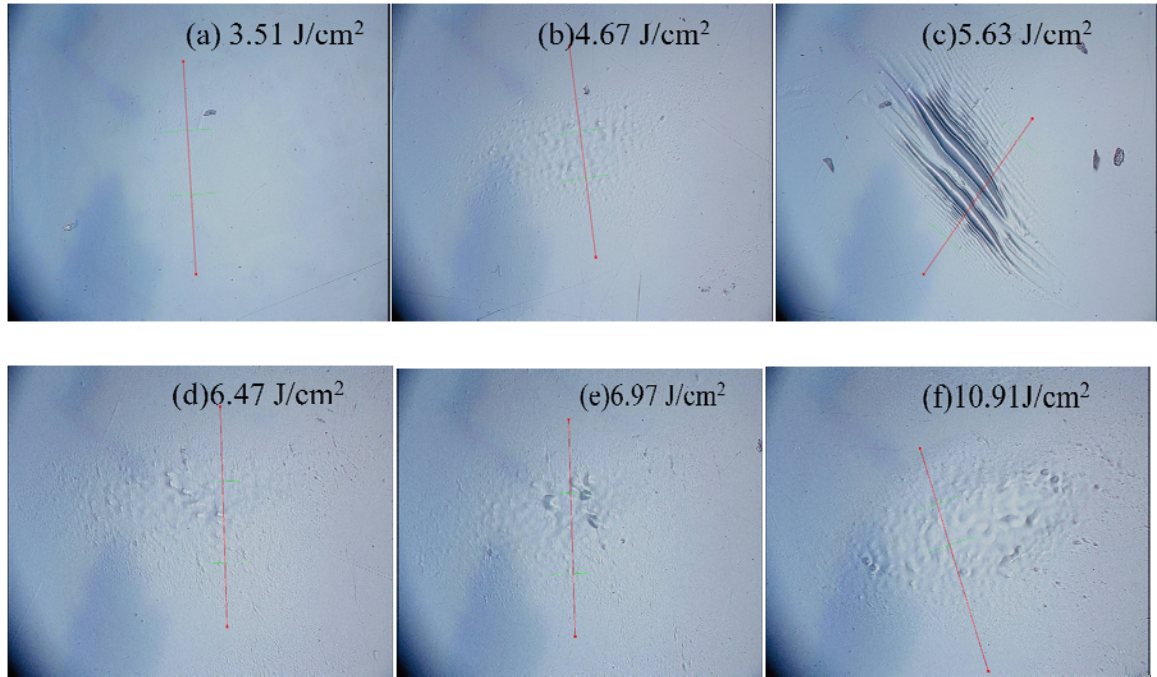
FIG. 45. Surface changes on COC target due to various fluences produced by the single FEL pulse.

The red line in each Fig. 45(a) – 45(f), represents the line scan done to obtain 1-D surface topography analysis. Fig. 46 shows the line scan of the respective image obtained from Fig. 45, giving another clear picture of how the surface melts/degrades and craters are formed after reaching the ablation fluence threshold. Fig. 47 shows the pseudo-etch depth measurements obtained from the series shown in Fig. 45 vs. the fluence used to produce these changes.

FIG. 46. Line scan obtained from Fig. 45.
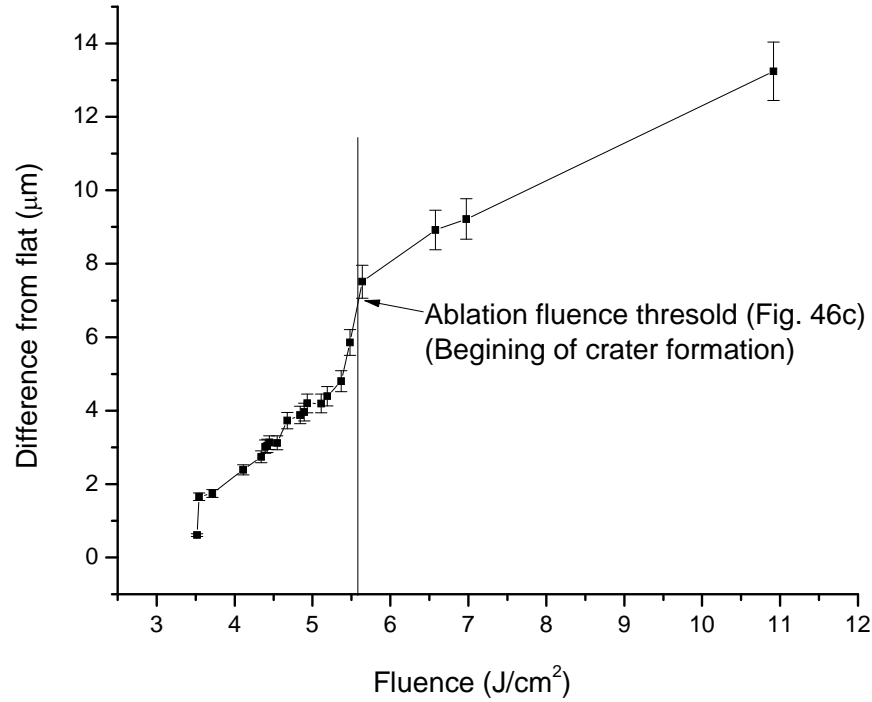
FIG. 47. Single FEL pulse fluence vs deformation from flat surface.

V. Thermal calculations (MATLAB)

As a special case of phase transformation, spinodal decomposition can be illustrated on a phase diagram exhibiting a miscibility gap. Thus, phase separation occurs whenever a material transitions into the unstable region of the phase diagram. The boundary of the unstable region sometimes is referred as binodal or coexistence curve which is found by performing a common tangent construction of the free-energy diagram. The region inside this binodal is called the spinodal, which is found by determining where the curvature of the free-energy curve is negative. The binodal and spinodal meet at the critical point. In this critical point a material is moved into the spinodal region of the phase diagram. This type of phase transformation is known as spinodal decomposition of phase explosion. To

determine whether this spinodal decomposition is followed by recoil-induce ejection of material which could be responsible for ablation, a finite element calculation was performed of the surface temperature rise of the COC target due to RIR laser irradiation, following the method used by S. Johnson, et.al. [124,125] in analysis of RIR-PLD of polystyrene targets.

The time dependent heat diffusion equation is solved to find the temperature rise of the copolymer. Since laser spot size in both x and y directions are much larger than the optical penetration depth, it is sufficient to solve the equation in z direction alone. The rate of heat conduction through a medium in a specified direction (here z-direction) is expressed by Fourier's law of heat conduction for 1-D heat conduction, which is given by Eq. (10)

$$\frac{\partial T}{\partial z} = \frac{Q}{\rho c_p},$$

(10)

where the heating source ($Q = I/\alpha$) is the energy density deposited by the laser, ρ is the density, c_ρ is the specific heat and I is the fluence per unit time. Since the criterion of thermal confinement holds in the z-direction, it is automatically satisfied in x and y as well, since the laser spot size is larger than the penetration depth. Thus the analytical expression for the temperature after laser absorption is given by Eq. (11)

$$T = T_i + \frac{2\alpha\varphi}{\rho c_p} exp\left(\frac{-2(x^2+y^2)}{\omega^2} - \alpha z\right),$$

(11)

where ω is the $1/e^2$ radius of the beam and α is the absorption coefficient. Here the coordinate system origin is at the center of the laser beam on the surface of the target and moving into the target corresponds to increasing z. The thermal properties of COC are given in Table VI.

TABLE VI. Thermal properties of COC and laser parameters used.

Thermal properties of COC	
Absorption coefficient at room temperature	732 cm^{-1}
Melting temperature	260 ^{0}C
Specific heat	0.39 J/g/^{0}C
Density	1.02 g/cm^3
Thermal conductivity	0.0014 W/cm/^{0}C

Laser Parameters	
Pulse time	50 µs
Beam diameter	400 µm
Wavelength	3.43 µm
Fluence	2 – 5.5 J/cm^2

Fig. 48 shows the cross-sectional image of the laser induced temperature rise for the wavelength of 3.43 microns and the fluence of 5.5 J/cm^2. Enthalpy of fusion is not taken into account, since the copolymer has no enthalpy associated with melting.[126] Since classical boiling is not a valid physical concept in polymers, the concept of spontaneous boiling up of polymer melts can only be explained through a spinodal decomposition process. The calculation shown in Fig. 48 demonstrates that the surface of COC reaches 1000 ^{0}C down to a depth of ~ 10 µm, indicating that spinodal decomposition is possible

at and immediately below the surface of the target alone. Since enthalpies associated with any phase transitions are not taken into consideration, the temperature calculated in this case is overestimated.
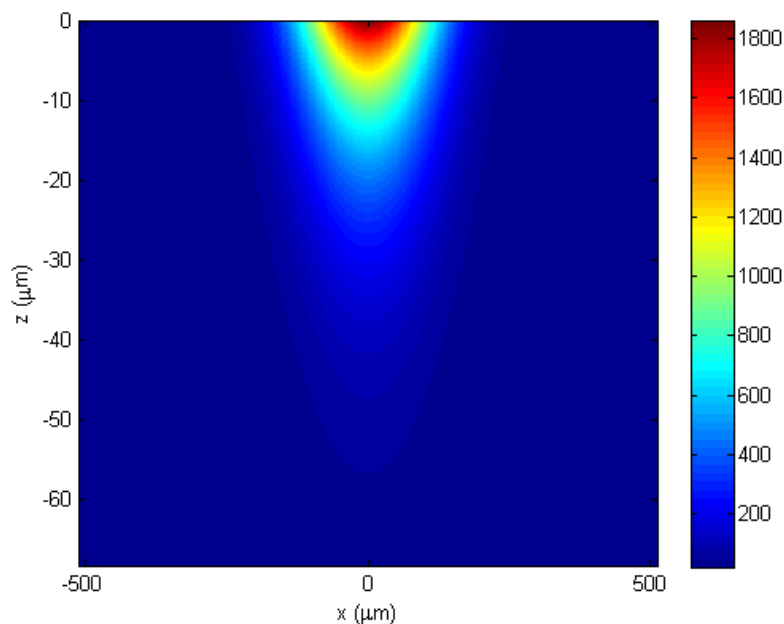
FIG. 48. Calculated laser induced temperature rise as a function of

x and z in COC using parameters as stated in Table VI.

Eq. (10) assumes that all variables are temperature independent, which is not in fact the case. Thus a temperature dependent 1-D heat equation must be solved to obtain the surface temperature rise of the material. A detailed description of this simulation calculation is shown earlier.[124]

The temperature dependent specific heat capacity of COC was measured using 2920 MDSC V2.6A differential scanning calorimetry (DSC). The temperature dependent absorption @ 3.43 μm was measured using Perkin Elmer RX FTIR spectrometer with 4 cm^{-1} resolution. These data are shown in Fig. 49. The absorption data were taken by

Dr. D.M. Bubb at Rutgers University and specific heat data were taken by Dr. D. Kranbuehl at College of William & Mary. The thermal properties of COC are given in Table VI and the fluence values from Fig. 47 were used for the simulation.
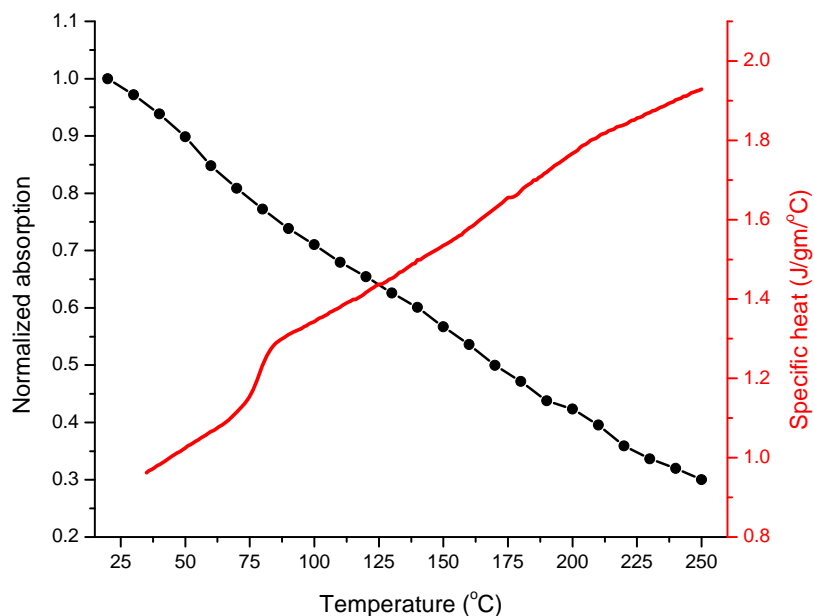
FIG. 49. Specific heat and IR absorbance at 3.43 μm

as a function of temperature of COC.

Fig. 50 shows the calculated temperature rise of the COC target at various fluences. As the temperature dependent absorption and specific heat data extend only up to 250^0C, the simulated surface temperature was calculated out only up to that temperature; the data above 250^0C was extrapolated. At fluences below 3.5 J/cm^2, the surface temperature does not reach the melting point of COC which was confirmed by our experimental results. At fluences greater than 3.5 J/cm^2, the surface temperature exceeds the melting point of COC, thus hoping to produce craters and ablating the material from the surface. According to the simulation, at 3.5 J/cm^2, the maximum surface temperature rise was just

above the melting temperature. From Fig. 45a, it is also evident that the surface of the COC target just started to melt and the laser creates a deformation on the surface. As the fluence was gradually increased to 5.5 J/cm^2, the surface temperature rose until ~350 ^{o}C which is enough to produce a crater of smaller depth (Fig. 45c and 46c) on the COC target following ablating the polymer chain from the surface of COC. Thus any fluence above 6 J/cm^2 would be enough to develop a thin film provided the target-substrate throw distance should be enough such that the ablated polymer chain reaches the surface of the substrate. Further exploration of fluence above 6 J/cm^2 and target-substrate throw distance would provide more information about the quality of the COC thin film deposited.

Fig. 51 shows the maximum surface temperature on the COC target at different fluences per pulse. The surface temperature simulation results were consistent with the experimental results of COC thin film deposition followed by crater measurements.
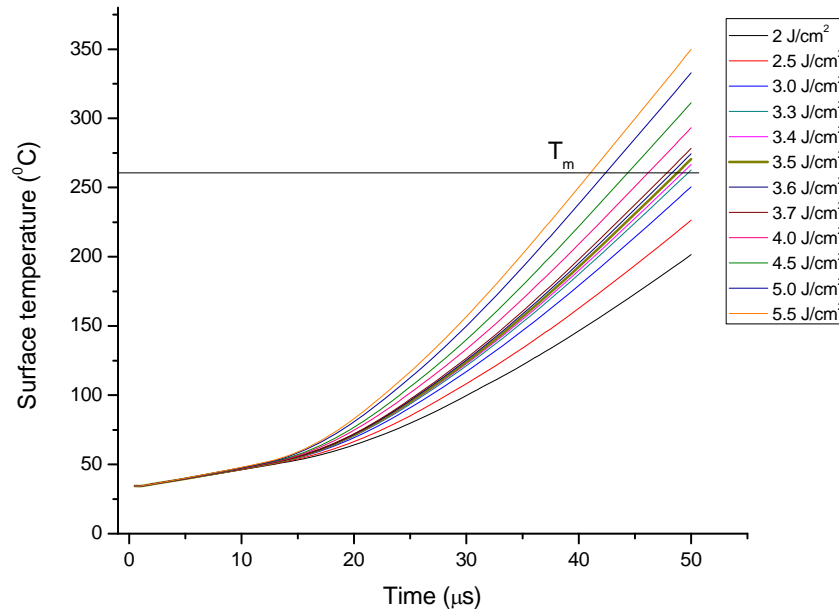
FIG. 50. Surface temperature rise of the COC target at different fluence per pulse.
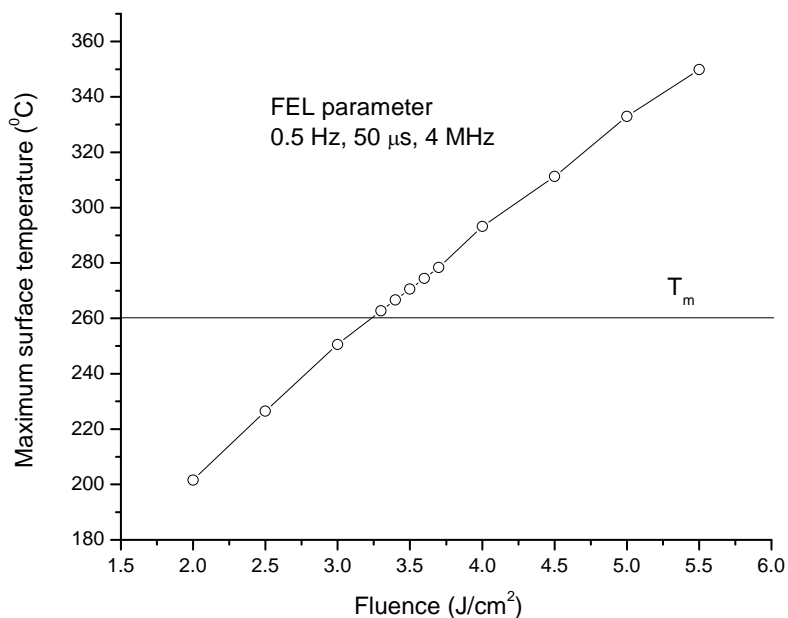
FIG. 51. Maximum surface temperature vs fluence

VI. CONCLUSION

At this point, there are so few mechanistic studies, and so few possible laser sources, that it is necessary to address these two issues before it is possible to begin commercial-scale development of the RIR-PLD process. Recent progress in vapor-phase deposition of the barrier polymer COC by RIR-PLD using picosecond lasers adds one more essential ingredient to previous studies showing vapor-phase deposition of polymer light-emitting diodes. While testing of the permeability of the films still needs to be done, the smoothness of the films and their high transparency is encouraging. The study presented here is a next step in demonstrating successful deposition of such materials using infrared laser technology. The fluence threshold measurements and the fluence used for thin film deposition were consistent with the simulation results. Thermal degradation on the COC

surface using an off resonant wavelength laser was observed, which proves wavelength is an important parameter polymer thin film deposition. Continued development of appropriate picosecond sources for the mid-infrared remains a high priority in order to develop this branch of thin-film synthesis for the future of organic and polymer-based optoelectronic devices.

CHAPTER 6

CONCLUSIONS

This dissertation represents a collection of work that was undertaken to investigate the laser material processing of metals and polymers using two different types of lasers. Successful laser material processing relies significantly on the development of new process schemes. Several novel techniques were used to process metals and polymers based on pulsed laser deposition (PLD) techniques, and the resulting material was thoroughly analyzed by a variety of methods.

For example, niobium surface melting in vacuum was used to smooth rough surfaces. Improvements in surface roughness were observed, quantified and optimized. Smoother material may have applications in SRF cavities where such processing could not only increase the cavity gradient, but also this method may be useful to repair interior surface damage of the cavities used in accelerators.

Next the niobium was processed in the nitrogen atmosphere. Evidence of successful nitriding of niobium to produce a superconducting phase niobium nitride (δNbN) surface layer was achieved. This result is a significant advance over traditional furnace nitriding, where it has not been possible to obtain only the delta phase NbN, but which was achieved using pulsed laser deposition. Surface temperature simulations were consistent with measurements for both niobium surface melting and niobium surface nitriding.

Another technique was used to understand the phenomenon of depositing delta phase NbN thin film both on copper and on niobium. Direct ablation of niobium in nitrogen atmosphere shows that the pulsed laser deposition method can be used to deposit δNbN

on a niobium substrate, but additional work is needed to deposit δNbN on a copper substrate. A pure δ phase NbN thin film was not obtained, but a procedure to obtain δNbN using pulsed laser deposition was found.

Finally, a free electron laser was used to deposit polymer (cyclic olefin copolymer) thin film using the resonant infrared free electron laser ($\lambda = 3.43$ μm) at Jefferson Lab. Fluence threshold measurements and the fluence used to deposit COC thin film was consistent with simulation results. Observations of thermal degradation of the polymer using off resonant wavelength laser was observed.

REFERENCES

[1]*Intelligent Energy Field Manufacturing Interdisciplinary Process Innovations*, edited by W. Zhang, (CRC Press, Florida, 2011).

[2]P. Schaaf, *Laser processing of materials; fundamentals, application and developments*, (Springer-Verlag Berlin Heidelberg, 2010).

[3]A. Vogel, J. Noack, G. Huttermann, and G. Paltauf, J. Phys. Conf. Ser. **59**, 249 (2007).

[4]A. Vogel, J. Noack, G. Huttman, G. Paltauf, Appl. Phys. B **81**, 1015 (2005).

[5]S.Y. Chou, and Q. F. Xia, Nat. Nanotechnol. **3(5)**, 295 (2008).

[6]W. Hoving, Proc. SPIE **3097**, 248 (1997).

[7]E. Louzon, Z. Henis, S. Pecker, Y. Ehrlich, D. Fisher, and M. Fraenkel, App. Phys. Lett. **87**, 41903 (2005).

[8]R.J. Levis, G.M. Menkir, and H. Rabitz, Science **292**, 709 (2001).

[9]F.E. Livingston, L.F. Steffeney, and H. Helvajian, Appl. Surf. Sci. **253**, 8015 (2007).

[10]S.M. Pimenov, G.A. Shafeev, A.A. Smolin, V.I. Konov, and B.K. Vodolaga, Appl. Surf. Sci. **86(4)**, 208 (1995).

[11]C. Ristoscu, G. Socol, C. Ghica, I.N. Mihailescu, D. Gray, A. Klini, A. Manousaki, D. Anglos, and C. Fotakis, Appl. Surf. Sci. **252(13),** 4857 (2006).

[12]J. Solis, C.N. Afonso, J.F. Trull, and M.C. Morilla, J. Appl. Phys. **75(12)**, 7788 (1994).

[13]B. Tan, K. Venkatakrishnan, and K.G. Tok, Appl. Surf. Sci. **207(4)**, 365 (2003).

[14]V.P. Veiko, G.K. Kostyuk, N.V. Nikonorov, A.N. Rachinskaya, E.B. Yakovlev, and D.V. Orlov, Proc. SPIE B. 66060Q (2007).

[15]F.E Livingston, P.M. Adams, and H. Helvajian, Appl. Phys. A **89**, 97 (2007).

[16]F.E. Livingston, and H. Helvajian, Appl. Phys. A **81**, 1569 (2005).

[17]F.E. Livingston, P. Adams, and H. Helvajian, Proc. SPIE **5662**, 44 (2004).

[18]F.E. Livingston, P. Adams, and H. Helvajian, Appl. Surf. Sci. **247**, 526 (2005).

[19]D.M. Bubb, J.S. Horwitz, J.H. Callahan, R.A. McGill, E.J. Houser, D.B. Chrisey, M.R. Papantonakis, R.F. Haglund Jr, M.C. Galicia and A. Vertes, J. Vac. Sci. Technol. A **19(5)**, 2698 (2001).

[20]D.M. Bubb, B. Toftmann, R.F. HaglundJr, J.S. Horwitz, M.R. Papantonakis, R.A. McGill, P.W. Wu and D.B. Chrisey, Appl. Phys. A **74**, 123 (2002).

[21]J. Mazumder and A. Kar, J. Metals. **9**, 18 (1987).

[22]G. Sepold, and M. Grupp, Contents of the proceeding (LANE 2001), pp. 133.

[23]G. Horowitz, J. Mate. Res. **19**, 1942 (2004).

[24]M. Katayama, Y.Tokuda, Y. Inoue, A. Usami and T. Wada, J. Appl. Phys. **69**, 3541 (1991).

[25]*Laser–Tissue Interaction IX,* edited by S. L. Jacques, (SPIE Proc. Series Vol. 3254 Bellingham, WA, 1998).

[26]S.L. Jacques, Appl. Opt. **32**, 2447 (1993).

[27]L.V. Zhigilei and B.J. Garrison, Appl. Phys. Lett. **74**, 1341 (1999).

[28]A. Miotello and R. Kelly, Appl. Phys. A **69A,** S67 (1999).

[29]R. Kelly and A. Miotello, Phys. Rev. E **60**, 2616 (1999).

[30]M.M. Martynyuk, Sov. Phys. Tech. Phys. **21**, 430 (1976).

[31]L.V. Zhigilei, P.B.S. Kodali, and B. J. Garrison, Chem. Phys. Lett. **276**, 269 (1997).

[32]D. Bauerle, *Laser Processing and Chemistry, (Springer Series in material science,* Berlin, Heidelberg: Springer-Verlag 1996).

[33]R. Poprawe, *Tailored Light 2: Laser Application Technology*, 1st ed., (Springer-Verlag, Berlin, Heidelberg, 2011).

[34]D.B. Chrisey and G.K. Huber, *Pulsed laser deposition of thin films*, (John Wiley & Sons, NewYork, 1994).

[35]R. Eason, *Pulsed laser deposition of thin films*, (John Wiley & Sons, New York 2006).

[36]W. M. Steen, *Laser Material Processing* (Springer-Verlag London Limited, 1991).

[37]N.B. Dahotre and S.P. Harimkar, *Laser Fabrication and Machining of Materials* (Springer, New York, 2008).

[38]J.D. Jackson, *Classical Electrodynamics*, (John Wiley & Sons, New York, 1999).

[39]M. Born and E. Wolf, *Principles of Optics* (Cambridge University Press, London, 1999).

[40]Luxpop is the database for Thin film and bulk index of refraction and photonics calculations. www.luxpop.com

[41]N. Perrin, and C. Vanneste, J. Phys. France. **48**, 1311 (1987).

[42]P.P. Pronko, S.K. Dutta and D. Du, J. Appl. Phys. **78**, 6233 (1995).

[43]P. Schaaf, Prog. Mater. Sci. **47**, 1 (2002).

[44]S. Unamuno, M. Toulemonde, and P. Siffert, *Laser Processing and diagnostics*, edited by D. Bauerle (Springer-Verlag, Berlin, 1984).

[45]F. Righini, J. Spisiak, G.C. Bussolino and M. Gualano, International J. Ther. Phys. **20(4)**, 1107 (1999).

[46]G. Betz and M.G. Frohberg, Scripta Metallurgica. **15**, 269 (1981).

[47]J.P. Moore, R.S. Graves and R.K. Williams, High Temp. High Pressures. **12**, 579 (1980).

[48]R. Hultgren, *et.al.*, *Selected values of the thermodynamic properties of the elements*, (American Society for Metals, Metals Park, OH, 1973).

[49]H. Padamesee, J. Knobloch and T. Hays, *RF superconductivity for Accelerators,* 2nd ed.*, (John Wiley & Sons, Inc., New York, 2008).

[50]J.A. Ramos, D.L. Bourell, and J.J. Beaman, *Mat. Res. Soc. Symp. Proc.* 758, (Massachusetts, USA, 2002), pp. 53-61.

[51]W.M. Steen, and K.G. Watkins, J. Phys. IV. **3**, 581 (1993).

[52]T.L. Perry, D. Werschmoeller, N.A. Duffie, X. Li, and F.E. Pfefferkorn, J. Manuf. Sci. E-T ASME. **131,** 031002 (2009).

[53]M. Vadali, C. Ma, N.A Duffie, S. Li and F.E. Pfefferkorn, *Proc. International Conference on MicroManufacturing*, (ICOMM, Tokyo, Japan, 2011), pp. 331-338.

[54]T.L. Perry, D. Werschmoeller, N.A. Duffie, X. Li, and F.E. Pfefferkorn, J. Manu. Sci. E-T ASME **131,** 021002 (2009).

[55]T.L. Perry, D. Werschmoeller, X. Li, F.E. Pfefferkorn, and N.A. Duffie, J. Manuf. Proc. **11,** 74 (2009).

[56]P.F. Marella, D.B. Tuckerman, and R.F. Pease, Appl. Phys. Lett. **54**, 1109 (1989).

[57]D.B. Tuckerman, and A. H. Weisberg, IEEE Electr. Device. Lett. **7**, 1 (1986).

[58]T.M. Shao, M. Hua, H.Y. Tam and E.H.M. Cheung, Surf. Coat. Tech. **197**, (2005).

[59]M. Bereznai, I. Pelsoczi, Z. Toth, K. Turzo, M. Radnai, Z. Bor, and A. Fazekas, Biomaterials. **24**, 4197 (2003).

[60]A. Temmler, K. Graichen, and J. Donath, J. Laser Technik. **7**, 53 (2010).

[61]Y. G. Kim, J.K. Rye, D.J. Kim, H,J. Kim, S. Lee, B.H. Cha, H. Cha, and C.J. Kim, Jpn. J. Appl. Phys. **43**, 1315 (2004).

[62]S. Aldajah, O.O. Ajayi, G.R. Fenske, and S. Kumar, J. Tribol-T. ASME **125**, 643 (2003).

[63]H. Tian, C. Xu, C.E. Reece, and M.J. Kelley, Appl. Surf. Sci. **257**, 4781 (2011).

[64]F. Spaepen, *Ultrafast Phenomena V: Proceedings of the Fifth OSA Meeting* (New York: Springer-Verlag, 1986), pp. 174-178.

[65]M. Senthilkumar, N.K. Sahoo, S. Thakur, and R.B. Tokas, Appl. Surf. Sci. **252,** 1608 (2005).

[66]G. Gavrila, A. Dinescu, and D. Mardare, Roma. J. Info. Sci. Tech. **10**, 291 (2007).

[67]B. Aune *et.al.*, Phys. Rev. S T Accel. Beams **3**, 092001 (2000).

[68]M. Pham Tu, K. Mbaye, L. Wartski, and J. Halbritter, J. Appl. Phys. **63**, 4586 (1988).

[69]Z. Wang, A. Kawakami, Y. Uzawa, and B. Komiyawa, J. Appl. Phys. **79**, 7837 (1996).

[70]J.C. Villegier *et.al.*, Physica. C **326-327**, 133 (1999).

[71]K. Mbaye, M. Pham Tu, N.T. Viet, L.Wartski and J.C. Villegier: Rev. Phys. Appl. **20**, 457 (1985).

[72]R.P. Elliott, *Constitution of Binary Alloys First Supplement*, (McGraw-Hill, New York, 1965).

[73]P. Fabbricatore, P. Fernandes, G.C. Gualco, F. Merlo, R. Musenich, and R. Parodi, J. Appl. Phys. **66(12)**, 5944 (1989).

[74]W. Lengauer, and P. Ettmayer, Monatsh. Chem. **117**, 275 (1986).

[75]C. Angelkort *et.al*., Spectrachim. Acta. A **57**, 2077 (2001).

[76]E. Carpene, P. Schaaf, M. Han, K.P. Lieb, and M. Shinn, Appl. Surf. Sci. **186**, 195 (2002).

[77]Y.E.E-D Gamal, M. S.E-D Shafik and J. M. Daoud, J. Phys. D: Appl. Phys. **32,** 423 (1999).

[78]H.U. Krebs, Int. J. of Non-Equilib. Pr. **10(3)**, 24 (1997).

[79]Bettis Jr. Appl. Opt. **31**, 3448 (1992).

[80]*Laser-induced plasma and applications,* edited by L.J. Radziemski, D.A. Cremers (New York, Marcel Dekker, Inc. 1992).

[81]P. Fabbricatore, P. Fernandes, G.C. Gualco, F. Merlo, R. Musenich, and R. Parodi, J. Appl. Phys. **66**, 5944 (1989).

[82]V.N. Zhitomirsky, I. Grimberg, L. Rapoport, N.A. Travitzky, R.L. Boxman, S. Goldsmith, A. Raihel, I. Lapsker, and B.Z. Weiss, Thin Solid Films **326**, 134 (1998).

[83]V.N. Zhitomirsky, I. Grimberg, L. Rapoport, N.A. Travitzky, R.L. Boxman, S. Goldsmith, and B.Z. Weiss, Surf. Coat. Technol. **120**, 219 (1999).

[84]A. Bendavid, P.J. Martin, T.J. Kinder, and E.W. Preston, Surf. Coat. Technol. **163**, 347 (2003).

[85]K.L. Rutherford, P.W. Hatto, C. Davies, and I.M. Hutchings, Surf. Coat. Technol. **86**, 472 (1996).

[86]M.S. Wong, W.D. Sproul, X. Chu, and S.A. Barnett, J. Vac. Sci. Technol. A **11(4),** 528 (1993).

[87]M. Fenker, M. Balzer, R.V. Büchi, H.A. Jehn, H. Kappl, and J.J. Lee, Surf. Coat. Technol. **163**, 169 (2003).

[88]K.S. Havey, J.S. Zabinski, and S.D. Walck, Thin Solid Films **303**, 238 (1997).

[89]M. Larsson, M. Bromark, P. Hedenqvist, and S. Hogmark, Surf. Coat. Technol. **91**, 43 (1997).

[90]Z. Han, X. Hu, J. Tian, G. Li, and G. Mingyuan, Surf. Coat. Technol. **179**, 188 (2004).

[91]M. Benkahoul, E. Martinez, A. Karimi, R. Sanjines, and F. Levy, Surf. Coat. Technol. **180**, 178 (2004).

[92]C.S. Sandu, M. Benkahoul, M. Parlinska-Wojtan, R. Sanjines, and F. Levy, Surf. Coat. Technol. **200**, 6544 (2006).

[93]N. Hayashi, I.H. Murzin, I. Sakamoto, and M. Ohkubo, Thin Solid Films. **259**, 146 (1995).

[94]M.L. Klingenberg, and J.D. Demaree, Surf. Coat. Technol. **146,** 243 (2001).

[95]K. Baba, R. Hatada, K. Udoh, and K. Yasuda, Nucl. Instrum. Methods Phys. Res. B Beam Interact. Mater. Atoms **127**, 841 (1997).

[96]X.T. Zeng, Surf. Coat. Technol. **11**, 75 (1999).

[97]G. Cappuccio, U. Gambardella, A. Morone, S. Orlando, and G.P. Parisi, Appl. Surf. Sci. **109**, 399 (1997).

[98]R.E. Teece, J.S.Horwitz, J.H. Classssen, and D.B.Chrisey, Appl. Phys. Lett. **65,** 22 (1994).

[99]A. Bhat, X. Meng, A. Wong and T.V. Duzer, Supercond. Sci. Tech. **10(3)**, 1032 (1999).

[100]K.S. Keskar, T. Yamashita, and Y. Onodera, Jpn. J. Appl. Phys. **10(3),** 370 (1971).

[101]H. Knau, A. Welti, A. Mielke, S. Senz and H.E. Stier, Physica C **182**, 1 (1991).

[102]S. Isagawa, Appl. Phys. **52**, 921 (1981).

[103]P. Fabbricatore, P. Frenandes, G.C. Gulaco, R. Masenich and R. Parodi, IEEE T. Magn. **25**, 1865 (1988).

[104]V.M. Pan, V.P. Gorishnyak, E.M. Rudenko, V.E. Shaternik, M.V. Belous, S.A. Koziychuk and F.I. Korzhinsky, Cryogenics **23**(5), 258 (1983).

[105]Kenji Kawaguchi and Mitsugushohma, Jpn. J. Appl. Phys. **30**, 2088 (1991).

[106]R.E. Teece, J.S. Horwitz, D.B. Chrisey, E.P. Donovan and S.B. Quadri, Chem. Mater. **6**, 2205 (1994).

[107]V. Boffa, V. Gambardella, V. Marotta, A. Morone, F. Murtas, S. Orlando, and G.P. Parisi, App. Surf. Sci. **106**, 361 (1996).

[108]K. Mittag, Cryogenics **13(2)**, 94 (1973).

[109]H. Knau, A. Welti, A. Mielke, S. Senz and H.E. Stier, Physica. C **182,** 39 (1991).

[110]A.J. Heeger, Rev. Mod. Phys. **73**, 681 (2001).

[111]A. P. Ghosh, L.J. Gerenser, C.M. Jarman, and J.E. Fornalik, Appl. Phys. Lett. **86(22),** 223503 (2005).

[112]F. Bundgaard, T. Nielsen, D. Nilsson, P. Shi, G. Perozziello, A. Kristensen, and O. Geschke, *Proceedings of the mTAS*, (Malmo, Sweden, 2004) pp. 372– 374.

[113]G. Khanarian, Opt. Eng. **40**, 1024 (2001).

[114]R. Scheller, ETP 99 World Congress, (1999).

[115]T. Scrivani, R. Benavente E. Perez, and J.M. Perena, Macromol. Chem. Phys. **202**, 2547 (2001).

[116]D.M. Bubb and R.F. Haglund, "*Resonant Infrared Pulsed Laser Ablation and Deposition of Thin Polymer Films, in Pulsed Laser Deposition of Thin Films:*

Applications-Led Growth of Functional Materials," edited by R. Eason (John Wiley and Sons, Inc., New York, 2006).

[117]D.M. Bubb, J.S. Horwitz, J.H. Callahan, R.A. McGill, E.J. Houser, D.B. Chrisey, M.R. Papantonakis, R.F. Haglund, M.C. Galicia, and A. Vertes, J. Vac. Sci. Tech. A **19(5),** 2698 (2001).

[118]M.R. Papantonakis and R.F. Haglund, Appl Phys A-Mater. **79(7),** 1687 (2004).

[119]N.L. Dygert, A. P. Gies, K.E. Schriver, and R.F. Haglund, Appl. Phys. A-Mater. **89(2)**, 481 (2007).

[120]M.R. Papantonakis, E. Herz, D.L. Simonsen, U.B. Wiesner, and R.F. Haglund, Jr., "*Deposition of functionalized nanoparticles in multilayer thin-film structures by resonant infrared laser radiation, in Laser-based Micro- and Nanopackaging and Assembly,*" edited by. W. Pfleging, Y. Lu, K. Washio, F. G. Bachmann and W. Hoving, (*Proceedings of SPIE*, 6459, 64590X, 2007).

[121]H. Injeyan and G. Goodno, *High Power Laser Handbook,* (McGraw-Hill Companies, Inc., China, 2010).

[122]C. Liu, J. Yu, X. Sun, J. Zhang and J. He, Poly. Degrad. Stab. **81**, 197 (2003).

[123]S.M. Avanesyan, A. Halabica, S.L. Johnson, M.J. Kelley, J.M. Klopf, H.K. Park, K.E. Schriver, S. Singaravelu and R.F. Haglund, Jr., Proc. SPIE **7585**, 758507 (2010).

[124]S.L. Johnson, "*Resonant-infrared laser ablation of polymers: Mechanisms and applications,*" Ph.D. thesis, (Vanderbilt University, 2008).

[125]S.L. Johnson, D.M. Bubb and R.F. Haglund Jr., Appl. Phys. A **96**, 627 (2009).

[126]D.V. Rosato, N.R. Schott, and M.G. Rosato, *Plastics Engineering, Manufacturing & Data Handbook*, (Springer, Berlin, 2001).

Appendix A

EXPERIMENTAL SETUP

I. PLD 5000

A. Pumping Stack

A PVD Products Inc., PLD 5000 system (Technical details courtesy of PVD Products Inc.) shown schematically in Fig. A1, was used for all the experiments performed at Jefferson Lab. Installing and commissioning it were key tasks. The system consists of a vacuum chamber made up of stainless steel, attached to a water cooled Pfeiffer vacuum turbo drag pump and splinter screen. The turbo pump provides a pumping speed of 1,200 l/sec. A Leybold D-25B rotary vane mechanical pump prepared for oxygen gas (Fomblin oil) is provided to evacuate the chamber and back the turbo pump. This package provided a base pressure below 5×10^{-7} Torr. When gas is passed through, the chamber can sustain the maximum positive pressure of 625 Torr.

A mechanical pump is used to evacuate the chamber and/or loadlock (optional) during the roughing cycle of pump down and also backs the turbo pump during operation. The foreline valve and the rough valve isolate the mechanical pump. The foreline valve connects the mechanical pump to the turbo pump, and once the foreline valve is open the turbo pump will evacuate. The rough valve connects the mechanical pump to the chamber, and once the rough valve is open the chamber will evacuate.

To spin up the turbo pump:

- Close the chamber gate valve (software interface)

- Switch on the mechanical pump (software interface)

- Open the foreline valve (software interface)

- Switch on the turbo pump (software interface)

- Wait for the turbo pump to reach full speed (625 rpm)

To spin down and turn off the turbo pump:

- Close the chamber gate valve (software interface)

- Switch off the turbo pump (software interface)

- Wait for the turbo pump to reach half of the maximum rotation speed

- Close the foreline valve (software interface)

- Switch off the mechanical pump (software interface, if not longer needed)

B. Loadlock

An optional loadlock with transfer arm is mounted to the system. The loadlock has a quick access door for sample loading. The sample is transferred into the main chamber with a magnetically coupled linear actuator. The loadlock includes a mechanical pump, roughing valve, foreline valve, vent valve, pressure relief valve, convectron gauge, and ion gauge.

C. Substrate Assembly

An optional substrate rotation assembly sits on top of a 2.75" Z-stage. The Z-stage movement is controlled by a stepper motor and has mechanical hard stops to limit the range of motion. The Z-stage can be lowered for substrate loading/unloading and raised for deposition. The rotary motion feedthrough is magnetically coupled and the entire assembly moves in unison with the motion of the Z-stage.

FIG. A1. Schematic diagram of PLD 5000

D. Adjustable height rotating substrate heater

A substrate heater consisting of a bank of 6 quartz halogen IR lamps housed in a water cooled OFHC copper block is provided. The copper block is polished and gold plated for good reflectivity. A maximum substrate temperature of 500 ^{o}C is achievable. The heater is powered via a programmable Eurotherm closed-loop temperature control unit and a DC power supply. A type K thermocouple is utilized as the input to the Eurotherm controller. The heater is mounted to an 8" conflate flange that provides all necessary feedthroughs. This flange is mounted to a programmable motorized Z-stage with 3" of stroke to provide variable target to substrate distances.

A rotating substrate stage is integrated with the heater unit. This includes a magnetically coupled rotary feedthrough with computer controlled motor with encoder to provide substrate rotation speeds up to 50 rpm. This unit is mounted to a motor driven Z-stage with 2" stroke to accommodate easy substrate transfers with the loadlock. A

stainless steel substrate spinner assembly and shaft connected to the rotary feedthrough is provided.

E. Liquid nitrogen cooled target manipulator

The target manipulator includes a large cylindrical electrode nickel plated OHFC copper liquid nitrogen reservoir that houses six stainless steel target pedestals. Three pedestals are for frozen liquid (MAPLE) targets, and three pedestals are used for solid targets. The MAPLE target pedestals are in excellent thermal contact with the reservoir via copper brushes. Each of the pedestals is held in place via a set of high quality ball bearings located within the reservoir housing. The shaft of each of the pedestals includes a spur gear. Upon indexing to the proper position, this spur meshes with a second spur gear driven by an appropriate motor drive with sufficient torque to rotate the one active target pedestal. Rotation speed up to 12 rpm is provided. All target indexing and target rotation functions are computer controlled.

The liquid nitrogen reservoir is bottom fed via a stainless steel tube and includes a similar vent line. A type K thermocouple is connected to the reservoir and a temperature readout display is provided. Infrared heat lamps sit beside the LN_2 reservoir and can be used to quickly heat the reservoir when the chamber is to be vented.

A molybdenum plate sits directly above the target assembly to minimize cross contamination between targets and to help thermally isolate the targets from the substrate heater. This plate includes a slot to expose the active ablation target to the incident laser beam and holes that line up under the fill tubes.

F. Intelligent Window

The intelligent window keeps the optical beam path clean and allows the laser beam energy to be monitored inside the deposition chamber. The unit includes an electropnuumatic linear-motion feedthrough with a reflector that diverts the laser beam to a Coherent PM 150 air cooled thermopile sensor with an EPM-1000 readout electronic unit.

A motorized drive is provided to rotate an internal sacrificial CaF disc 6" in diameter to expose new window surface to keep the beam path clean for extended periods. The laser beam entrance window to deposition chamber is a 2" CaF window sealed via a pair of differentially pumped Viton 0-rings.

G. Optical Train

A complete set of CaF optics is provided to cover the range from 1 to 8 μm to be compatible with the FEL. One of the beam tuning mirrors is held in a programmable kinematic mirror mount with programmable actuator that allows the focused laser beam to be rastered over the active target diameter. This rastering mirror moves the laser beam on the target; which raster's ~1.8 inches on the target. The focus lens is mounted in a motor driven linear translation stage that keeps the beam spot size constant during the rastering process. The laser beam is incident at an angle of 60° to normal to the rotating target, which is 2" in diameter. The raster mirror and translation stages are both controlled via computer. The complete assembly is housed within a laser safe enclosure with large access door.

H. Computer Control Software Package

The system is run via laptop computer with a LabVIEW interface and an Opto22 PLC control system. The computer provides both manual step-by-step operation of all valves on the system as well as auto pump/vent features for the main chamber and loadlock. The computer controls the laser beam raster pattern, substrate temperature profiles, target and substrate rotation speeds, substrate height, MFC flow rates, process pressure in the deposition chamber, target indexing, and full control over the Intelligent Window.

II. LASER SYSTEMS

A brief introduction to the pulsed lasers used is presented here.

A. High Intensity Peak Power Oscillator (HIPPO)

The Spectra-Physics High Intensity Peak Power Oscillator (HIPPO) comprises a solid-state laser head and a Model J80, dual-diode, pump power supply. The Nd:YVO$_4$ (Vanadate) based laser head is optimized for high peak power and high average power, with superior pulse stability. Vanadate is a popular solid state laser host due to its high gain and because it can provide high power laser emission at high pulse repetition rates. Being a solid state active media, Vanadate exhibits thermal lensing caused by the temperature gradients inside the crystalline material. Temperature gradient creates an optical index gradient that acts as a lens. The effective focal length of this thermal lens is determined in part by the amount of heat deposited in the crystal from the pump energy. The more pump energy applied to the crystal, the stronger the thermal lens and the shorter the effective focal length. The laser head (fundamental) provides 1064 nm output

alone and can include an optional second harmonic generator (532 nm), third harmonic generator (355 nm) or fourth harmonic generator (266 nm).

The HIPPO uses a W-fold cavity for convenient end-pumping the Nd:YVO$_4$ (Vanadate) lasing media crystal. A high reflector and output coupler define the cavity length. The latter allows a portion of the cavity light to pass out of the laser. To generate high energy pulses, two high-powered, acousto-optic Q-switches are placed in the cavity to act as switches to turn the laser on and off from 15 Hz to 300 kHz. Two high-power, thermally-stabilized, Spectra Physics FC bar laser diodes in the Model J80 power supply provide 2x26 W of 808 nm pump power to the laser cavity via fiber-optic cables. These cables attach to the laser head by connectors that maintain the alignment of the output from the fiber to the components inside the laser head.

A telescopic setup inside each input focuses the pump light through a dichroic mirror and into the end of the Vanadate crystal. The dichroic mirrors are highly transmissive at the diode pump wavelength and highly reflective at 1064 nm. The pump beams are absorbed by the crystal and 1064 nm and infrared (IR) intracavity light is generated.

To provide a source for output power monitoring, the output is sampled using a beam splitter and photodiode that are placed between the output coupler and the end of the laser. To provide safety, a mechanical shutter is placed inside the housing to stop the 1064 nm lasing action in its default closed position. It can be commanded to open and close via remote command but is closed when power is not applied to the system and will not open until commanded to do so.

B. Free Electron Laser (FEL)

The output of a Free-Electron Laser (FEL) is generated by stimulated emission of radiation. Its emission properties are essentially the same as any other laser – partial coherence, mono-chromaticity, etc., but the method used to generate the laser output in a FEL is much different than in a conventional laser. A FEL feeds a beam of electrons from a particle accelerator through a line of alternating magnets called an undulator or wiggler. The magnetic field causes the electrons to wiggle when they travel through the undulator and the electrons will emit radiation as their velocity changes. Most particle accelerators deliver a train of electron pulses. The interaction of the electrons with the combined magnetic and radiation field results in a periodic force on the electrons. As a result a velocity spread is induced on the electrons in the electron beam. After the electrons have propagated a certain distance, this velocity modulation is translated into a density modulation on the electron beam, i.e., bunches are formed approximately a radiation wavelength apart. Therefore the electron beam is capable of amplifying a radiation field coherently. Mirrors are used to reflect the radiation back and forth through the undulator. The electrons are not bound to any atoms, hence the term Free-Electron Laser. The cavity length is chosen such that the optical pulse overlaps with a fresh electron pulse after one round trip at the entrance of the undulator. The efficiency of the FEL depends on the wavelength generated and can vary from tens of percent at mm wavelengths to a fraction of a percent in the UV. However since the energy stored in the electron beam increases as the wavelength decrease, high peak powers can be produced at all wavelengths. The efficiency of a FEL can be enhanced in two ways; first a non-uniform undulator can be used to increase the extraction efficiency. Second the energy stored in

the electron beam after the interaction can be recovered, thereby increasing the overall efficiency of the system. Therefore the FEL can be tuned in principle over a very large wavelength range from m to nm. The output wavelength of the FEL is related to the wiggler periodically spacing, $\lambda_{wiggler}$, by the following equation

$$\lambda_{FEL} = \frac{\lambda_{wiggler}}{2\gamma^2}[1 + \kappa^2(B)], \tag{12}$$

where γ is the electron beam energy in terms of its rest mass, and κ is a term that is dependent on the magnitude and orientation of the magnetic field, B. However this range is limited in practice by the type of particle accelerator used (which fixes the energy range covered) and the fact that undulators have a fixed period and the strength of the magnetic field can be varied only within certain limits. Nevertheless the tuning range which can be obtained with FEL is in general much larger than those obtained with conventional lasers. Typical electron beam energies are tens of MeV and an undulator period of several centimeters. Oscillator FELs have also been operated in the UV, visible and radar wavelength regime. In general the undulator period must be reduced and the electron beam energy increased to obtain shorter wavelengths. The wavelength tunability, high efficiency and reliability can make the FEL very attractive for industrial applications.

i. **Meter calibration for FEL experiments**

To find the energy per pulse of the FEL hitting on the organic target kept inside the chamber, two energy meters were used. Fig. A2 shows the schematic diagram and actual image of the two meters used, one kept inside the chamber and the other outside the chamber. Such that, while doing actual experiment, meter 2 is removed and values from

meter 1 is taken into consideration to determine the energy per pulse of the FEL irradiated on the target. Bunches of individual long and short pulses were sent and the readings were noted from both the meters simultaneously. The linear fit of these values were plotted as shown in Fig. A3. Using the linear equation obtained, the energy of each pulse can be found.
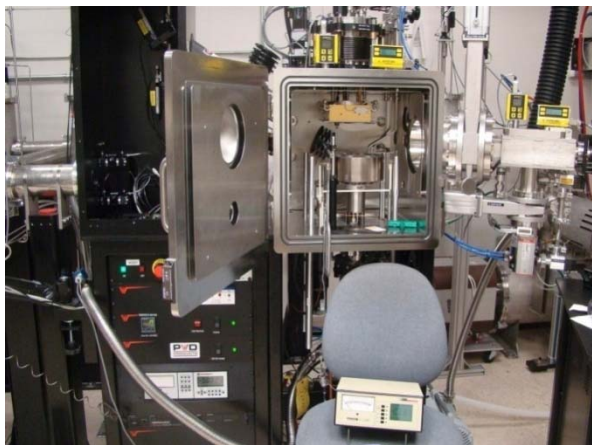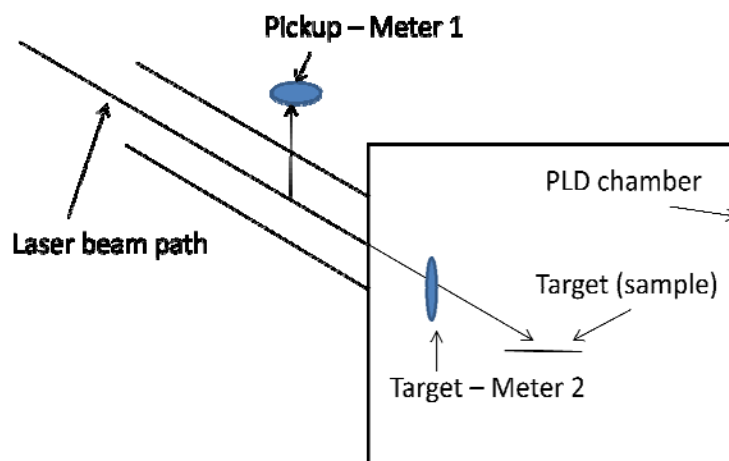

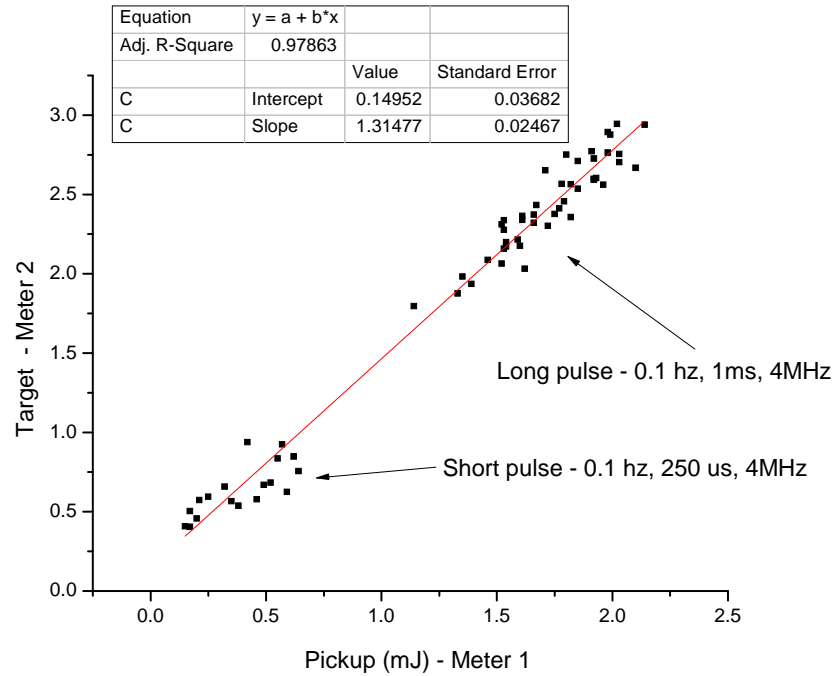FIG. A2. Schematic and actual picture of positioning the meter used for calibration.

FIG. A3. Liner fit of energy per pulse obtained from two meters

ii. Beam spot measurements

To measure the beam dimensions of the FEL radiation a knife edge measurements was performed. The razor blade was scanned through both vertical and horizontal dimensions of the beam. The beam reflected from the target was observed and the beam profile was created. The picture of knife edge measurements scanning both vertical and horizontal position is shown in Fig. A4.
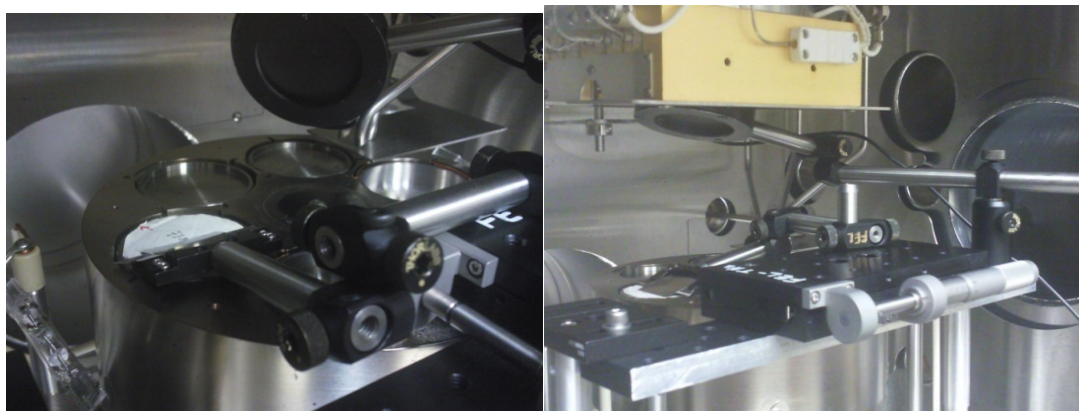
FIG. A4. Picture of position knife edge measurements.

Appendix B

INSTALLATION AND COMMISSIONING

The journey of PLD facility in Jefferson lab (FEL building - User Lab 5) started on May 2007. The space was allocated in one of the user labs (UL5) in the FEL building (Fig. B1).
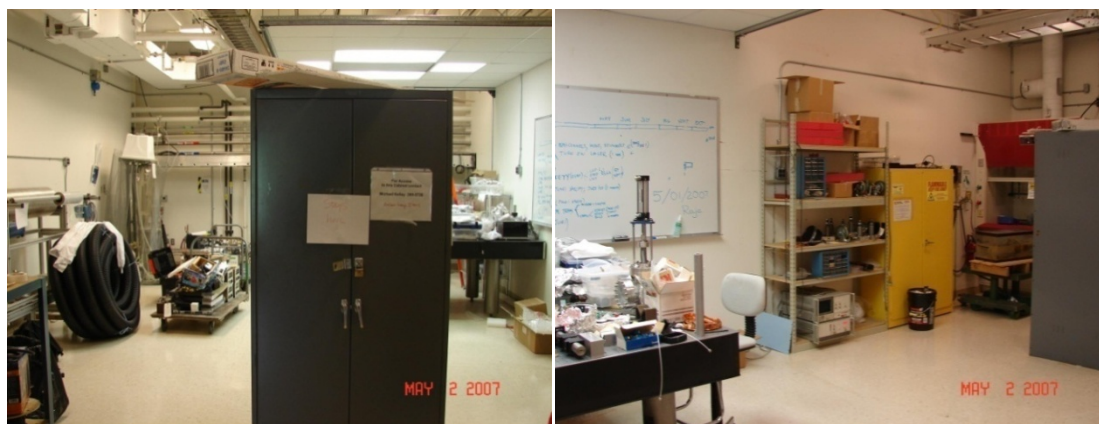

FIG. B1. Picture taken on May 2007.

The space in UL 5 was planned and authorized for the research equipment to move in. Extra cabinets, hardware were removed from UL5 and the Ti:sap laser (femtoseconds laser) was moved to UL 5 from UL6 (Fig. B2).

FIG. B2. Picture taken on June 2007.

First a power supply unit was installed. Then, the Ti:Sap laser was connected to the power supply unit, and also the chiller water provided from FEL building was hooked up. UL 5 was further cleaned to welcome the PLD 5000 (Fig. B3).

FIG. B3. Picture taken on November 2007.

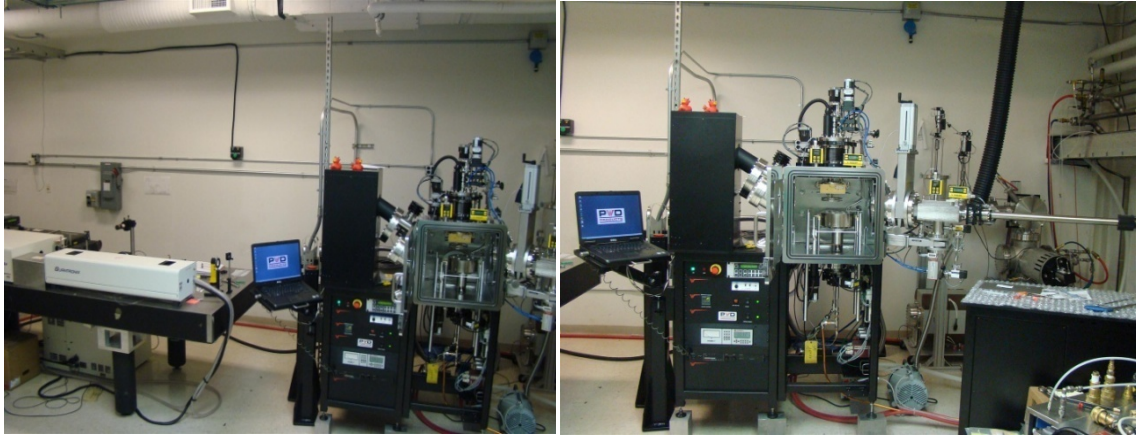By end of March 2008, the PLD 5000 was installed (Fig. B4).

FIG. B4. PLD 5000 was installed

By end of April 2008, the Ti:sap laser was aligned and beam characterization was performed to make sure the laser was working fine with necessary power output (Fig. B5). Commissioning of the PLD 5000 started step by step to make sure all the movable parts were operating without any problem.
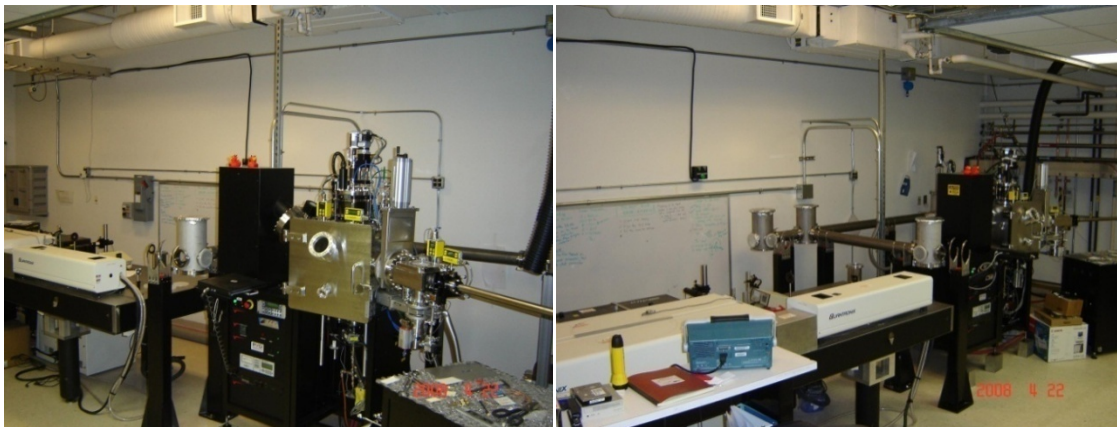

FIG. B5. All equipment was placed according to the plan.

First experiments performed in UL5 using the Ti:Sap laser on a niobium target inside PLD 5000 unit occurred in July 2008. This demonstrated that the laser had enough power to produce thermal energy, which can melt niobium surface in nitrogen atmosphere. The free electron laser was used in this research for the first time during December 2008; the beam was focused inside the PLD 5000 unit for depositing organic thin film on glass and NaCl substrate. In the picture (Fig. B6) is Dr. Michael J. Kelley (left) and Dr. Richard Haglund (Vanderbilt University), for the successful experiment done using the FEL laser on organics.

In the mean time, the power of the Verdi V5 was rolling over and was not stable. On February 2009, plans were made to move the HIPPO laser from UL 4 to UL5. It was moved to UL5 on May 2009. Optics were purchased, installed in their positions, the laser was characterized for beam spot and other measurements, and aligned into the PLD 5000 chamber. Experiments to produce superconducting phase niobium nitride and laser polishing using the HIPPO laser started (Fig. B7). In December 2009, organic (Cyclic Olefin Copolymer) was deposited to make a thin film using the free electron laser. In the fig. B8

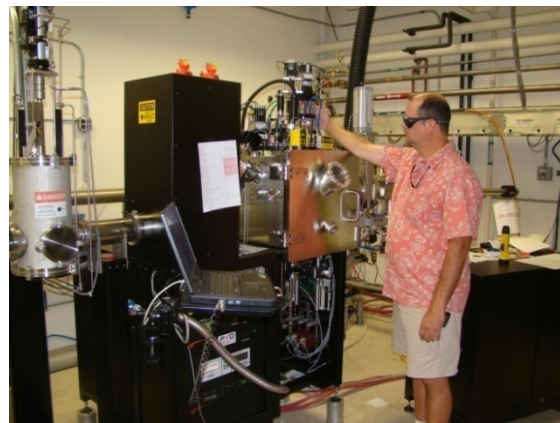FIG. B6. After successful deposition of organic thin film.

FIG. B7. Dr. Michael J. Klopf witnessing the deposition of δNbN.

(from left) is Dr. Hee Park (AppliFlex LLC), Dr. Michael J. Klopf, me, Dr. Michael J. Kelley, Dr. Sergey M. Avanesyan (Vanderbilt University).

FIG. B8. Another successful day for organic thin film deposition.

Appendix C

PROBLEMS ENCOUNTERED

I. Beam expander

The beam diameter coming out of HIPPO laser head is ~ 0.9 mm. A Galilean beam expander setup was done to expand the beam diameter ~v30 mm to obtain necessary fluence at the target. Fig. C1 shows the Galilean beam expander schematic and setup. The expanded beam was allowed to focus using a 800 mm focal length lens. At the position of the beam waist a SPRICON (beam profiler) was used to measure the spot diameter.
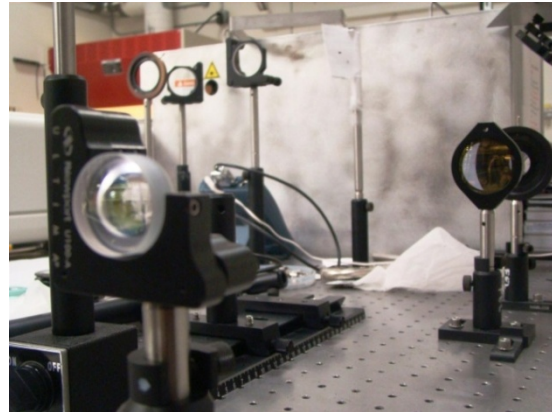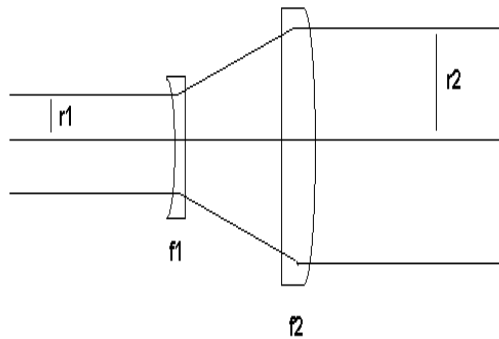

FIG. C1. Galilean beam expander setup

II. Gear system in PLD 5000

The whole substrate heater stage is moved in the z direction by a sprocket and bronze eccentric bushing which is attached to a chain and motor (Fig. C2). This sprocket got clogged, possibly due to tight screws or no free rotation of bushing. The complete rotating system was removed from the heater stage, by unscrewing the post and lifting it

up, which let sprocket and bushing come out. The parts were checked, cleaned with acetone, and moly disulfide was applied on sprockets for free rotation and fixed back to the *z*-stage. The parts need to be checked before starting any sort of experiment where the *z* stage needs to move up or down.
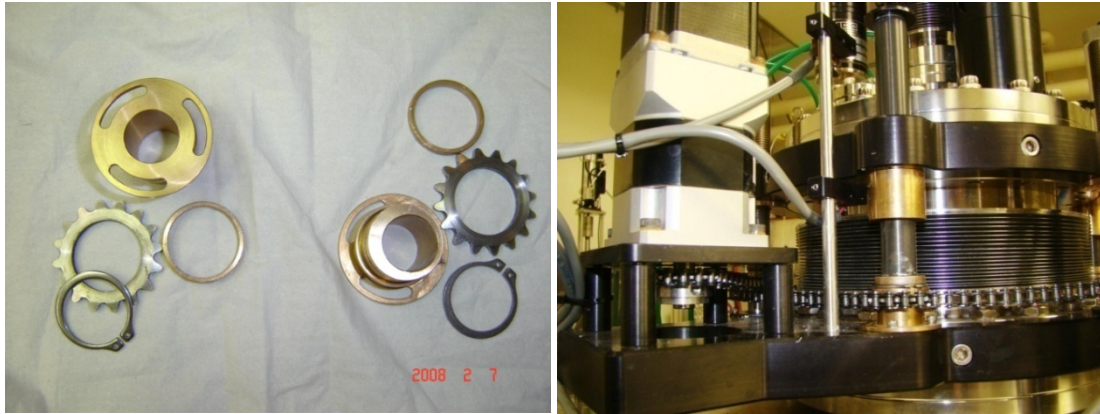

FIG. C2. Gear parts

III. Optics adjustments

Lenses of focal length 800 mm and 1000 mm were used for the HIPPO and the FEL laser respectively. The distance from the rastering mirror to the target location is constant (730.25 mm) in the PLD 5000. So the distance from the rastering mirror to the focusing lens is adjusted on the 2" post (Fig. C3) according to the lens used for the particular experiment (The locations of these lenses are marked on the post).

IV. Target pedestal motor revolution speed

Labview limits the target pedestal motor rotation to 12 rpm. This bounded the experiment on niobium melt smoothing to explore cases with less pulse overlap per unit area. This is a software restriction only, which can be removed by PVD Products Inc.
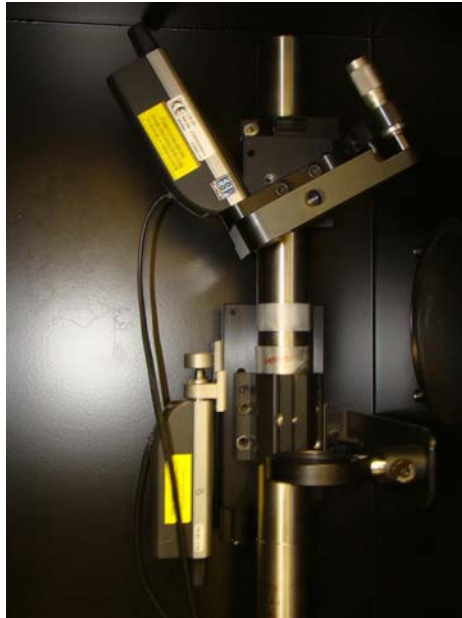
FIG. C3. Optics height adjustment according to the experiment.

V. Substrate shutter

Before starting the deposition on any substrate the surface of the target should be clean. The substrate shutter should be closed for few minutes, while the laser is rastering the surface. After few minutes we need to open the substrate shutter. Sometimes the shutter does not move to the open position completely (Fig. C4), which can cause two problems. First, the deposition is not uniform on the substrate because the shutter is half way in between the substrate and the target. Second, to change the target-substrate throw distance we need to move the substrate holder down from the z-stage. As the shutter is half way blocking the substrate position, the substrate holder hits the substrate shutter and if not noticed, then the rod of the substrate holder bends.
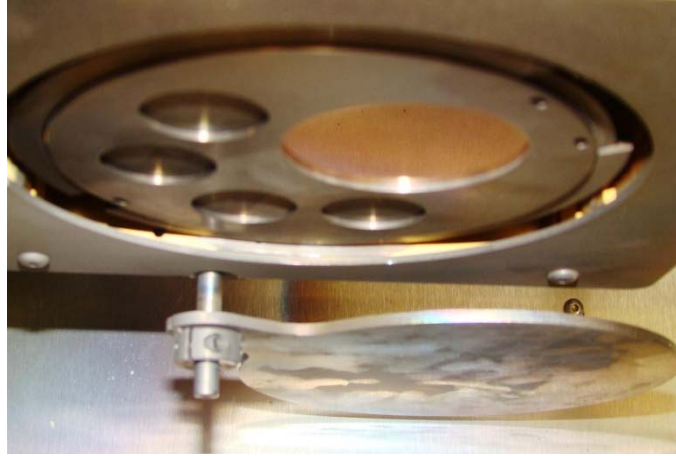
FIG. C4. Substrate shutter and substrate location

VI. Intelligent window (IW) rotation

After the experiments, on the exposed area of the inner side of the CaF intelligent window there may be some thin film depositions. When the next deposition needs to be done, the deposited film on the inner side of the window can block 100% transmittance of the laser power, causing loss of fluence. So before doing any deposition, it is good to check the power of the laser inside the chamber and make sure the power is the same as initial power. If the power is low, then the intelligent window should be rotated little bit through the Labview interface. Once the inner side of the window is completely coated with different thin film and the laser has no path to go into the chamber, this window should either be replaced or etched for a clear area.
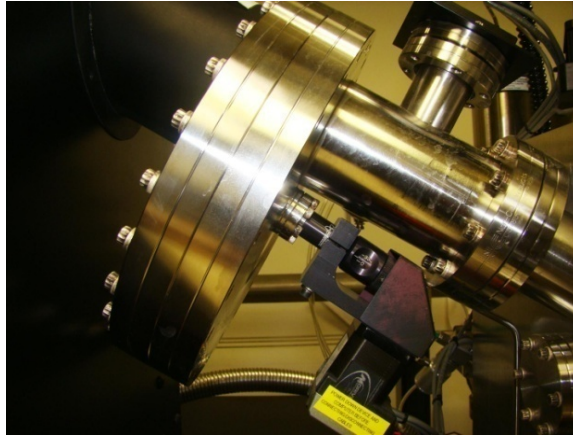
FIG. C5. Position of Intelligent window

VII. Aperture near the intelligent window was removed

The aperture outside the PLD chamber was ~10 mm. The beam diameter of the FEL was bigger than this aperture, which was clipping the beam entering inside the chamber. So the aperture was removed.

VIII. Chiller water facility

The PLD 5000 unit is connected to the chiller water provided by the FEL facility. Chiller water is transported through stainless steel pipes. Inside the lab, the water is transferred through copper pipe, which could have some dust/rust particles. These particles got clogged inside the PLD unit and the heat produced due to the turbo and other motors were not removed from the machine causing an explosion of the return supply water pipe, above the PLD 5000 unit. Thus a filter is attached (Fig. C6) to filter these dust particles and provide chilled water inside the unit preventing further explosions.

FIG. C6. New water filter.

VITA

Senthilraja Singaravelu (Raja)
Department of Physics, ODU
4600 Elkhorn Avenue, Norfolk, VA 23529.

EDUCATION:
- **Ph.D,** Physics, Old Dominion University, Norfolk, VA.   [May *2012*]
- **M.S.,** Physics, Old Dominion University, Norfolk, VA   [*May 2006*]
- **M.Sc., Physics** (*Specialization in Electronics*)**,** Bharathiar University, India   [*April 2001*]
- **B.Sc., Physics,** University of Madras, India   [*March 1998*]

PATENT:
- Patent disclosure submitted: *"Enhanced Superconducting Surface for Nb SRF Cavities Obtained by Gas Laser Nitriding,"* Thomas Jefferson National Laboratory, Newport News, VA.

HONORS AND AWARDS:
- Article "*Laser Nitriding of Niobium for application to Superconducting Radio-Frequency Accelerator Cavities"* was selected for Virtual Journal of Applications of Superconductivity, November 15, 2011, published by AIP and APS.
- Honorable Mention for the Visiting Scholar Award (Second prize) for the paper presented at 9th and 10th Annual Graduate Research Symposium, March 2010 & 2011 respy., The College of William & Mary, USA.
- Third prize for the poster presentation presented at Jefferson Lab Annual Users meeting, June 2010, Thomas Jefferson laboratory, USA.
- Second prize for the poster presentation presented at Tidewater Virginia Chapter & Washington, D.C area Chapter of Sigma Xi-11th Annual Student Research Poster Session, November 2009, Christopher Newport University, USA.
- Best post graduate thesis award for the topic entitled "Vacuum evaporated vanadium pentoxide (V_2O_5) thin films," Bharathiar University, India.
- First in the class, B.Sc. (Physics), July 1995 – March 1998, University of Madras, India.

PUBLICATIONS:
- **S. Singaravelu**, J.M. Klopf, G. Krafft, M.J. Kelley, "*Laser Nitriding of Niobium for application to Superconducting Radio-Frequency Accelerator Cavities,*" J. Vac. Sci. Tech. B, **29**, 061803, (2011).
- **S. Singaravelu**, J.M. Klopf, C. Xu, G. Krafft, M.J. Kelley, "*Laser Polishing of Niobium for application to Superconducting Radio-Frequency Cavities,*" – Submitted to J. Vac. Sci. Tech. B, 2011.
- **S. Singaravelu**, J.M. Klopf, K. E. Schriver, H.K. Park, M.J. Kelley, R.F. Haglund Jr., "*Resonant Infrared Pulsed Laser Deposition of Cyclic Olefin Copolymer Films*", - Submitted to App. Phys. A, 2011.
- S. M. Avanesyan, A. Halabica, S. L. Johnson, M. J. Kelley, J. M. Klopf, H. K. Park, K. E. Schriver, **S. Singaravelu,** R. F. Haglund, Jr., "*Deposition of polymer barrier materials by resonant infrared pulsed laser ablation,*" Proc. SPIE, vol. 7585, 2010.